Laser systems for collinear spectroscopy and the charge radius of ^{12}Be

Dissertation

zur Erlangung des Grades
"Doktor der Naturwissenschaften"

im Promotionsfach Chemie
am Fachbereich Chemie, Pharmazie und Geowissenschaften
der Johannes Gutenberg-Universität
in Mainz

Andreas Krieger
geb. in Frankfurt am Main

Mainz, den 30. März 2012

Abstract

Collinear laser spectroscopy has been used to investigate the nuclear charge radii of short-lived medium- and heavy-Z nuclei for more than three decades. But it became only recently be applicable to low-Z nuclei. This region of the nuclear chart attracts attention because so-called ab-initio nuclear models, based on realistic nucleon-nucleon potentials, can only be applied to the lightest elements due to the rapidly increasing calculational demands with the number of nucleons. Furthermore, strong clusterization of atomic nuclei occurs and the encountered halo nuclei are presently subject of intense research.
The isotopic chain of beryllium exhibits the prime example of a one-neutron halo nucleus, ^{11}Be, and the two- or four-neutron halo nucleus ^{14}Be. ^{12}Be is a key isotope between these two exotic nuclei and particularly interesting because the nuclear shell model predicts a shell closure for the magic neutron number $N = 8$.
In the course of this thesis, several frequency-stabilized laser systems for collinear laser spectroscopy have been developed. At TRIGA-SPEC a frequency-doubled diode laser system with a tapered amplifier and a frequency comb-stabilized titanium-sapphire laser with a frequency doubling stage are now available for the spectroscopy of refractory metals above molybdenum. They have already been used for test-experiments and commissioning of the TRIGA-LASER beamline. Furthermore, frequency-quadrupling of the Ti:Sa laser was demonstrated to expand the emitted wavelengths into the 200 nm region. At ISOLDE/CERN a frequency comb-stabilized and an iodine-stabilized dye laser were installed and applied for laser spectroscopy of ^{9,10,11,12}Be$^+$. The improved laser system and the development of a delayed photon-ion coincidence detection improved the sensitivity of the beryllium spectroscopy by more than two orders of magnitude and, thus, the previous measurements of $^{7-11}$Be could be extended for the first time to the short-lived isotope ^{12}Be. In addition, the accuracy of the absolute transition frequencies and of the isotope shifts of ^{9,10,11}Be were significantly improved.
Comparing the extracted charge radii with results of the Fermionic Molecular Dynamics model, the trend of the charge radii of the lighter isotopes can be explained by the pronounced cluster structure of the beryllium nuclei. Further it was derived that the ground-state wavefunction is clearly dominated by an intruder $(sd)^2$ configuration. This is contradictory to the nuclear shell model expectation of a p^2 ground-state configuration and strongly supports the previously observed breakdown of the $N = 8$ magic shell closure in the beryllium isotope ^{12}Be.
This work was financially supported by a grant from the Carl-Zeiss-Stiftung.

Zusammenfassung

Die kollineare Laserspektroskopie hat sich in den vergangenen drei Jahrzehnten zur Bestimmung der Kernladungsradien mittelschwerer und schwerer kurzlebiger Atomkerne in ausgezeichneter Weise bewährt. Auf die Isotope sehr leichter Elemente konnte sie allerdings erst kürzlich erweitert werden. Dieser Bereich der Nuklidkarte ist von besonderem Interesse, denn die ersten ab-initio Modelle der Kernphysik, die den Aufbau eines Atomkerns basierend auf individuellen Nukleonen und realistischen Wechselwirkungspotentialen beschreiben, sind gegenwärtig nur für die leichtesten Elemente anwendbar. Außerdem existiert in dieser Region eine besonders exotische Form von Atomkernen, die sogenannten Halokerne. Die Isotopenkette der Berylliumisotope zeichnet sich durch das Auftreten des Ein-Neutronen Halokerns ^{11}Be und des Zwei- oder Vier-Neutronen-Halos ^{14}Be aus. Dem Isotop ^{12}Be kommt durch seine Position zwischen diesen beiden Exoten und den im Schalenmodell erwarteten magischen Schalenabschluss $N = 8$ eine besondere Bedeutung zu.

Im Rahmen dieser Arbeit wurden mehrere frequenzstabilisierte Lasersysteme für die kollineare Laserspektroskopie aufgebaut. An TRIGA-SPEC stehen nun unter anderem ein frequenzverdoppeltes Diodenlasersystem mit Trapezverstärker und frequenzkammstabilisierter Titan-Saphirlaser mit Frequenzverdopplungsstufe für die Spektroskopie an refraktären Elementen oberhalb von Molybdän zur Verfügung, die für erste Testexperimente eingesetzt wurden. Außerdem wurde die effiziente Frequenzvervierfachung eines Titan-Saphirlasers demonstriert. An ISOLDE/CERN wurde ein frequenzkammstabilisierter und ein jodstabilisierter Farbstofflaser installiert und für die Laserspektroskopie an ^{9,10,11,12}Be$^+$ eingesetzt. Durch das verbesserte Lasersystem und den Einsatz eines verzögerten Koinzidenznachweises für Photonen und Ionen gelang es die Empfindlichkeit der Berylliumspektroskopie um mehr als zwei Größenordnungen zu steigern und damit die früheren Messungen an $^{7-11}$Be erstmals auf das Isotop ^{12}Be auszuweiten. Außerdem wurde die Genauigkeit der absoluten Übergangsfrequenzen und der Isotopieverschiebungen der Isotope ^{9,10,11}Be signifikant verbessert.

Durch den Vergleich mit Ergebnissen des Fermionic Molecular Dynamics Modells kann der Trend der Ladungsradien der leichteren Isotope durch die ausgeprägte Clusterstruktur der Berylliumkerne erklärt werden. Für ^{12}Be wird ersichtlich, dass der Grundzustand durch eine $(sd)^2$ Konfiguration statt der vom Schalenmodell erwarteten p^2 Konfiguration dominiert wird. Dies ist ein klares Indiz für das bereits zuvor beobachtete Verschwinden des $N = 8$ Schalenabschlusses bei ^{12}Be.

Diese Arbeit wurde durch ein Stipendium der Carl-Zeiss-Stiftung finanziell unterstützt.

Contents

List of Figures

1 Motivation

The adduced evidence of the existence of the atom [Ein05] provoked Joseph Thompson to suggest the first atomic model, the *plum pudding* model. But only a few years later, in 1911, Ernest Rutherford abolished the plum pudding model after he discovered the constitution of atoms in scattering experiments. Amongst other atomic models, *e.g.*, Bohr's atomic shell model also nuclear models were proposed guided by experimental results: The liquid drop model, a fairly well-known macroscopic model, assumes that the nucleus is an incompressible liquid and estimates the radius R of a nucleus to be proportional to $R \propto \sqrt[3]{A}$ fm [May02].
In the early years nuclear density studies by electron or proton scattering experiments have been restricted to stable nuclei [Tan03]: Many nuclei obeyed this postulate and a homogeneous distribution of protons and neutrons in the nucleus was assumed. The constitution of the nucleus was explained by the *nuclear shell model* and M. Goeppert-Mayer & H. D. Jensen explained the magic numbers in the nuclear shell model to describe experimental results [Goe55].
This picture was questioned when exotic and unstable nuclei were investigated experimentally after the invention of radioactive beam facilities. In 1985 Tanihata et al. investigated interaction cross section measurements at high energies (800A MeV) to determine the root mean square matter radii of light isotopes. The results are shown in Fig. 1.1. Some of these isotopes (*e.g.* ^{11}Li, ^{11}Be and ^{14}Be) exhibit an extended nuclear matter distribution compared to their neighboring isotopes. First, in ^{11}Li this effect was attributed to either a large deformation of the nucleus or an extended distribution of nuclear matter [Tan85]. The measurement of the spin and the magnetic moment [Arn87] as well as the quadrupole moment of ^{11}Li disproved a deformation of ^{11}Li [Arn92]. Due to (a) weakly bound nucleon(s) in these isotopes the picture of a halo formation established. The so-called "halo nuclei" [Han87], which mainly occur near the dripline, were discovered. For the sake of completeness the boron isotopic chain up to the atomic mass number A = 15 which was also measured by Tanihata is depicted in Fig. 1.1 which shows no indication of such a halo formation[1]. Up to now several neutron halo nuclei are verified, *e.g.* ^{6,8}He, ^{11}Li, ^{11,14}Be, ^{15,19}C. Concerning boron, some indication for halo formation was observed in the excited states of ^{17,19}B. Neutron halo nuclei typically fulfill three characteristics [Tan03]:

- a very low neutron or two-neutron separation energy of the outer neutrons (typically $S_n, S_{2n} \leq 1$ MeV),
- narrow momentum distribution of breakup fragments,

[1] Proton halo nuclei, such as ^{8}B [Ili11], do not show an extended matter radius due to the coulomb barrier. However, they might exhibit increased charge radii.

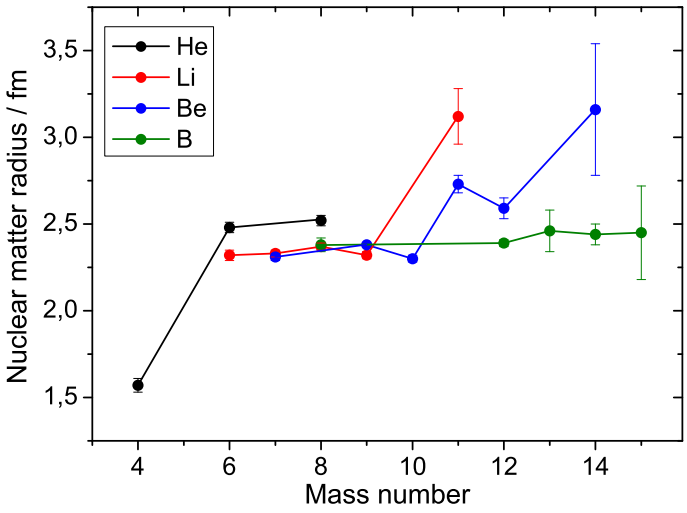

Figure 1.1: The root mean square radii of the matter distribution of light isotopes determined by interaction cross section measurements. Values taken from [Tan88].

- an increased cross section in scattering experiments compared to their neighbors.

1.1 Nuclear Charge Radii of Halo Isotopes

Besides the nuclear matter radius, the charge radius (proton distribution) is another characteristic property of the nuclear ground state. An extended matter distribution caused by halo formation influences the charge radius as well. The nuclear properties predicted by theoretical calculations, like, *e.g.*, the Greens-Function Monte-Carlo (GFMC) calculations [Pie01], No-Core Shell Model (NCSM) [Nav09] or the Fermionic Molecular Dynamics (FMD) Model [Nef05] are compared with the experiment to benchmark the models. These, among other "ab-initio" calculations, are mostly based on realistic nucleon-nucleon and three-nucleon potentials like the Argonne V18 or Illinois potentials [Wir95], respectively, and, thus, test our knowledge of fundamental nuclear forces at one edge of the nuclear chart. Especially deformed and halo nuclei challenge the theoretical models, since the long extended tail in the wave functions (which occur in loosely bound systems) are difficult to describe as well as the knowledge of nuclear forces at these exotic formation is still vague. A model-independent way to extract the rms charge radius is offered by the optical isotope shift (IS), which is the frequency difference in an electronic transition of two isotopes of the same element. The IS consists of a nuclear volume effect and a mass effect, whereby the latter must be known in order to extract the change of the rms charge radius from the nuclear volume effect. This method is widely used for short-lived heavy isotopes since many years [Ott89], but for the very light isotopes $Z \leq 10$ the mass effect contribution dominates the IS and thus very precise calculations of the mass effect are in need. A special role plays the spectroscopy on hydrogen- and hydrogen-like systems, because these

are the only systems so far, where absolute charge radii can be extracted from the atomic spectra. One of the contemporary open questions is the disagreement between the proton radius determined from laser spectroscopy of atomic hydrogen and muonic hydrogen [Poh10] which disagree by about 5σ and only the atomic hydrogen value is also in agreement with the charge radius from elastic electron scattering [Sic03, Ber10]. The difficulty in extending mass shift and QED calculations to systems with more than one electron lies in the complicated electron-correlation integrals that appear in the formulas. With the expansion of reliable isotope shift calculations in two- and three-electron systems, charge radii of halo nuclei came into reach. G. Drake and Z. C. Yan were the first who calculated the mass effect in three-electron systems to the required accuracy of better than 100 kHz [Yan00]. Since then, these calculations have been improved by two orders of magnitude for three-electron systems [Yan03, Puc06, Yan08, Noe11] and first results are even available for four electron systems [Pac04]. Based on these calculations the proton distribution of the isotopic chains of the lightest isotopes were determined in high-precision laser spectroscopy experiments during the last decade. Before it was only possible to reach this accuracy for He-like systems and measurements were performed on atomic He and Li^+ ions using optical pumping in combination with magnetic resonance and collinear saturation spectroscopy [Rii94], respectively. In Munich two photon resonance spectroscopy of ^{1,2}H was performed [Ude97, Hub98, Jen11], whereas Shiner *et al.* used the magnetic resonance technique to determine the nuclear charge radius of ^{3}He [Shi95]. To reach the accuracy for short-lived isotopes with lifetimes of a few ms and very small production rates demands dedicated laser spectroscopy that meet all the needs concerning efficiency, speed and accuracy.

At GANIL and at the Argonne National Laboratory the helium atoms ^{6,8}He, which are known to be two and four-neutron halo nuclei, respectively, were confined in a magneto-optical trap [Wan04, Mue07] to investigate the nuclear charge radii by high-precision laser spectroscopy. For short-lived lithium isotopes a dedicated two-photon resonance ionization spectroscopy technique was developed and applied at GSI to determine the charge radii of ^{8,9}Li [Ewa04] and later at TRIUMF where the most prominent two-neutron borromean halo nucleus ^{11}Li was investigated [San06, Noe11]. The beryllium isotopes ^{7,9,10}Be as well as the one neutron halo nuclei ^{11}Be were measured performing combined collinear and anticollinear laser spectroscopy at ISOLDE/CERN [Noe09, Zak10] in the framework of the BeTINa Experiment[2] in 2008.

In the framework of this thesis, the BeTINa Experiment was continued to extend the measurements of the beryllium isotopic chain up to ^{12}Be. Due to the very low production rate of about 1500 ions/pulse at ISOLDE[3] compared to the lowest yield of $7 \cdot 10^7$ ions/pulse in 2008 at ^{11}Be, the measurement of the isotope shift of ^{9,12}Be was infeasible. To overcome this limitation, the sensitivity of the collinear laser spectroscopy had to be increased. Two attempts are tried within this work: the usage of the ISOLDE cooler and buncher ISCOOL and a photon-particle coincidence detection by counting only those photons which are in delayed coincidence with the corresponding ion [Eas86].

[2] (**Be**ryllium **T**rap for the **I**nvestigation of **N**uclear ch**a**rge radii)

[3] Yield taken from the ISOLDE yield table.

^{12}Be attracts attention since it is the neighboring isotope of the one neutron halo nucleus ^{11}Be and the borromean halo nucleus ^{14}Be. This halo character arises from an *sd*-intruder configuration, that in case of ^{11}Be even inverts the ground state parity into $1/2^+$ instead of the shell-model expected $1/2^-$ [Gei99]. From this point of view, a slight halo-like structure could also be expected in case of ^{12}Be if it is considerably influenced by the intruding *sd*-shell. Besides the fact that both neighboring isotopes ^{11}Be and ^{14}Be are known to be halo nuclei, ^{12}Be has a large neutron separation energy of ($S_n = 3.67$ MeV) [Ett10] and a wide momentum distribution which has been determined in nuclear breakup reactions [Zah93]. Even though both characteristics of a halo formation are not fulfilled, recent proton scattering experiments performed at GSI [Ili11] indicated an extended matter distribution which could be attributed to a slight neutron halo character or to a deformation of the nucleus. Along benchmarking theoretical models the charge radius of ^{12}Be attains additional information of the nuclear structure.
Besides the discovery of the halo nuclei, the intense research of radioactive isotopes far from the valley of stability, since the appearance of the first radioactive beam facilities, indicated the disappearance of the magic numbers in regions far away from the valley of β-stability. Instead new magic numbers may be established as discussed by [Sor08]. ^{12}Be is a candidate for this effect, since according to the nuclear shell model proposed inter alia by M. Goeppert-Mayer it should posses the $N = 8$ magic shell closure. It was found in FMD nuclear structure calculations that an admixture of *sd*-intruder states into the shell-model *p* states changes the charge radius considerably [Nef11]. According to these calculations the charge radius should decrease if the neutrons occupy predominantly the p shell whereas it should increase for orbitals with sd character. Thus, the measurement of the charge radius of ^{12}Be will give a clear indication for a disappearance of the magic number $N = 8$.

1.2 Refractory elements around $Z = 40$ and $N = 60$

A similar effect is found around the $N = 60$ region of the elements around $Z = 40$ as depicted in Fig. 1.2. It shows the changes in the charge radius around the shell closure $N = 50$ and around $N = 60$ for isotopes of elements yttrium to molybdenum ($Z = 39-42$). This region became only recently available for IS measurements [Che07, Cam02, Che07, Cha09]. A common feature of the radii in this range is a compression of the charge radii with increasing neutron number below $N = 50$ and increasing radii above. The second striking feature is the strong increase at the $f_{9/2}$ sub-shell closure, which exhibits reduced strengths with increasing Z. This is attributed to a strong deformation from spherical to prolate (oblate) deformation. However, in the isotopic chain of the refractory element molybdenum this transition is not observed anymore [Cha09]. This is ascribed to the changing neutron-proton interaction along the isotones. While ab-initio nuclear models are working only for the light elements yet, the region of medium heavy and heavy mass isotopes is the realm of the shell model, applying different interactions.
The investigation of the nuclear properties of the refractory elements in this region is one

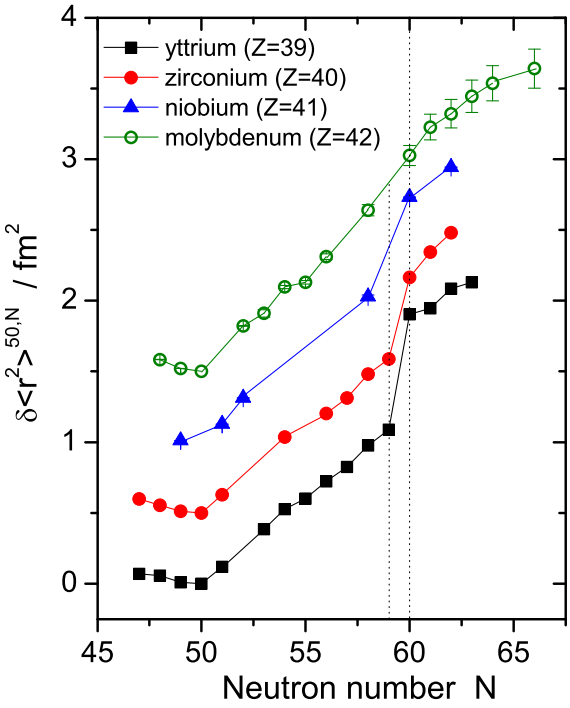

Figure 1.2: Changes in the charge radius between the magic shell closure N = 50 and 60. The isotopic chains (separated in 0.5 fm for a better illustration) were denoted as follows: ■ yttrium [Che07], ● zirconium [Cam02], △ niobium [Che07] and ○ molybdenum [Cha09]. Isotopes at N = 50 exhibit the smallest charge radius of the whole isotopic chain. A sudden increase of the charge radii are observed around N = 60 which is attributed to a deformation. This deformation disappears in the molybdenum ○ isotopic chain.

of the goals of the TRIGA-SPEC project, which is an apparatus for high precision laser spectroscopy and mass spectrometry in Mainz. Here, neutron-rich nuclei can be produced by neutron-induced fission of ^{235}U and ^{249}Cf in the surrounding of the core of a nuclear research reactor. The fission products recoiling from the target can be stopped in a gas chamber and transported via a helium-jet through a capillary to the experiment. Contrary to ISOL facilities, this technique gives access to the refractory elements.

1.3 Laser Systems for Collinear Laser Spectroscopy

All these investigations require laser systems mostly in the ultra-violet and near UV regions. Since the spectral width of each active medium covers only a part of the required laser wavelengths, several different laser systems must be used to cover the whole spectral range. Diode lasers attract attention mainly in the deep red to IR range since these low-cost lasers are easy to align, but the main drawback is their small spectral range of a few tens of nm. A Titanium:Saphirre (Ti:Sa) ring laser covers the wavelength range from

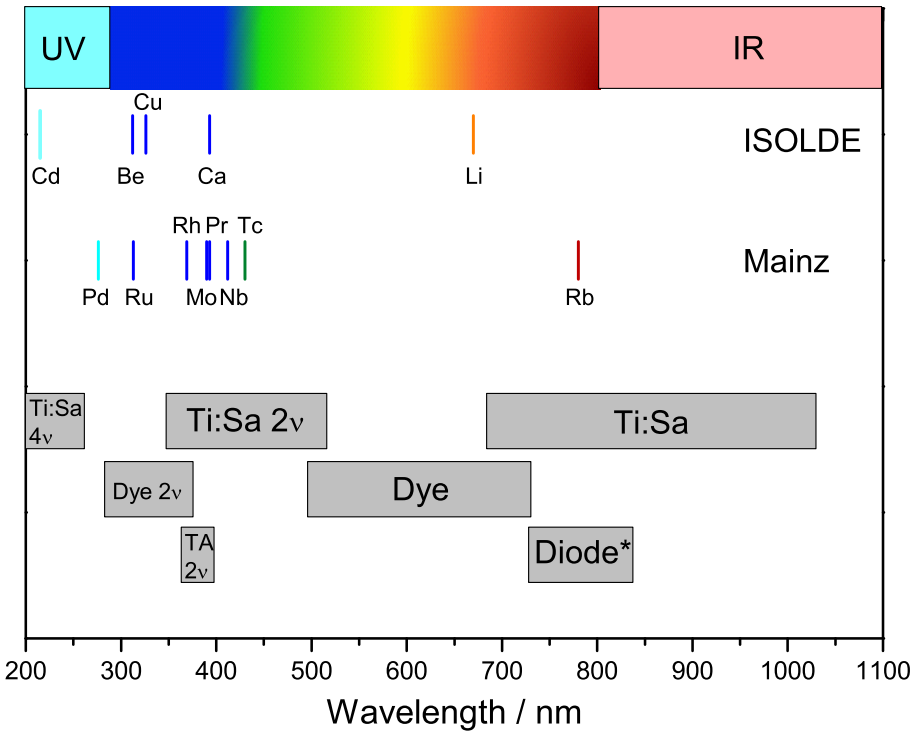

Figure 1.3: Laser systems that have been set-up at TRIGA-SPEC and at ISOLDE to cover the required transition wavelengths of interest. At TRIGA-SPEC mainly the refractory elements are of interest. The upper row shows the elements investigated at the ISOLDE facility and the second row the elements that can be investigated at TRIGA-SPEC in Mainz. ∗ Only diode laser installed at Mainz are listed.

700 to 1030 nm with excellent stability, whereas only a dye laser can be operated between 500 to 700 nm[4]. In order to achieve a wavelength below the wavelength of the pump laser, a second harmonic generator must be used. In combination with a Ti:Sa or a Dye laser the complete UV region can be covered as illustrated in Fig. 1.3. The deep UV region around 250 nm and below is achieved by frequency-quadrupling a Ti:Sa laser, since these lasers distinguish themselves with an excellent beam quality and high output powers of several watts. During the work of this thesis (amplified) diode lasers, dye lasers and Ti:Sa lasers, SHG and FHG were installed and applied for the spectroscopy of a number of elements.
This thesis is divided as follows: In Chapter 2 the theory of nuclear structure and nuclear models are presented as well as the isotope shift and the mass shift calculations in a three electron system. Chapter 3 introduces into the experimental techniques for ion beam production and laser spectroscopic techniques applied at the TRIGA research reactor in Mainz and at the ISOLDE facility at CERN. The laser developments at TRIGA-LASER are detailed in Chapter 4. While the BeTINa experiment and the measurement of the

[4]This region becomes now also available with a Ti:Sa laser by sum frequency generation with powerful fiber lasers using periodically-poled non-linear crystals.

short lived radioactive ^{12}Be isotope at CERN is presented in Chapter 5. The last Chapter explains the principle of a laser spectroscopic high-voltage determination of the ISOLDE HV installation in the ppm regime. Finally, the thesis ends with a summary and an outlook.

2 Theory

2.1 Nuclear Structure

The nuclear structure of stable nuclei is fairly well understood with a variety of nuclear models. Roughly, three regions of the nuclear chart can be distinguished which are described by different theoretical approaches: light nuclei can be modeled using *ab-initio* approaches, *e.g.* Greens-Function Monte-Carlo, Fermonic Molecular Dynamics or Cluster models, medium heavy nuclei in the Interacting Shell Model and heavy nuclei with the Energy Density Functional theory. However, the ability to predict fundamental properties of nuclei away from the valley of stability is still limited. Therefore properties like the spatial structure, nuclear charge and matter distributions of exotic nuclei are experimentally studied to benchmark and further develop theoretical models. Various methods were developed over the past years and some of them are briefly summarized in this chapter.
The nuclear matter distribution $\rho_m(r)$ is the sum of the proton (charge) $\rho_c(r)$ and neutron distribution $\rho_n(r)$:

$$\rho_m(r) = \rho_c(r) + \rho_n(r) \tag{2.1}$$

These density distributions are related to the matter and charge radii $r_{m,c}$ according to [Pov06]

$$\left\langle r^2_{m(c)} \right\rangle = 4\pi \int_0^\infty r^2 \rho_{m(c)}(r) r^2 dr \tag{2.2}$$

in the case of a spherically symmetric, angle-independent nuclear charge distribution. For stable nuclei the root mean square charge radius $\left\langle r_c^2 \right\rangle$ can be obtained from electron scattering experiments. Since the electromagnetic interaction with a point-like particle is well understood at intermediate momentum transfer, the nuclear charge radius can be extracted from elastic scattering cross section measurements in a model-independent way[1]. The present work refers to the measurement of the nuclear charge radius of ^{9}Be [Jan72], which is used as the reference radius to extract the absolute charge radii from the beryllium isotope shift measurements in Chapter 5.8.1.
Since secondary (radioactive) beams are available, the nuclear matter radius r_m of short-lived isotopes is commonly determined from interaction cross section measurements in a target by nucleus-nucleus collisions. The interaction cross section $\sigma_I = \pi \left(R_p + R_t\right)^2$, where R_p and R_t are the interaction radii of projectile and target nuclei, is measured with

[1] However, the mean square charge radius has to be determined from the behavior of scattering amplitude at zero momentum transfer $q = 0$. Hence, it must be extrapolated from the measurements at small but finite momentum transfer and how well this is understood is again debated these days due to the different proton radii observed in electron scattering and atomic and muonic spectroscopy [Poh10].

the transmission method using a large acceptance spectrometer. Firstly, isotopes of He, Li and Be were studied at high energies (790 MeV/nucleon) [Tan85, Tan88, Alk96]. The investigation of the spatial structure became even more interesting since Tanihata *et al.* discovered the *halo nuclei* [Han87]. The interaction cross section of ^{11}Li was found to be much larger than its neighboring isotopes, which implies a sudden increase of the matter radius from ^{9}Li to ^{11}Li. Most often the experimental results are analyzed in the Glauber theory which relates the experimentally derived cross section σ_I to the matter radius. Thus, the extracted matter radii are model-dependent.
The measurement of the differential cross section in proton elastic scattering experiments provide more accurate information about nuclear properties [Ege02, Dob06, Alk06]. Due to the short lifetime of exotic nuclei the proton elastic scattering is performed in inverse kinematics. Recently, such an experiment was performed at GSI/Darmstadt by Ilieva *et al.* [Ili08, Ili11] measuring the beryllium isotopic chain $^{7-14}$Be at small momentum transfer. The experiment was performed in the IKAR chamber, which served as a hydrogen target and recoil-proton detector simultaneously. Since the four momentum transfer t is measured at several points and the cross sections are bigger at small momentum transfers, high statistical accuracy can be achieved. The Glauber multiple-scattering theory therefore allows the determination of the radii of the nuclear core and (a possible) halo from the absolute differential cross section as a function of the four momentum transfer t (GeV/c)^2. As an example the differential cross sections of ^{12}Be versus the four momentum transfer are shown in Fig. 2.1 (left). The cross sections are divided by the exponential function $C_0 \cdot exp\,(B_0 t)$. Here C_0 denotes the absolute value of the differential cross section and B_0 the slope at this momentum transfer. If a halo structure is assumed, a low-density-tail in the wave functions is expected since light nuclei have roughly Gaussian density distributions (compared to the heavier ones which have Woods-Saxon density distributions), the elastic scattering cross section shows exponential behavior. If exists, the deviation from the exponential behavior is thus clearly visible. Different density parameterizations, *e.g.*, single Gaussian and Fermi parameterization were applied to the experimental data, but do not reproduce the trend of the data points. If a halo nucleus is assumed, it is reasonable to parameterize the densities of the core and halo separately *e.g.* applying a Gaussian-Gaussian, Gaussian-halo or sum-of-Gaussian parameterization. The averaged density distribution extracted from Fig. 2.1 (left) is depicted in Fig. 2.1 (right). In [Ili08, Ili11] this result is interpreted as an evidence for an extended matter distribution of the ^{12}Be nucleus. The matter radius is 2.71(6) fm.
Nuclear charge radii can only be extracted from these data if a particular distribution is assumed in the Glauber model and thus they are strongly model dependent. However, it has been shown in the lithium isotope chain that charge radii can be determined in principle from nuclear charge exchange reactions [Bla92]. Only recently, this method was successfully applied to the isotope chain of beryllium and the trend of the charge radii obtained with this method is similar to that extracted from optical isotope shifts [Tan12]. Optical isotope shift measurements provide a model-independent way to determine the nuclear charge radius. Therefore the hyperfine structure of at least two isotopes of the same element are studied. These isotope shift measurements of the atomic levels are mostly performed by high resolution spectroscopy. In this thesis the very sensitive technique

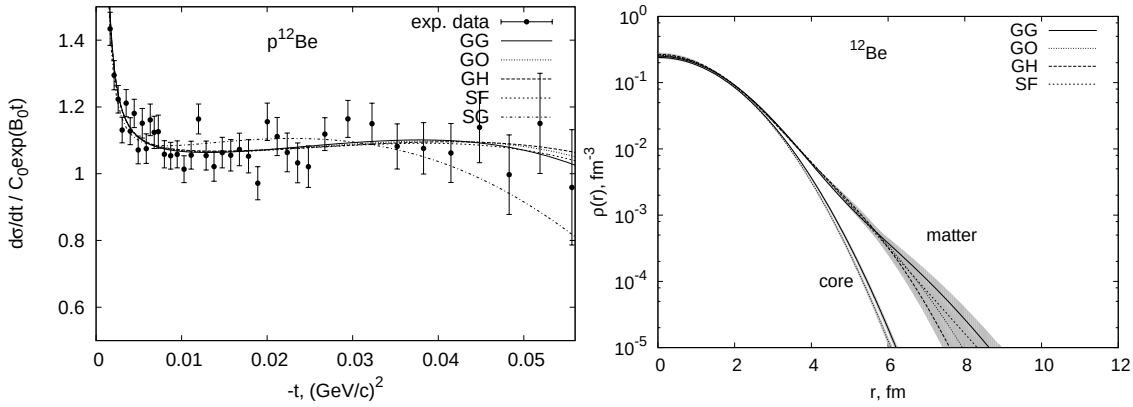

Figure 2.1: Many-body nuclear density distribution of the ^{12}Be isotope obtained from the mean value of different parameterizations (left). The deduced matter and core density distributions are obtained with different parameterizations (right). The error band is the sum of the individual error bands. Taken from [Ili11].

of collinear laser spectroscopy was applied to the beryllium isotopes $^{9-11}$Be and to the short-lived isotope ^{12}Be.

2.2 Nuclear Shell Model

In contrast to atomic physics, where a central Coulomb potential describes the electromagnetic interaction between the electrons and the nucleus which is fairly well known, the strong interaction between the individual nucleons is much less understood in nuclear physics. The Nuclear Shell Model uses, *e.g.*, a Woods-Saxon potential to describe such a nucleon-nucleon interaction in an effective mean field caused by the remaining nucleons [May02]. Starting from the non-relativistic Hamiltonian of an N-nucleon system the Hartree-Fock method is applied to approximate an effective mean field with a Hamiltonian

$$\mathrm{H} = \sum_{i}^{N}(\mathrm{T}_i) + \sum_{i<j}^{N}(\mathrm{V}_{ij}) \tag{2.3}$$

where T_i denotes the kinetic energy and V_{ij} the nucleon-nucleon-potential. For a good approximation V_{ij} is substituted by a mean potential V_i which describes the interaction of all other nucleons $i = 1...N$ to the i-th nucleon

$$\mathrm{H} = \mathrm{H}_0 + \mathrm{V}_{\mathrm{ww}} \tag{2.4}$$

$$\mathrm{H} = \sum_{i}^{N}(\mathrm{T}_i + \mathrm{V}_i) + \underbrace{\sum_{i<j}^{N}(\mathrm{V}_{ij}) - \sum_{i}^{N}(\mathrm{V}_i)}_{\mathrm{V}_{\mathrm{ww}}}. \tag{2.5}$$

where V_{ww} denotes the residual interaction and should be $V_{ww} \ll H_0$. A corresponding effective mean-field potential of all nucleons can be a Woods-Saxon-Potential, which approximates the density distribution of the nucleons:

$$V(r)_{(mean)} = -V_{(0)} \left[1 + e^{\frac{r-R}{a}}\right]^{-1} \tag{2.6}$$

Here the parameter R denotes the size (radius) of the nucleus and a the skin thickness. The solution of Schrödinger's Equation corresponding to Eq. 2.3 with the effective mean field Woods-Saxon potential (Eq. 2.6) leads to discrete energy levels. Similar to the atomic structure a spin-orbit coupling occurs as well in the nucleus. But it is much stronger than in the case of the electrons and its influence on the energy level structure is therefore much stronger. Hence, Eq. 2.3 has to be modified by the radial function $V_{\mathbf{l}\cdot\mathbf{s}}(r)(\mathbf{l}\cdot\mathbf{s})$ to

$$V_{(i)} = V(r)_{(mean)} + V_{\mathbf{l}\cdot\mathbf{s}}(r)(\mathbf{l}\cdot\mathbf{s}) \tag{2.7}$$

According to Eq. 2.7 the potential energy can be calculated for two cases

$$V(r)_{(mean)} + \frac{1}{2}V_{ls}(l) \qquad \text{if} \quad j = l + \frac{1}{2} \tag{2.8}$$

$$V(r)_{(mean)} - \frac{1}{2}V_{ls}(l+1) \quad \text{if} \quad j = l - \frac{1}{2}. \tag{2.9}$$

Since $V_{ls}(r)$ and $V(r)_{(mean)}$ are both negative, energy levels for $j = l - \frac{1}{2}$ are energetically higher than those where $j = l + \frac{1}{2}$. Subtracting Eq. 2.8 and Eq. 2.9 shows that the energy splitting between two levels is proportional to

$$\Delta E \approx l + (l+1) = 2l + 1 \tag{2.10}$$

The introduction of the spin-orbit coupling enabled the nuclear shell model to confirm all observed extraordinary stable "magic nuclei". If the number of protons and/or neutrons matches a magic number $Z, N = 2, 8, 20, 28, 50, 82, 126$ the nucleus is called magic or doubly magic nucleus. Examples are ${}^{4}_{2}\mathrm{He}$ and ${}^{16}_{8}\mathrm{O}$, ${}^{40}_{20}\mathrm{Ca}$ for doubly magic stable nuclei. In this case the separation energy $S_{(n,p)}$ of the next nucleon that is added is usually much smaller, since the next nucleon must inhabit the next shell and, thus, has reduced binding energy. It should be noted that the isotope ${}^{11}\mathrm{Li}$ and ${}^{12}\mathrm{Be}$ are $N = 8$-magic nuclei, far-away from stability.

Similar to the rare gases, a closed shell can be regarded as inert as long as the available energies are small. Thus, the properties of nuclides are determined by the nucleons outside the closed shells. The nuclear spin I can easily be determined by the number of coupling nucleons. In case of an even-even nucleus (even number of protons and neutrons) the ground-state nuclear spin I is always zero. For an even-odd nucleus the total angular momentum of the unpaired nucleon determines the spin $I = j$. For an odd-odd nucleus the spin I is predicted by the Nordheim rule:

$$|j_p - j_n| \leq I \leq j_p + j_n \tag{2.11}$$

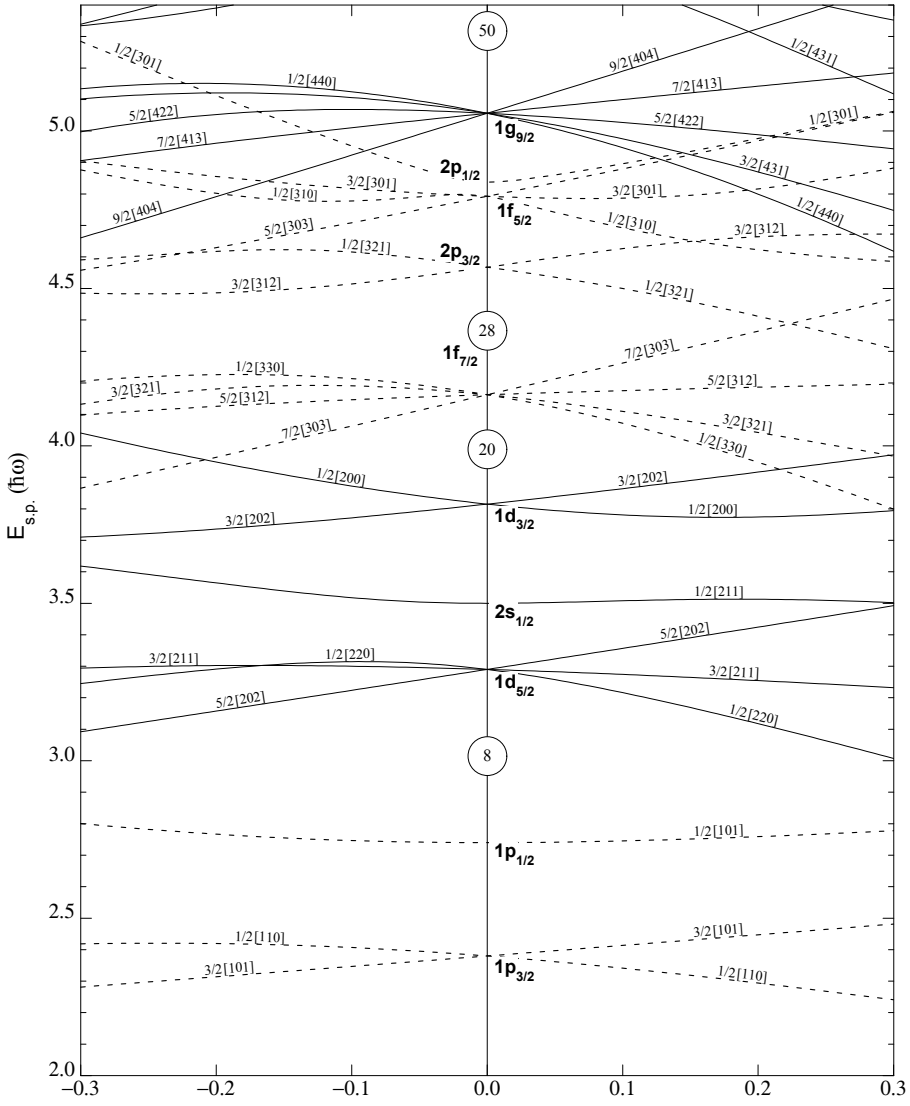

Figure 2.2: The Nilsson Diagram shows the one particle states of a deformed potential. The energy levels are plotted versus the deformation parameter δ. Picture taken from [Fir96].

where $j_{p,n} = l_{p,n} \pm 1/2$.
Doubly magic nuclei and isotones and isotopes around the magic nuclei are mostly spherically symmetric, whereas deformation occurs predominantly for nuclei that have a larger number of nucleons in partially filled orbitals. This is a consequence of the attractive residual interaction between paired nucleons $V_{ww} \approx 1 - 2$ MeV (see Eq. 2.4). For comparison the distance between shell closures is of the order of a few 10 MeV [May02]. Compared to the total binding energy the pairing energy comprises just a small fraction, but it defines the coupling of the valence-nucleons and thus determines the nuclear properties like spin, magnetic moment and electronic quadrupole moment.
The Nilsson Model extends the Nuclear Shell Model aiming to describe single-particle states of deformed nuclei. S. G. Nilsson suggested an anisotropic harmonic oscillator potential $V(r) = \frac{m}{2}\omega^2 r^2$ as an effective mean field potential to describe deformed nuclei with a rotational symmetry along the symmetry axis z [Nil55]. To build the Hamiltonian several correction terms $D\ell^2$ and the spin-orbit coupling term $C\ell \cdot \mathbf{s}$ were empirically added to reproduce the magic numbers

$$V_i = \frac{m}{2}\left[\omega_{xy}^2\left(x^2 + y^2\right) + \omega_z^2 z^2\right] + C\mathbf{l} \cdot \mathbf{s} + D\mathbf{l}^2 \tag{2.12}$$

The numerical solution of Schrödinger's Equation are plotted in the so-called Nilsson Diagrams partially shown in Fig. 2.2. The level energies are plotted versus the deformation parameter δ, where the left side shows the oblate and the right side prolate deformation. Each level is characterized by a set of quantum numbers $[N, n_z, l_z]$, where N is the quantum number of the major shell, n_z the number of nodes in the wave function along the z axis and l_z the projection of the angular momentum component onto the symmetry axis.
The Nilsson Diagram shows that an increased deformation of the nucleus pushes some of the energy level close to the low lying level or even inverts the level structure. The origin of these intruder states is the pairing interaction and the energy gain of the residual proton-neutron interaction [Hey87]. In some nuclei these correlations degenerate states in such a way that a particle-hole excitation is involved across a shell gap. Close to the drip line this effect weakens the shell gap [Bro02].
A prime example is the region around $N = 20$, the so-called *Island of Inversion*. In mass measurements of sodium isotopes it was found that the neutron separation energy do not indicate a shell closure at $N = 20$ [Thi75]. In terms of collinear spectroscopy the ground state properties of magnesium isotopes were investigated. Anomalous spin and magnetic moments were referred to intruder configurations, which are caused due to the filling of the pf-shell before the sd-shell is fully occupied [Yor11].

2.3 Fermionic Molecular Dynamic Model

The Nuclear Shell Model fails in the description of nuclei featuring halo formations or cluster effects leading to molecule-like structures. This is due to the fact that the spatially compact harmonic oscillator states used in the Shell Model can hardly model the long tails

Table 2.1: Charge and matter radii of the beryllium isotopic chain from the FMD model [Nef11]. All values are given in fm.

Isotope	**Charge radii**	**Charge radii** 0_2^+	**Matter radii**
^{7}Be	2.67		2.37
^{9}Be	2.58		2.44
^{10}Be	2.43		2.23
^{11}Be	2.52		2.80
^{12}Be	2.43	2.57	2.52
^{14}Be	2.58	2.62	2.74

of halo-nuclei. A more fundamental microscopic approach is based on nucleon-nucleon potentials and three-nucleon interactions. These are usually fitted to the phase shifts of nucleon-nucleon-scattering and the binding energies of the lightest nuclei, respectively. Such an approach is the Greens-Function Monte-Carlo model that uses the Argonne V18 potential and a variety of three-body interactions (Illinois 2..7) [Wir95]. Sometimes the three body part is encapsulated in an effective two-body potential that is chosen to simulate the effect of the three-body forces. So-called *ab initio* approaches, like the Greens-Function Monte-Carlo calculations [Pie01] or the No-Core Shell Model [For11], allow the description of exotic nuclei modeling the nuclear structure from basic principles *e.g.* nucleon-nucleon interaction.
The No-Core Shell Model is also an ab-initio approach based on harmonic oscillator states but - as indicated above - huge model spaces are required to reproduce the tails in the nucleon distribution of halo nuclei and the convergence is rather slow [For11]. To reduce the complexity of the calculations, cluster models do not start from the description of individual nucleons but consider the fact that the light nuclei can often be treated as composed of sub-structure like α particles, deuterons (d) and tritons (t). Experimental evidence comes from low cluster thresholds in light nuclei, *e.g.* it is easier to remove a deuteron from ^{6}Li than a single proton or neutron.
The Fermionic Molecular Dynamics approach aims to describe exotic nuclei especially with occurring halo- or cluster-formation. These clusters naturally arise in the FMD approach [Fel97, Nef08]. The following paragraph is based on [Nef08, Nef08b] and gives a short introduction into the idea of Fermionic Molecular Dynamics calculations.
The FMD basis states are Slater determinants

$$|Q\rangle = A \ \{|q_1\rangle \otimes ... \otimes |q_A\rangle\} \tag{2.13}$$

where A denotes the Antisymmetrization operator. A single-particle state $|q\rangle$ is given by a single (or a superposition of) Gaussian wave packet(s)

$$\langle \mathbf{x}|q\rangle = \sum_i c_i \exp\left\{-\frac{(\mathbf{x}-\mathbf{b}_\mathrm{i})^2}{2\mathrm{a}_\mathrm{i}}\right\} |\chi_\mathrm{i}^{\uparrow}, \chi_\mathrm{i}^{\downarrow}\rangle \otimes |\xi\rangle. \tag{2.14}$$

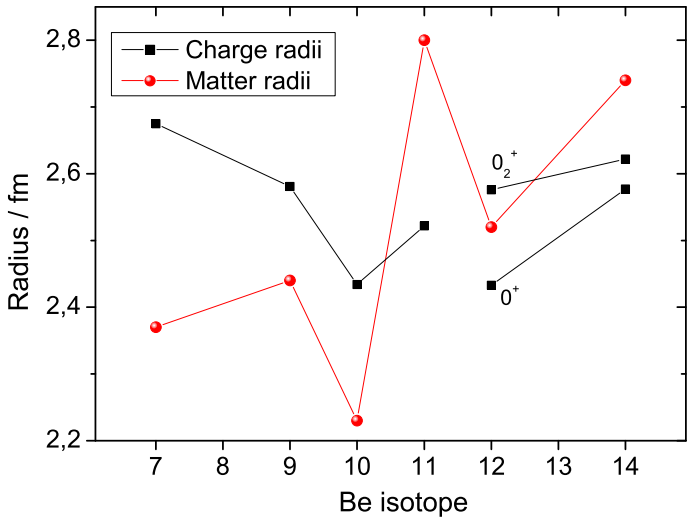

Figure 2.3: The nuclear charge and matter radii of the beryllium isotopic chain from the Fermionic Molecular Dynamics approach [Nef11]. The charge radii of ^{12}Be and ^{14}Be are plotted for the 0^+ and the second 0^+_2 states, which are nearly pure p^2 and $(sd)^2$ configurations.

The complex parameter **b** includes the mean position and momentum of the wave packet. The spread of the wave packet is described by the parameter a and the spin by the spinor χ. The isospin ξ is $+1$ for a proton $+1$ and -1 for a neutron.
In the simplest mean-field picture the energy $E(Q) \geq E_{\mathrm{GS}}$ can be derived varying the many-body state $|Q\rangle$ in the time independent Ritz variation on the intrinsic Hamilton $H_{\mathrm{int}} = H - T_{\mathrm{CM}}$

$$\delta \frac{\langle Q\,|H - T_{\mathrm{CM}}|\,Q\rangle}{\langle Q|Q\rangle} = 0. \tag{2.15}$$

concerning all single-particle parameters. The internal motion and the center-of-mass motion are entangled in the Slater determinant. The effective interaction between the nucleons in the Hamiltonian is derived from the Argonne V18 potential [Wir95] using the Unitary Correlation Operator Method (UCOM) [Nef03] which includes strong short-range and tensor correlations. In Eq. 2.15 the kinetic energy T_{CM} of the center of mass motion is subtracted since only the properties of the intrinsic states are of interest. This variation is a minimization of the expectation value of the Hamilton operator. Therefore the ground state is that many-body state $|Q\rangle$ where an absolute minimum of the energy $E_{\mathrm{GS}} = \langle Q_{\mathrm{GS}}\,|H|\,Q_{\mathrm{GS}}\rangle$ is found according to the variation of all parameters. In this mean-field approach the many-body state may break the symmetries of the Hamiltonian. The intrinsic state $|Q\rangle$ is therefore projected on parity, angular momentum and total linear momentum.
The invariance of the wave function under translation is restored by the projection on the total momentum $P = 0$. The projection can be large especially for heavier nuclei. Therefore, the so-called variation after projection (VAP) calculations are costly and thus,

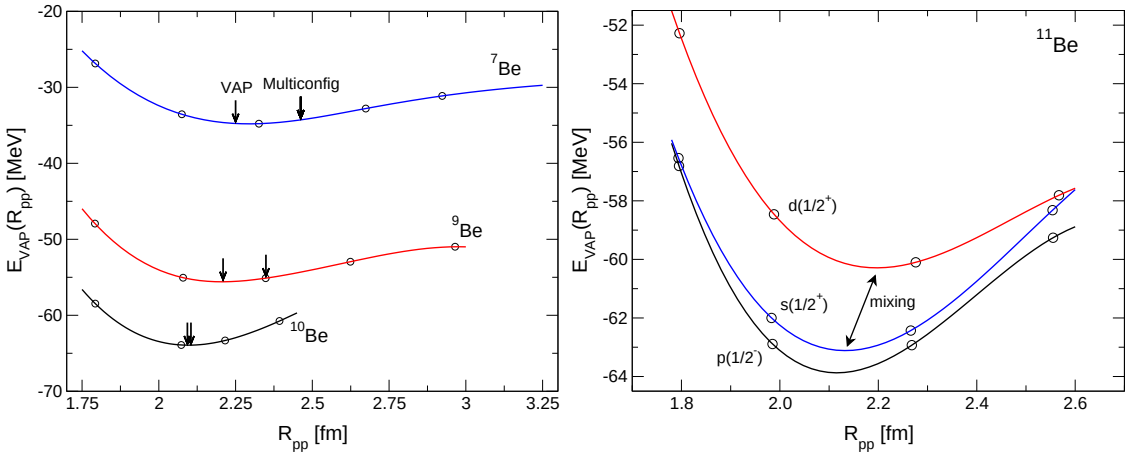

Figure 2.4: Energies of FMD configurations for ^{7,9,10}Be (left) and for ^{11}Be (right). The proton radius R_{pp} relative to the center of charge is a constraint for the intrinsic states in the FMD calculations. The arrows indicate the expectation value R_{pp} obtained either in the variation after projection minimum or in a multiconfiguration mixing calculation. Taken from [Zak10, Nef11].

are performed for light nuclei only. For heavier nuclei the energy minimization is done under constraints, such as the radius or quadrupole deformation and the minimum in energy is derived from the energy surface. In this thesis the experimentally determined charge radii of the beryllium isotopes benchmark the prediction of the FMD model based on improved VAP calculations, the VAP multi-configuration approach. The set of the projected intrinsic states $|Q\rangle$, obtained by energy minimization for the parity and angular momentum projected states, represents the basis of a many-body system. If the Hamiltonian is thus diagonalized in this basis, the eigenstates can be expressed in terms of mixed eigenstates expanded in the basis of projected states. The energy spectra as well as the charge and matter radii were calculated by the VAP multi-configuration [Nef08]. The calculated nuclear charge and matter radii are listed in Tab. 2.1 and are shown in Fig. 2.3. The charge radius decreases from ^{7}Be towards ^{10}Be and increases again up to ^{11}Be due to its halo formation. The charge radius of ^{12}Be is calculated from the local minimum in energy and indicated as 0^+. It corresponds to a nearly pure p^2 configuration and is comparable in size with ^{10}Be. However, the second 0^+ state, indicated as 0^+_2, is strongly influenced by an admixture of $(sd)^2$ orbitals. Hence, the charge radius of the 0^+_2 state is more extended than the 0^+ ground state and ^{11}Be, respectively. The trend of the nuclear charge radius is explained in [Zak10] by an underlying cluster nature of light nuclei which is also present in, *e.g.*, ^{12}C, ^{16}O and ^{24}Mg [Fre07]. In a cluster model, ^{7}Be consists of an α particle and a ^{3}He nucleus, the unbound ^{8}Be of $(\alpha + \alpha)$ particles and in case of ^{9}Be the additional neutron glues the two α particles together. ^{10}Be is well bound and the distance between the two α particles is rather small. Such a pronounced α-clustering in beryllium isotopes were obtained in previous FMD calculation by a variation of energy after projection (VAP) as a result of the proton and neutron densities of the intrinsic states [Zak10].

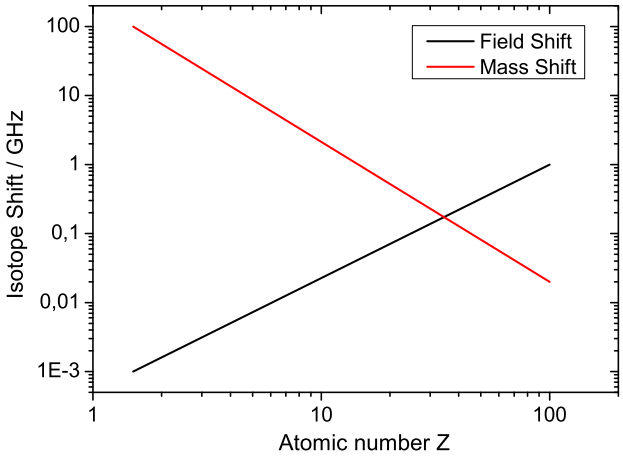

Figure 2.5: Rough contribution of the mass shift and the field shift to the isotope shift as a function of the atomic numbers Z.

Assuming no core polarization, a proton radius R_{pp} can be defined relative to the *center of charge*. It is a measure for the distance of the two α-clusters and it should be stressed, that this proton radius significantly differs from the nuclear charge radius which is the proton charge distribution relative to the *center of mass*. The results of VAP calculations with constraint on the proton radius R_{pp} are presented in Fig. 2.4 which shows the energy surface as a function of the proton radius R_{pp} for each isotope. The arrows indicate the R_{pp} expectation value obtained by an unconstrained VAP (single configuration) and by variation of the energy in a multiconfiguration calculation (linear combination of the obtained intrinsic states of different R_{pp}). The energy surfaces of ^{7}Be and ^{9}Be show similar behavior and are both flat. By contrast, in ^{10}Be the energy surface is much steeper and thus no extended configurations contribute to the ground state. The distances between the single- and multiconfiguration results of the obtained energy minima decrease from ^{7}Be to ^{9}Be and practically coincide for ^{10}Be. The decreasing R_{pp} values correspond to cluster distances of 4.23 fm (^{7}Be), 4.08 fm (^{9}Be) and 3.51 fm (^{10}Be) [Zak10].
The configuration completely differs in case of ^{11}Be since the additional neutron might either occupy the $p_{1/2^-}$ orbit, $s_{1/2^+}$ orbit, or a mixture of both. Therefore, further many-body states must be varied in the multiconfiguration calculation. In Fig. 2.4 (right) the mixing of the energy surfaces $s_{1/2^+}$ (blue) ($p_{1/2^-}$ (black)) orbit and the $d_{5/2^+}$ (red) coupled with ^{10}Be(2^+) to spin $d_{1/2^+}$ is indicated. However, multiconfiguration mixing increases R_{pp} relative to ^{10}Be only slightly, since the proton radius R_{pp} of ^{11}Be and ^{10}Be are nearly identical.

2.4 Atomic Physics

The fundamental properties of a nucleus lead to multitudinous changes in the electronic level structure caused by (a) the finite size of the nucleus, (b) the spin and magnetic

moment, (c) the spectroscopic quadrupole moment which is caused by a deformation of the nucleus. While the first one shifts the transition energies from one isotope to another, the other two lead to a splitting of the fine-structure levels of the atom. Both effects are summarized as hyperfine structure. High-precision laser spectroscopy enables us to probe such properties of the nucleus which are apparent in the hyperfine structure of an atomic transition. On-going developments in high resolution laser spectroscopy (see [Che10]) enable to resolve the hyperfine structure of rare exotic nuclei and thus allows the extraction of the fundamental properties of the nucleus with high accuracy.

2.4.1 Isotope Shift

The isotope shift $\delta\nu_{\mathrm{IS}}^{A,A'}$ is the frequency difference in an electronic transition ν^A between two isotopes A and A' of the same element $\delta\nu_{\mathrm{IS}}^{A,A'} = \nu^{A'} - \nu^A$. If nuclear moments cause hyperfine splitting, the electronic transition frequency ν^A is the center of gravity (cg) of all hyperfine components. Since the isotope shift $\delta\nu_{\mathrm{IS}}^{A,A'}$ arises due to a change of the nuclear mass and the finite size of the nucleus, it can be expressed by the sum of the so called mass shift $\delta\nu_{\mathrm{MS}}^{A,A'}$ and field shift $\delta\nu_{\mathrm{FS}}^{A,A'}$ [Ott89]

$$\delta\nu_{\mathrm{IS}}^{A,A'} = \delta\nu_{\mathrm{MS}}^{A,A'} + \delta\nu_{\mathrm{FS}}^{A,A'}. \tag{2.16}$$

The mass shift originates from the change of the nuclear mass which influences the kinetic energy of the electron caused by the nuclear motion. Except for hydrogen-like spectra where the mass shift contribution is given by the normal mass shift $\delta\nu_{\mathrm{NMS}}^{A,A'}$, a correlation of electron momenta influences the nuclear motion leading to the specific mass shift $\delta\nu_{\mathrm{SMS}}^{A,A'}$

$$\delta\nu_{\mathrm{MS}}^{A,A'} = \delta\nu_{\mathrm{NMS}}^{A,A'} + \delta\nu_{\mathrm{SMS}}^{A,A'} = (N+S)\frac{M_A - M_{A'}}{M_A M_{A'}}. \tag{2.17}$$

Since both terms have the same A-dependence, they can be summarized introducing the normal and specific mass shift parameters $N = m_e \cdot \nu^A$ and S. It should be noted that N has to be positive whereas S can also be negative depending on the electron correlations. It was found experimentally that $|\mathrm{S}| \leq \mathrm{N}$ for common $s \rightarrow p$ transitions. In contrast, the specific mass shift parameter S can be one order of magnitude bigger than N if d- or f-electrons are involved [Hei74]. While $\delta\nu_{\mathrm{NMS}}^{A,A'}$ can easily be calculated, $\delta\nu_{\mathrm{SMS}}^{A,A'}$ exhibits a challenge. Since now it is only possible to calculate $\delta\nu_{\mathrm{SMS}}^{A,A'}$ for systems with up to three-electrons [Yan08, Yan08b, Puc08] with high spectroscopic accuracy (see Section 2.5).
The field shift contribution $\delta\nu_{\mathrm{FS}}^{A,A'}$ in Eq. 2.16 arises due to the change of the finite size and angular shape of the charge distribution when adding neutrons to the nucleus. This influence on the electronic binding energy of electrons can be derived nonrelativistically in first order perturbation theory. The electrostatic energy E of a nuclear charge distribution

$\rho_N(\mathbf{r})$ in an s-electron potential $V(\mathbf{r})$ can be derived as

$$E = \int_{r<R_1} \rho_N(\mathbf{r}) V(\mathbf{r}) d^3\mathbf{r}. \tag{2.18}$$

If the electron density is assumed to be constant over the nuclear volume, the potential at the nuclear site can be separated into a constant and a variable part, where the latter describes the distribution in the nucleus [Ott89]

$$E = -Ze^2\ V(0) + \frac{2\pi}{3} Ze^2 \left|\Psi(0)\right|^2 \left\langle r_c^2 \right\rangle . \tag{2.19}$$

Here the first term denotes the interaction of the s-electron with a point-like source, which is corrected by the finite-size contribution. For a transition, only the change of the electron density between the lower and the upper state $\Delta \left|\Psi(0)\right|^2$ is relevant for the finite size effect. The contribution to the electronic spectra is about 10^{-6} for heavy and 10^{-9} for light nuclei. Even though such accuracies are available experimentally, the separation of the field effect in the transition frequency from other effects, *e.g.*, the specific mass shift, can still not be performed for other than hydrogen-like spectra. Hence, the mean square charge radius $\left\langle R_c^2 \right\rangle$ can not be determined directly. But it is possible to extract the change of the nuclear charge radius $\delta \left\langle r_c^2 \right\rangle^{A,A'}$ by measuring the isotope shift, where the first term in Eq. 2.19 cancels

$$\delta\nu_{\mathrm{FS}}^{A,A'} = -\frac{2\pi}{3} Ze^2 \Delta \left|\Psi(0)\right|^2 \delta \left\langle r_c^2 \right\rangle^{A,A'} . \tag{2.20}$$

Introducing the field shift coefficient $F = -\frac{2\pi}{3} Ze^2 \Delta \left|\Psi\left(0\right)\right|^2$ Eq. 2.20 can be written as

$$\delta\nu_{FS}^{A,A'} = F \delta \left\langle r_c^2 \right\rangle^{A,A'} . \tag{2.21}$$

For the beryllium isotopes Yan *et al.* [Yan08, Yan08b] and Puchalski *et al.* [Puc10] calculated the parameter F independently from each other to -16.912 MHz/fm^2. Table 2.2 shows the results for the beryllium isotopes. The Eq. 2.17 and Eq. 2.21 can be inserted into Eq. 2.16 to obtain the common expression for the isotope shift which directly yields the spectroscopically accessible parameter $\delta \left\langle R_c^2 \right\rangle$

$$\delta\nu_i^{A,A'} = (N+S) \cdot \frac{M_A - M_{A'}}{M_A M_{A'}} + F_i^{A,A'} \delta \left\langle r_c^2 \right\rangle . \tag{2.22}$$

In order to extract the absolute charge radius from an isotope shift measurement, the nuclear charge radius of at least one isotope has to be determined by a different method, *e.g.*, elastic electron scattering. In this thesis the charge radius of the stable beryllium isotope ^{9}Be which was determined from electron scattering experiments [Jan72, Jag74] to $R_c(^9\mathrm{Be}) = 2.519 \pm 0.012$ fm is used as a reference radius. If such a reference radius is available the absolute charge radii can be calculated according to

$$R_c(A') = \sqrt{R_c^2(A) + \delta \left\langle r_c^2 \right\rangle^{A,A'}}. \tag{2.23}$$

Table 2.2: Summary of mass shift contributions for the $2s\ ^2S_{1/2} \rightarrow 2p\ ^2P_{1/2,3/2}$ transitions in Be^+ with respect to $^9Be^+$. The first uncertainty originates from unknown higher order terms whereas the second uncertainty is due to the atomic mass. All values are given in MHz.

Isotope	$2S_{1/2} \rightarrow 2P_{1/2}$	$2S_{1/2} \rightarrow 2P_{3/2}$	Field shift parameter F	Reference
$^7Be^+$	-49 225.744(35)(9)	-49 231.779(35)(9)	-17.021(31)	[Puc09]
	-49 225.779(38)	-49 231.828(38)	-16.912	[Dra02]
$^{10}Be^+$	17 310.459(13)(11)	17 312.553(13)(11)	-17.027(31)	[Puc09]
	17 310.442(12)	17 312.569(12)	-16.912	[Dra02]
$^{11}Be^+$	31 560.245(31)(12)	31 564.207(31)(12)	-17.020(31)	[Puc09]
	31 559.990(24)	31 563.868(24)	-16.912	[Dra02]
$^{12}Be^+$	43 390.180(30)(180)	43 395.480(30)(180)	-17.022(31)	[Puc10]
	43 390.168(39)	43 395.499(39)	-16.912	[Dra10]

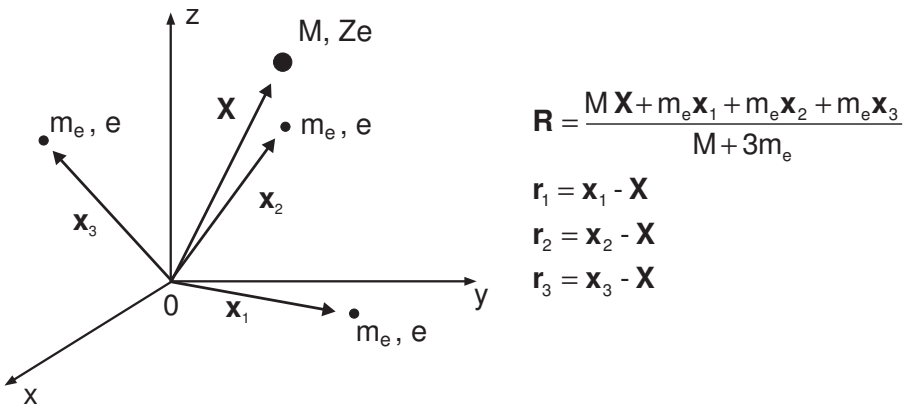

Figure 2.6: A reference frame for a three-electron system. The center-of-mass transformation introduces relative vectors $\mathbf{r}_i$ as well as the center-of-mass vector $\mathbf{R}$. Taken from [San05].

The sizes of the mass and field shift contributions to the isotope shift depend strongly on the atomic number Z as depicted in Fig. 2.5. While the mass shift scales roughly as $1/A$, the field shift increases with $Z^2/\sqrt{A}$. For the lightest elements the field shift contributes only on the order of 100 kHz to a few MHz, whereas the dominating mass shift is of the order of several tens of GHz. Since now, only mass shift calculations up to three-electron systems [Yan08, Yan08b, Puc09] reach the required accuracy to extract the charge radius for these light isotopes. Therefore spectroscopy was applied to lithium-like beryllium ions in order to extract the change of the nuclear charge radius from the field shift contribution in an appropriate manner (about 1 MHz).

2.5 Mass Shift Calculations of Lithium-like Beryllium

According to Eq. 2.17 the mass shift consists of a normal mass shift and a specific mass shift contribution. While the normal mass shift calculation is trivial, the latter exhibits a quite challenging task since it includes electron correlation and quantum electrodynamic effects. Significant theoretical effort expedited the accurate treatment of the slowly convergent numerical calculation of the correlation integrals [Dra99]. The precise mass shift calculations of 2- and 3-electron-systems improved to a numerical accuracy of the non-relativistic energy of $\sim 10^{-20}$ for helium and $\sim 10^{-12}$ for lithium and beryllium [Yan00, Yan02, Dra05]. The following section gives an idea of the mass shift calculations in 3-electron-systems and is based on the article [Dra05]. In a first step the nonrelativistic energy E_{NR} of a correlated three-electron-system orbiting a nucleus is derived from Schrödinger's Equation. The Hamiltonian in a reference frame, such as shown in Fig. 2.6, can be written as

$$H = -\frac{\hbar^2}{2M}\boldsymbol{\nabla}_X^2 - \frac{\hbar^2}{2m_e}\boldsymbol{\nabla}_{x_1}^2 - \frac{\hbar^2}{2m_e}\boldsymbol{\nabla}_{x_2}^2 - \frac{\hbar^2}{2m_e}\boldsymbol{\nabla}_{x_3}^2 \tag{2.24}$$

$$- \frac{Ze^2}{|\mathbf{X}-\mathbf{x}_1|} - \frac{Ze^2}{|\mathbf{X}-\mathbf{x}_2|} - \frac{Ze^2}{|\mathbf{X}-\mathbf{x}_3|} \tag{2.25}$$

$$+ \frac{e^2}{|\mathbf{x}_2-\mathbf{x}_1|} + \frac{e^2}{|\mathbf{x}_3-\mathbf{x}_1|} + \frac{e^2}{|\mathbf{x}_3-\mathbf{x}_2|}. \tag{2.26}$$

A center-of-mass transformation introduces the center-of-mass coordinate $\mathbf{R}$ and the relative coordinates $\mathbf{r}_i$ to eliminate the center-of-mass motion. Considering the reduced mass $\mu = m_e M/(m_e + M)$ the distances are rescaled to $\boldsymbol{\rho}_i = \mathbf{r}_i(\mu e^2/\hbar^2)$ and the nonrelativistic energy E_{NR} according to

$$\mathcal{E} = \left(\frac{m_e}{\mu}\right)\frac{E_{\mathrm{NR}}\hbar^2}{e^4} = \frac{E_{\mathrm{NR}}}{2R_\infty(1-\frac{\mu}{M})}\ , \tag{2.27}$$

with R_∞ as the Rydberg constant. Schrödinger's Equation follows as

$$\left(\underbrace{-\frac{1}{2}\sum_{i=1}^{3}\nabla_{\rho_i}^2}_{E_{\mathrm{kin}}\ \mathrm{incl.MS}} \underbrace{- Z\sum_{i=1}^{3}\frac{1}{\rho_i}}_{\mathrm{Coulomb-term}} \underbrace{+\sum_{i>j}^{3}\frac{1}{|\boldsymbol{\rho}_i-\boldsymbol{\rho}_j|}}_{\mathrm{ee-term}} \underbrace{-\frac{\mu}{M}\sum_{i>j}^{3}\boldsymbol{\nabla}_{\rho_i}\cdot\boldsymbol{\nabla}_{\rho_j}}_{\mathrm{Mass\ polarization}}\right)\Psi = \mathcal{E}\Psi. \tag{2.28}$$

The Hamiltonian in Eq. 2.28 can be separated into

$$\left(H_0 + \left(-\frac{\mu}{M}\right)H_1\right)\Psi = \mathcal{E}\Psi, \tag{2.29}$$

where H_0 includes the normal mass shift contribution and $H_1 = \sum_{i>j}^{3}\boldsymbol{\nabla}_{\rho_i}\cdot\boldsymbol{\nabla}_{\rho_j}$ the specific mass shift or mass polarization term.

The solution wave functions Ψ_0 of H_0 are obtained using the variation principle in a basis set of Hylleraas coordinates. Then Eq. 2.29 is expanded in the time-independent perturbation theory with the perturbation factor $\lambda = \left(\frac{\mu}{M}\right)$:

$$\psi = \psi_0 + \lambda\psi_1 + \ ... \tag{2.30}$$

$$\mathcal{E} = \mathcal{E}_0 + \lambda\mathcal{E}_1 + \lambda^2\mathcal{E}_2 + \ ... \tag{2.31}$$

In a second step the obtained nonrelativistic wave functions are used to include relativistic and QED corrections to E_{NR}. The total energy E_{tot} of an electronic configuration is given as an expansion series in the fine structure constant $\alpha = e^2/\hbar c$ by

$$E_{\mathrm{tot}} = E_{\mathrm{NR}} + \alpha^2 E_{\mathrm{REL}} + \alpha^3 E_{\mathrm{QED}} + ... + E_{\mathrm{FS}}. \tag{2.32}$$

Here E_{REL} denotes the relativistic correction term, E_{QED} the quantum electrodynamic correction and E_{FS} the contribution of the nuclear finite size effect. It is convenient to expand these contributions in terms of μ/M

$$\begin{aligned} E_{\mathrm{NR}} &= E^{(0)}_{\mathrm{NR}} + \left(\tfrac{\mu}{M}\right) E^{(1)}_{\mathrm{NR}} + \left(\tfrac{\mu}{M}\right)^2 E^{(2)}_{\mathrm{NR}} + ... \\ E_{\mathrm{REL}} &= E^{(0)}_{\mathrm{REL}} + \left(\tfrac{\mu}{M}\right) E^{(1)}_{\mathrm{REL}} + ... \\ E_{\mathrm{QED}} &= E^{(0)}_{\mathrm{QED}} + \left(\tfrac{\mu}{M}\right) E^{(1)}_{\mathrm{QED}} + ... \ . \end{aligned} \tag{2.33}$$

It should be noted that E_{FS} is the finite size correction term as mentioned in Chapter 2.4.1 and is therefore given by

$$E_{\mathrm{FS}} = \frac{2\pi Z e^2 \left\langle {r_{\mathrm{c}}}^2 \right\rangle}{3} \left\langle \sum_{i=1}^{3} \delta(\mathbf{r}_i) \right\rangle. \tag{2.34}$$

The expectation value $\left\langle \sum_{i=1}^{3} \delta(\mathbf{r}_i) \right\rangle$ is nothing else than $|\psi_e(0)|$ from Eq. 2.19 and describes the expectation value of the electron density at the nucleus. The contributions to the transition energy in $^9\mathrm{Be}^+$ in the $2s\ ^2\mathrm{S}_{1/2} \rightarrow 2p\ ^2\mathrm{P}_{1/2}$ transition are listed in Tab. 2.3. It is shown that the zeroth order QED correction term $E^{(0)}_{\mathrm{QED}}$, resulting in an energy shift caused by the electron self-energy and vacuum polarization terms [Dra06, Yan08] , contributes with an uncertainty comparable in size to the nuclear finite volume terms. This uncertainty restricts the extraction of the absolute charge radius directly from optical measurements[2]. But, taking the energy difference $\Delta E\,(A, A')$ into account, all mass-independent terms including $E^{(0)}_{\mathrm{QED}}$ vanish . In contrast to $E^{(0)}_{\mathrm{QED}}$ the remaining first order QED term, $E^{(1)}_{\mathrm{QED}}$ in Eq. 2.35, can be calculated to sufficient accuracy. It includes recoil terms due to radiative recoil or Lamb-shift and mass polarization terms.
The isotope shift, which is the energy difference ΔE between the electronic transitions in

[2]Only recently a programme was started by K. Packucki to complete QED calculations up to the $m\alpha^7$ terms in the $2s\ ^3\mathrm{S}_1 \rightarrow 2p\ ^3\mathrm{P}_J$ transitions in helium-like ions. This gives some prospect to extract also absolute charge radii for two-electron systems [Pac12].

Table 2.3: Contributions to the isotope shift calculations in $^9Be^+$ in the $2s\ ^2S_{1/2} \rightarrow 2p\ ^2P_{1/2}$ transition [Puc08].

Contribution	Order	Mass shift [MHz]
Nonrelativistic energy E_{NR}	λ, λ^2	956 709 540.2(3)
Relativistic corrections E_{REL}	λ	548 061.3(11)
QED corrections (Lamb shift) E_{QED}	λ	-58 126(252)
Finite nuclear size ΔE_{FS}		-107(1)
Total		957 199 368(252)

two isotopes (A, A'), is thus:

$$\begin{aligned} \Delta E\left(A, A'\right) &= \left[\left(\tfrac{\mu}{M}\right)_A - \left(\tfrac{\mu}{M}\right)_{A'}\right]\left(E^{(1)}_{\mathrm{NR}} + \alpha^2 E^{(1)}_{\mathrm{REL}} + \alpha^3 E^{(1)}_{\mathrm{QED}}\right) \\ &+ \left[\left(\tfrac{\mu}{M}\right)^2_A - \left(\tfrac{\mu}{M}\right)^2_{A'}\right] E^{(2)}_{\mathrm{NR}} + ... + E_{\mathrm{FS,A}} - E_{\mathrm{FS,A'}}. \end{aligned} \tag{2.35}$$

Due to the accuracy of the present experiments ($\Delta E\left(A, A'\right) \leq 1$ MHz) higher orders than $\lambda^2 = \left(\frac{\mu}{M}\right)^2$ are neglected. Therefore an absolute charge radius can be extracted if the energy difference $\Delta E\left(A, A'\right)$ which delivers the change of the root mean square charge radius is measured with sufficient accuracy (commonly a few MHz) and can be referred to a known reference radius.

2.5.1 Hyperfine Structure

The nuclear spin **I**, which depends on the number of unpaired nucleons, results in a magnetic dipole moment $\boldsymbol{\mu}_I$ of the nucleus according to [Her08]

$$\boldsymbol{\mu}_I = \frac{g_I \mu_N \mathbf{I}}{\hbar} \tag{2.36}$$

where $\mu_N = \frac{e\hbar}{2m_p}$ denotes the nuclear magneton and g_I the nuclear g-factor.
The electrons induce a magnetic field $\mathbf{B_e}$ at the nucleus which interacts with the nuclear spin-induced magnetic dipole moment $\boldsymbol{\mu}_I$. This interaction causes a coupling of the angular momentum **J** of the electron with the nuclear spin **I** to a total angular momentum $\mathbf{F} = \mathbf{J}+\mathbf{I}$. The eigenstates of the combined system **F** fulfill the angular momentum relations:

$$\hat{F}^2 |JIFm_F\rangle = \hbar^2 F(F+1)|JIFm_F\rangle \tag{2.37}$$

$$\hat{F}_Z |JIFm_F\rangle = m_F \hbar |JIFm_F\rangle. \tag{2.38}$$

The amount of allowed eigenvalues of **F** range from

$$|I - J| \leq F \leq J + I \qquad \text{if} \qquad |\mathrm{I} < \mathrm{J}|\,. \tag{2.39}$$

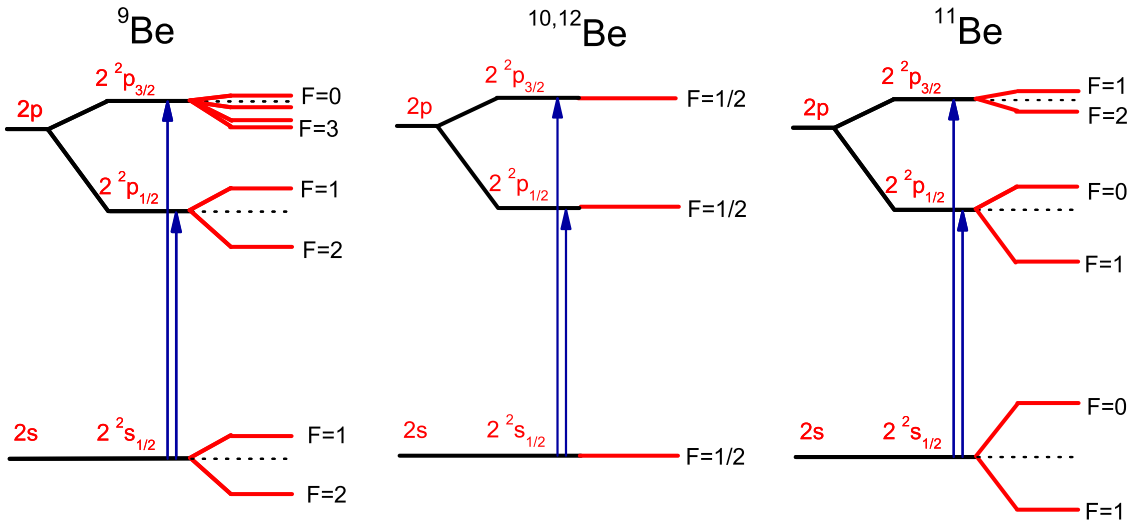

Figure 2.7: The energy level diagram of the investigated transitions in the beryllium isotopes $^{9-12}$Be. The nuclear spins are $I_{^9\mathrm{Be}} = 3/2$, $I_{^{11}\mathrm{Be}} = 1/2$ and $I_{^{10,12}\mathrm{Be}} = 0$. It should be noted that the energy splitting is not scaled.

The energy splitting of the hyperfine structure is calculated according to the Hamiltonian [Dra06b]

$$\hat{H}_{\mathrm{HFS}} = -\boldsymbol{\mu}_I \cdot \mathbf{B_e} \tag{2.40}$$

$$= \frac{\mathbf{I}}{\hbar} \cdot g_I \mu_N B \frac{\mathbf{J}}{\hbar} \tag{2.41}$$

$$= g_I \mu_N \cdot \frac{B}{\hbar^2} \cdot \mathbf{I} \cdot \mathbf{J}. \tag{2.42}$$

Since I and J are not good quantum numbers anymore, we have to replace them according to

$$\mathbf{I} \cdot \mathbf{J} = \frac{1}{2}\left(\mathbf{F}^2 - \mathbf{I}^2 - \mathbf{J}^2\right) = \frac{A}{2}K \tag{2.43}$$

Using Eq. (2.37 - 2.38) and replacing the operator product $\mathbf{I} \cdot \mathbf{J}$ according to Eq. 2.43 in Eq. 2.40 leads to an energy shift ΔE

$$\Delta E = \frac{A}{2}\left(F(F+1) - I(I+1) - J(J+1)\right) = \frac{A}{2}K \tag{2.44}$$

where $A = g_I \mu_N \frac{B\hbar}{J}$ denotes the hyperfine coupling constant and K is the Casimir -Factor. The distance between two neighboring hyperfine structure states denotes the interval rule

$$\Delta E = \Delta E_{F+1} - \Delta E_F = A(F+1). \tag{2.45}$$

The hyperfine level are additionally shifted if the nucleus is deformed and exhibits a

spectroscopic quadrupole moment. In this case the electric field gradient induced by the electrons, interacts with the quadrupole moment

$$\Delta E_{Q_s} = \frac{B}{2} \frac{\frac{3}{4}K(K-1) - I(I+1)J(J+1)}{2I(2I-1)J(2J-1)}. \tag{2.46}$$

Here $B = eQ \left\langle \frac{\partial^2 V_e}{\partial z^2} \right\rangle$ defines the electric quadrupole interaction constant with the electric field gradient $\left\langle \partial^2 V_e / \partial z^2 \right\rangle$. The spectroscopic electric quadrupole moment Q_s influences the hyperfine structure only if $I, J \geq 1$. Thus, for a dipole transition between $J = 1/2$ states this quadrupole term vanishes as well as for nuclei with $I = 1/2$.
The level schemes of the beryllium ions are shown in Fig. 2.7. The black lines represent the fine structure and the red ones the hyperfine structure splitting. The dotted lines show the center of gravity of the hyperfine structure which equals the fine structure splitting. The hyperfine structure of the $2p\ ^2\mathrm{P}_{3/2}$ level can not be fully resolved due to a very small splitting. In order to excite the $2s\ ^2\mathrm{S}_{1/2} \rightarrow 2p\ ^2P_{1/2,3/2}$ transitions a wavelength of about 313 nm is necessary.
The line strength S of an optical transition is defined as the squared transition matrix element $|R_{ul}|^2$ of the multipole operator $\hat{P}$ [Dra06b]:

$$S_{ul} = S_{lu} = |R_{ul}|^2 \tag{2.47}$$

$$R_{ul} = \langle \psi_u | \hat{P} | \psi_l \rangle . \tag{2.48}$$

where ψ_l and ψ_u denote the lower and upper level wave functions. For an allowed transition, *i.e.* an electric dipole transition E1 (see Tab. 2.4), the strength S is directly related to the Einstein A-factor, which is the transition probability between the lower (l) and upper (u) level:

$$A_{lu} = \frac{2\pi e^2}{m_e c \epsilon_0 \lambda^2} \frac{g_l}{g_u} f_{ul} = \frac{16\pi^3}{3h\epsilon_0 \lambda^3 g_u} S. \tag{2.49}$$

Here $g_{l(u)} = (2L_{l(u)} + 1)(2S_{l(u)} + 1)$ are the statistical weights of the lower and upper state respectively, λ the wavelength and $f_{ul} = 2/3\,(\Delta E / g_l)\,S$ the absorption oscillator strength. In case of a forbidden transition, *e.g.* a magnetic dipole transition M1, Eq. 2.49 substantially changes [Dra06b].
If hyperfine splitting occurs the transition strength of the fine structure level is distributed between different hyperfine transitions. The relative intensity of the hyperfine transition $S(F_l \rightarrow F_u)$ can be calculated using the 6j-Wigner-Kronecker symbols

$$S(F_l \rightarrow F_u) = \frac{(2F_l + 1)(2F_u + 1)}{2I + 1} \left\{ \begin{array}{ccc} J_u & F_u & I \\ F_l & J_l & 1 \end{array} \right\}^2 \cdot S(J_l \rightarrow J_u) \tag{2.50}$$

Here, $S(J_l \rightarrow J_u)$ is the transition strength S of the unperturbed fine structure transition(compare Eq. 2.47). The 6j-symbols can be computed using the Racah formula (see handbooks of mathematics).

Table 2.4: Selection rules for optical transitions. The multiple order l of a transition is characterized by the change of the angular momentum caused by the photon [May02].

multipole	electric El			magnetic Ml		
order l	El	$\|\Delta J\|$	ΔP	Ml	$\|\Delta J\|$	ΔP
dipol	E1	1	-	M1	1	+
quadrupol	E2	2	+	M2	2	-

2.6 Extraction of Nuclear Properties from Optical Spectra

Nuclear properties can be derived from an optical spectrum of the fine structure or a hyperfine multiplet. The frequency ν_i of a hyperfine transition (peak) i depends on the hyperfine constants $A_{l,u}, B_{l,u}$ of the **u**pper and **l**ower hyperfine level ([Che10])

$$\nu_i = \nu_{cg} + \alpha_u A_u + \beta_u B_u - \alpha_l A_l - \beta_l B_l, \tag{2.51}$$

where $\alpha = K/2$, $\beta = \frac{3K(K+1)-4I(I+1)J(J+1)}{8I(2I-1)J(2J-1)}$ and ν_{cg} denotes the center of gravity. According to the theoretical hyperfine multiplet a line profile, *e.g.* a Gaussian, Lorentzian or a Voigt profile, is applied to the optical spectra and therefore minimizing χ^2 determines the $A_{l(u)}$ and $B_{l(u)}$ hyperfine constants. It should be noted that four peaks are in most cases already sufficient to determine the hyperfine factors, even if the whole spectrum consists of many more transitions.
Assuming that the magnetic moment μ_{ref} and the electric quadrupole moment Q_{ref} of one isotope is precisely known (mostly from the stable isotope) the nuclear moments μ and Q of another isotope can be derived via the ratios

$$\mu = \mu_{\text{ref}} \frac{IA}{I_{\text{ref}} A_{\text{ref}}} (1 + \epsilon - \epsilon_{\text{ref}}) \underbrace{=}_{\text{point-like nucleus}} \mu_{\text{ref}} \frac{IA}{I_{\text{ref}} A_{\text{ref}}} \tag{2.52}$$

$$Q = Q_{\text{ref}} \frac{B}{B_{\text{ref}}}. \tag{2.53}$$

An extended charge distribution and nuclear magnetization effect influences the width of the hyperfine structure. In Eq. 2.52 this is taken into account by the so called Bohr-Weisskopf correction factor $(1 + \epsilon)$ of each magnetic dipole constant A. Usually, the hyperfine anomaly ϵ which contributes with ($\leq$ 1 %), can only be extracted using RF techniques in order to reach the required precision of better than 10^{-4}.
Furthermore a complete optical spectrum verifies the nuclear spin assumption by the number of peaks if $J \neq I$. And since the A-factor is directly proportional to the magnetic moment μ, it is verified as well.

3 Experimental Technique

This chapter introduces to the experimental technique applied at the nuclear research reactor TRIGA[1] in Mainz and at the ISOLDE facility at CERN. At first, the different ion production mechanisms at both facilities are discussed. Afterwards the approach of collinear laser spectroscopy, wherewith optical transitions in ions and atoms were studied at ISOLDE as well as in Mainz during the work of this thesis, is presented in detail.

3.1 TRIGA-SPEC Project

At the TRIGA research reactor in Mainz a Penning trap mass spectrometer and a collinear laser spectroscopy beamline are installed [Ket08]. This installation is complementary to the COLLAPS and ISOLTRAP experiments at ISOLDE, where the groups involved at TRIGA-SPEC are also pursuing laser and mass spectrometry. Using neutron-induced fission of actinide elements, short-lived neutron-rich isotopes can be produced. While refractory elements are not available at ISOLDE, they are one of the major objectives at TRIGA-SPEC. The TRIGA-SPEC setup is schematically illustrated in Fig. 3.1: A ^{249}Cf target placed inside the beam port B target chamber of the TRIGA reactor is bombarded with neutrons. A gas jet system transports the resulting fission fragments, which are bound to aerosol particles, from the reactor to an ion source at a high-voltage platform. Up to now there are 2 types of ion sources available: a surface ion source and an electron cyclotron resonance plasma ion source. The fission products are separated from the aerosol particles, ionized and accelerated towards the ground potential of the beamline. The resultant ion beam is mass separated by a 90° dipole-magnet and guided into an RFQ cooler and buncher. Subsequently, it releases accumulated ion beam pulses to a switchyard which controls the further guidance either into the Penning trap or to the collinear beamline.

3.1.1 Production of Short-Lived Isotopes at the Research Reactor TRIGA

As depicted in Fig. 3.1 the neutron-induced-fission products are created inside the beam port B of the research reactor. Since the target has to be placed very close to the reactor core it is very difficult to extract the ions using an ion guide technique as it is performed at Jyväskylä [Aey01, Moo08].

[1] **T**raining, **R**esearch, **I**sotopes, **G**eneral **A**tomic

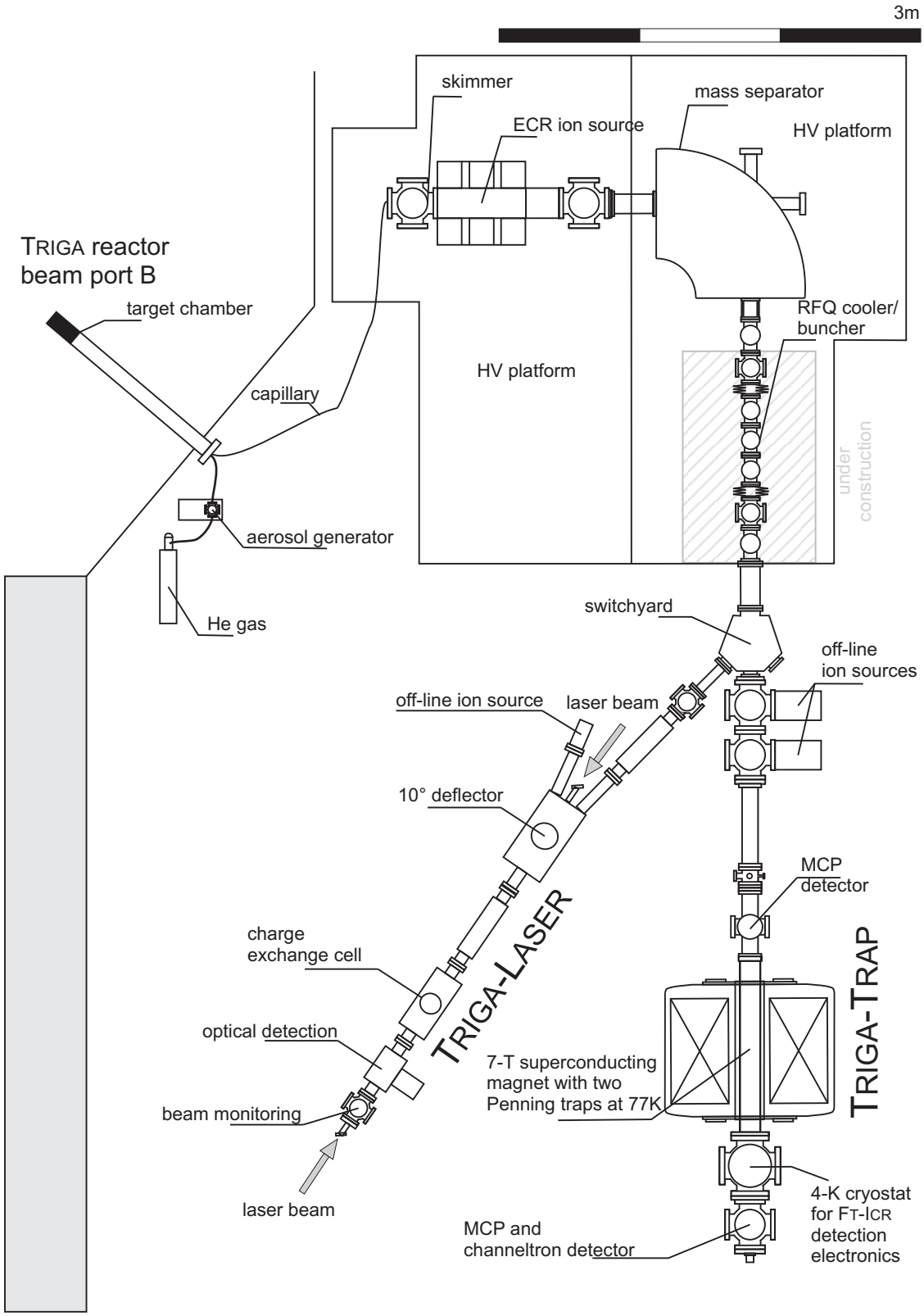

Figure 3.1: A schematic view of the TRIGA-SPEC project. A neutron flux of about 10^{11} neutrons/$\left(\mathrm{cm}^2\mathrm{s}\right)$ from the nuclear research reactor is used to induce fission on a ^{249}Cf target. The fission products attached to carbon aerosols are transported through a capillary into the ion source region. An electron cyclotron plasma source produces mostly singly ionized fission products. The mass separated ion beam can either be guided into the TRIGA-LASER collinear laser spectroscopy beamline or into the TRIGA-TRAP mass spectrometer. Taken from [Ket10].

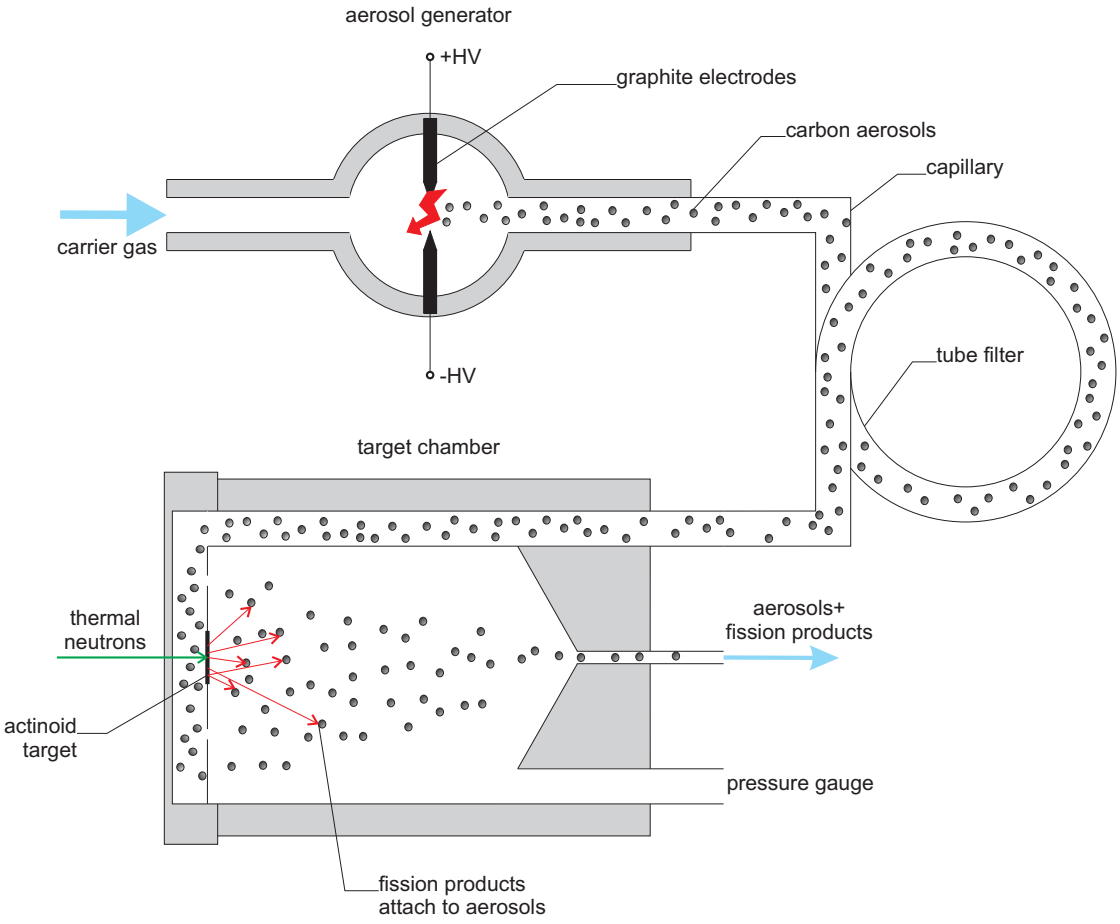

Figure 3.2: The gas jet system and the target chamber at the TRIGA reactor. The carrier gas streams into the aerosol generator, where a discharge burns between two graphite electrodes. The carrier gas flush the aerosols to the target chamber through a capillary. In the target region neutron induced fission products from an actinoid target thermalize due to a gas pressure of about 2 bars and attach to the aerosols. Taken from [Ket10].

To apply this technique a stopping cell, an ion guide and ion optics would have to be placed inside the biological shield of the reactor. Therefore, necessary maintenance would be difficult due to the activation of the materials and special care would have to be taken in order to fulfill safety issues.
At the TRIGA reactor a gas-jet technique [Mac69, Wol76, Tal87] is used instead to transport the fission fragments along several meters through a capillary to the ion source. Several carrier gases like argon and helium were tested to demonstrate an efficient transport of the fission products. High efficiency can only be maintained if diffusion to the walls of the capillary is avoided. The fission products are therefore attached to aerosol particles which are interspersed into the carrier gas. To produce, *e.g.*, carbon clusters, a discharge is

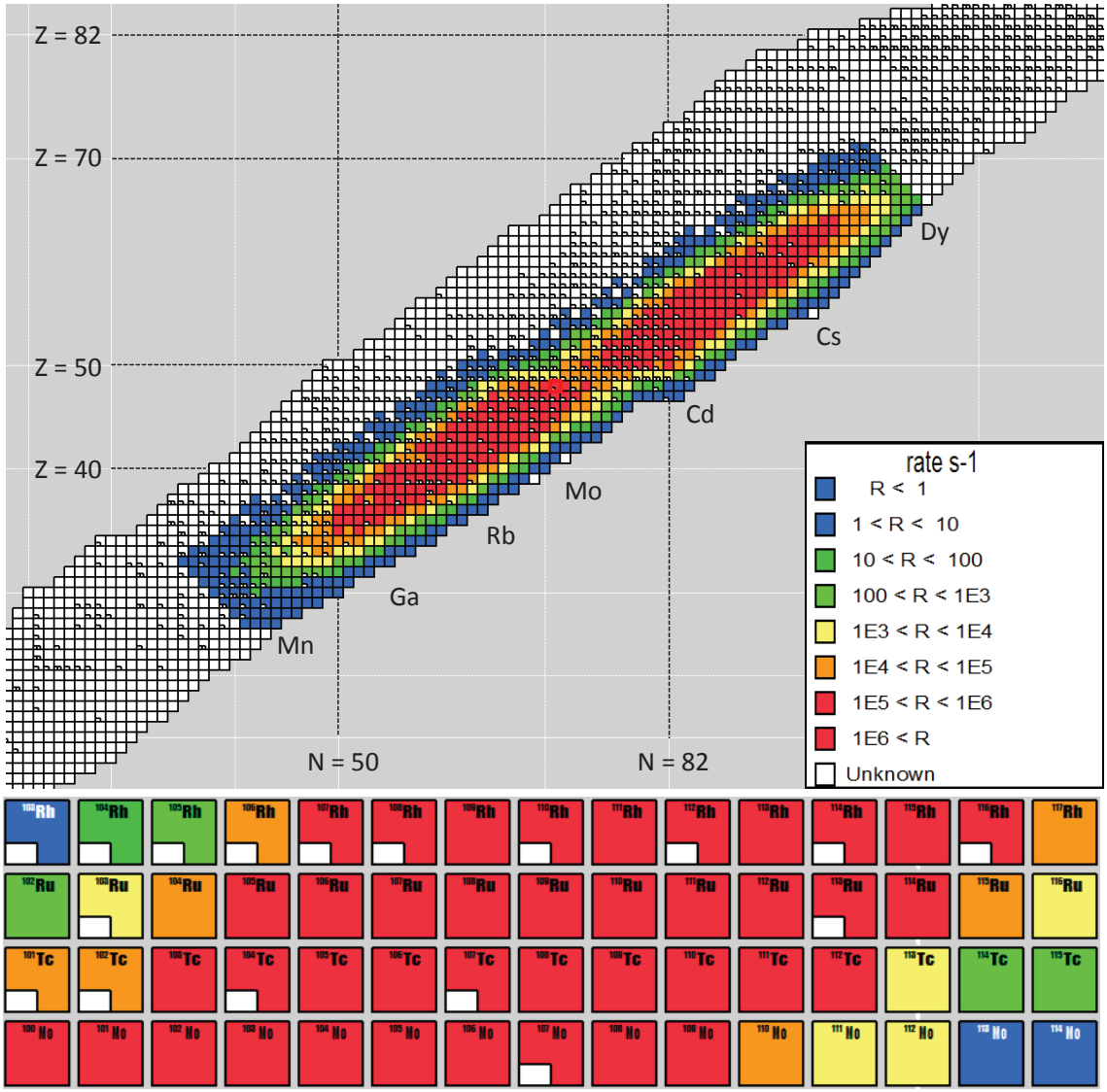

Figure 3.3: The production rate at the TRIGA reactor using a 300 μg ^{249}Cf target in the steady-state mode. The enlarged view below shows the production rate of the region of interest for collinear laser spectroscopy.

established between two graphite electrodes in the aerosol generator. The formed carbon aerosols are flushed with the carrier gas through a long capillary to the target chamber. A schematic view of the aerosol formation and the target chamber is depicted in Fig. 3.2. The target material (^{235}U, ^{249}Cf) is located inside the chamber. Fission is induced by the thermal neutrons inside the reactor and the fission products recoil from the target and are stopped in the carrier gas. Therefore a pressure of about 2 bars is maintained inside the chamber.

The expected production rate (yield) at the TRIGA reactor strongly depends on the

target material, its sample size and the neutron flux. In the steady-state mode the TRIGA Mainz is operated at a thermal power of 100 kW and a neutron flux of about 10^{11} neutrons/ $\left(\mathrm{cm}^2\mathrm{s}\right)$ is available at the target chamber position. Alternatively, the reactor can be operated in the pulsed mode, which delivers a neutron flux of about 10^{14} neutrons/ $\left(\mathrm{cm}^2\mathrm{s}\right)$ within a 20 ms window. Such a pulse can be triggered about 10 times per hour. The yield for the use of a 300 μg ^{249}Cf target in the steady-state mode is depicted in Fig. 3.3. A production rate around $10^6/s$ is estimated for neutron-rich nuclei above N = 50 and around N = 82. The yield quickly drops with increasing neutron number.
The radioactive ions and atoms attach to the aerosols and are flushed out of the target chamber to be transported to the ion source region through another capillary. Since the flow of the gas in the capillary is laminar and the mass of the aerosols which are typically as large as 100 nm in diameter is large, they are transported without wall collisions. A skimmer system with a conical aperture separates the fission products from the carrier gas which is pumped away using a 270 m^3/h roots pump. Due to their difference in mass the heavy transport clusters have a much smaller expansion angle in vacuum than the carrier gas. An overall efficiency up to 70% was demonstrated [Eib10] using carbon clusters as aerosols. Once the aerosols are separated from the carrier gas, the attached radioactive species have to be released in order to perform mass spectrometry or laser spectroscopy. This turned out to be the most difficult step for TRIGA-SPEC. Three different ion sources are currently investigated for this purpose: an ECR ion source, a surface ion source and a plasma ion source.

3.1.2 Ion Sources at TRIGA-SPEC

The setup of the electron cyclotron resonance **plasma ion source** (ECR) [Smo12] is shown in Fig. 3.4. A magnetron produces microwaves at 2.45 GHz which are coupled into a waveguide. A resultant standing-wave with its maximum at a horn antenna induces a secondary microwave at the same frequency which runs along a coil into the plasma region. The latter consists of 18 permanent magnets producing a magnet field of B = 87.5 mT for axial and radial confinement of the plasma. If the microwave frequency ν_M fulfills the electron cyclotron resonance condition $\nu_M = eB/2\pi m_e$ energy is fed into the electron cyclotron motion and a plasma is ignited. The fragments and aerosols entering the plasma of the ion source split up and the fragments are ionized. Since the microwave power is quite low (300 W) it is expected to get singly charged ions only. An extraction electrode extracts the ions from the plasma before acceleration up to 30 keV. Many attempts to efficiently ionize the fission products were made, but the ionization efficiency was below the detection limit which is attributed to a very short interaction time between the aerosols and the plasma [Smo11]. For that reason two additional ion sources are currently under development.
The second available source is a **surface ion source** [Ren12]. This is an improved design based on the high-temperature ion source applied at the HELIOS[2] setup in Mainz [Bru85].

[2] Helium-Jet on line isotope separator facility

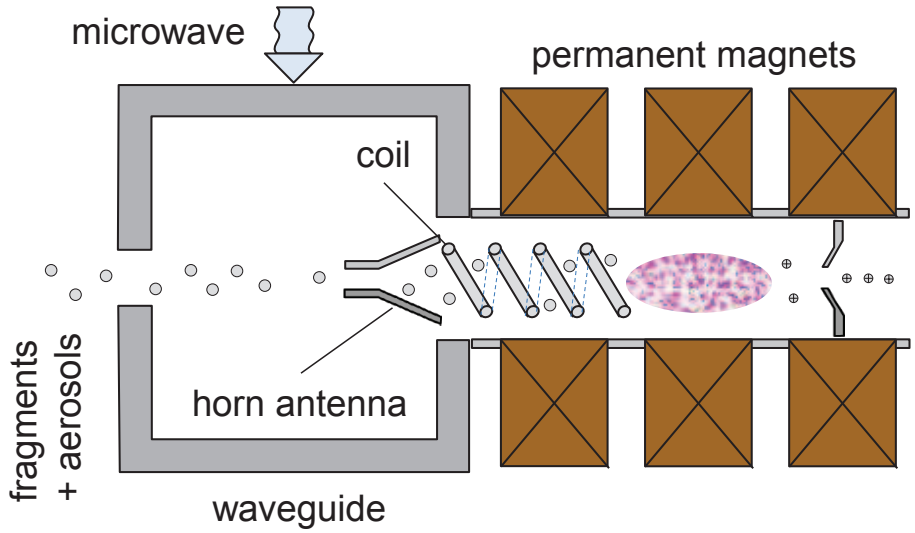

Figure 3.4: A schematic view of the ECR plasma ion source at the TRIGA reactor. Microwaves are fed into the plasma region using a horn antenna, which is coupled to a coil. The magnet field of 18 permanent magnets confine the plasma that splits the fission fragments from the aerosol clusters.

A layout is shown in Fig. 3.5. In this case the fission products are transported by the capillary into a brass tube and the carrier gas is separated from the aerosols with the skimmer. The carrier-gas cleaned aerosol beam passes a bornitrid insulator which keeps the skimmer in distance to the tantal-ionizer. The latter is heated via electron bombardment to temperatures up to 3500 K. Inside the ionization chamber the fission products are released from the aerosol particles and surface ionized provided that the ionization potential is sufficiently low. Another skimmer system is used to extract the ions up to 30 keV. A rather high ionization efficiency in the order of 80% is excepted for such a type of ion source. But only alkali, earth alkali and rare earth atoms can be ionized. Most of these nuclei have already been investigated in the past.
If the ionization potential exceeds 6 eV, the surface ion source can not be used. For that purpose another plasma ion source is currently under development [Nie12]. This is an improved version of the hollow-cathode plasma ion source developed by A. L. Mazumdar for the HELIOS system [Maz76]. The assembly is depicted in Fig. 3.6. A tantalum-anode and -cathode enclose an insulator made of bornitride. The cathode is heated to about 1800 K by electron bombardment. If the gas jet is adjusted to the skimmer (anode), the pressure inside the ion source increases. In order to ignite a plasma it is necessary to apply a voltage between anode and cathode in the order of about 1000 V. Once the plasma burns, the distance between gas jet capillary and anode can be increased again. In [Kar82] an overall efficiency of about 1% with this setup is reported. The main drawback of this ion source is a clogging of the ionized particles onto the apertures. After several hours of operation the diameter of the output aperatures decreases and the efficiency drops. In such a case the apparatus must be opened again to clean the aperature. However,

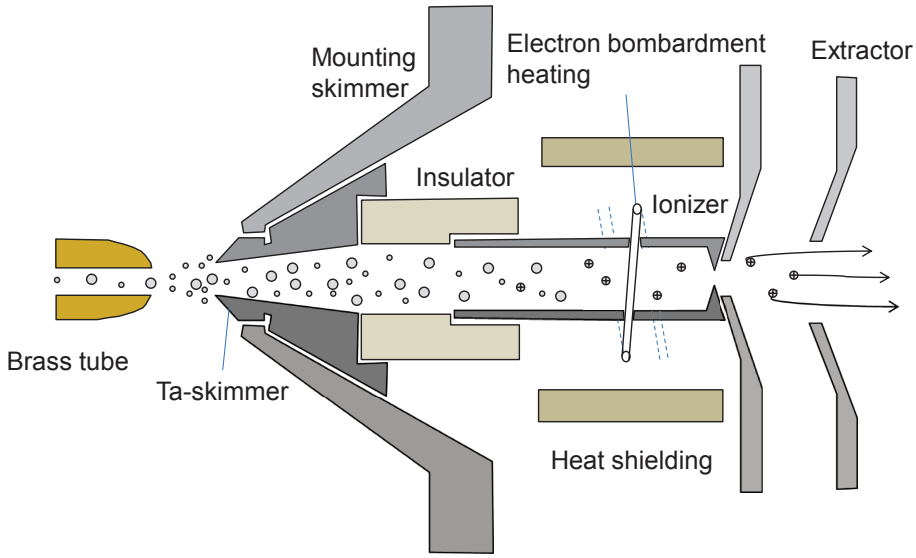

Figure 3.5: A schematic view of the surface ion source at the TRIGA reactor. A brass tube is used to separate the fission products from the carrier gas due to the expansion angle. The fission fragments are released from the aerosol particles inside the ionizer chamber which is heated by an electron bombardment up to 3500 K. Ions produced by surface ionization are extracted using the extractor and accelerated to about 30 kV.

further investigations and developments on this setup might avoid this problem. Then, the produced ions are further guided to the TRIGA-TRAP or TRIGA-LASER branch. Unfortunately, a radioactive ion beam was not prepared for laser spectroscopy at TRIGA-SPEC until the thesis was finished. However, first mass separated radioactive species were reported [Ren12]. Thus, the spectroscopic measurements during this work were performed using the off-line surface ion source directly installed at the TRIGA-LASER branch and are further explained in Chapter 4.

3.2 ISOLDE Facility at CERN

At the on-line separator ISOLDE at CERN [Kug00] depicted in Fig. 3.7 isotopes of many elements from helium up to radon (Z = 88), except cases like boron or silicon and all refractory metals, *e.g.* of the platinum group, are accessible, even if the lifetime is somewhere in the millisecond range. These (radioactive) isotopes are produced by nuclear reactions (spallation, fission and fragmentation) induced by a 1.4 GeV proton beam impinging on a target. In contrast to the production mechanism at the nuclear research reactor TRIGA refractory elements are prohibited at most ISOL facilities.
Here, the beryllium isotopic chain $^{9-12}$Be was investigated at ISOLDE. These isotopes were produced by nuclear fragmentation of a thick and hot uranium carbide (UC_x) target using the 1.4 GeV pulsed proton beam with a period of 1.2 s and an intensity about 10^{13}

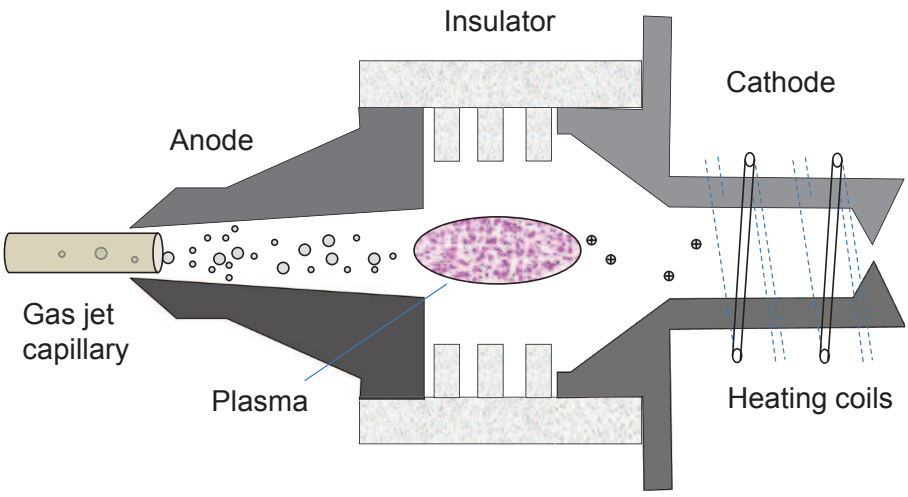

Figure 3.6: A profile of the plasma ion source at the TRIGA reactor. The anode and cathode are made from tantalum which enclose a bornitridinsulator. The cathode is heated to about 1800 K by electron bombardment which abets the ignition of the plasma.

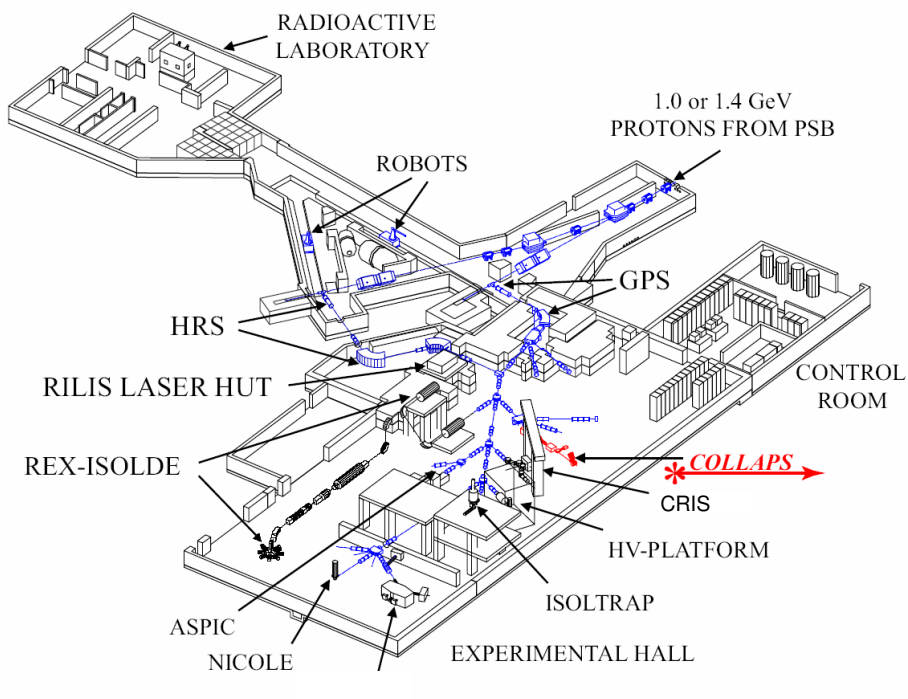

Figure 3.7: The ISOLDE facility at CERN . A high-energy proton beam of up to 1.4 GeV impinges on a thick target. The products are ionized and guided into a mass separator magnet. Finally the ion beam is deflected into the beamline. This experiment took place at the COLLAPS beamline.

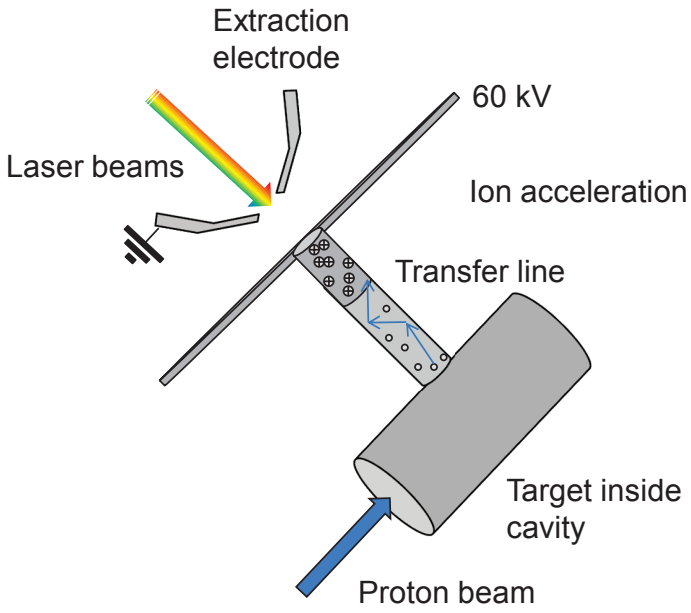

Figure 3.8: The RILIS ion source at ISOLDE. A pulsed proton beam impinges on a hot target heated up to 2300 degrees. The atoms effuse through a heated tungsten pipe and are resonantly ionized by (mostly 2-3) counter-propagating laser beams. A high potential up to 60 kV is used to extract the ions.

protons/pulse. The reaction products diffuse out of the target into an ion source. At the ISOLDE facility three different types of ion sources are in use: a surface ion source, a plasma ion source and the resonance ionization laser ion source (RILIS). Since the ionization potential of Be (9 eV) is too high for efficient surface ionization, the Z-selective RILIS was used as discussed in Chapter 5.
As shown in Fig. 3.8 for the resonant laser ionization the nuclear reaction products diffuse from the cavity target into an (tungsten) ionization line that is heated up to 2300°C applying currents up to 800 A. At the end of the ionization line they are resonantly ionized by pulsed laser beams. In case of beryllium a two-stage resonant ionization was used.
The beryllium production rates according the ISOLDE yield table are listed in Tab. 3.1. It reflects the typical yield decrease along an isotopic chain towards the neutron dripline. The reduction by three orders of magnitude between the yields of ^{11,12}Be and ^{12,14}Be can partially be accounted to the smaller production cross section and partially to the reduced lifetimes.
The ISOLDE ion source is located on a high-voltage platform[4] and after the ionization process the electrostatic field between the ion source and the beamline at ground potential accelerate the ions up to 60 keV. For a subsequent mass separation they are either guided into the General Purpose Separator (GPS) with a mass resolution of $m/\delta m \approx 2400$ or into the High Resolution Separator (HRS) with $m/\delta m \approx 10000$. The mass separated ion

[4]Details of the high voltage platform are discussed in Chapter 6.

Table 3.1: Nuclear properties of the beryllium isotopes and yield table at the ISOLDE facility at CERN. Listed are the nuclear mass M, half-life ($T_{1/2}$), nuclear spin I , magnetic dipole moment (μ_I) and the beryllium yields measured at ISOLDE using the PS Booster with a 1.4 GeV proton beam and RILIS for ionization[3].

	M [u]	$T_{1/2}$	I	$\mu_I[\mu_N]$	(ions/μC)
^{7}Be	7.01692983(11)[Aud97]	53 d	3/2	-1.39928(2) [Oka08]	$1.4 \cdot 10^{10}$
^{9}Be	9.01218300(10)[Rin09]	stable	3/2	-1.177432(3)[Win83]	
^{10}Be	10.01353474(13)[Rin09]	1.6×10^{6} a	0	-	$6.0 \cdot 10^{9}$
^{11}Be	11.02166155(62)[Rin09]	13.8 s	1/2	-1.6813(5) [Noe09]	$7.0 \cdot 10^{6}$
^{12}Be	12.0269223(23) [Ett10]	23.8 ms	0	-	$1.5 \cdot 10^{3}$
^{14}Be	14.042890(140) [Aud97]	4.35 ms	0	-	$4.0 \cdot 10^{0}$

beam is electrostatically guided into that beamline where the experiment takes place. In this case collinear spectroscopy of beryllium ions was performed at the laser spectroscopic apparatus COLLAPS.

3.3 Collinear Laser Spectroscopy

The linewidth of an optical spectrum is afflicted by various (in)homogeneous line broadening effects, of which the Doppler broadening usually dominates. It arises from the Maxwell-Boltzmann distribution of the atomic velocity. The frequency of the laser light in the rest frame of the atom moving with the velocity $\beta = v/c$ is Doppler shifted to

$$\nu' = \nu_0 \gamma \left(1 + \beta \cos\theta\right), \tag{3.1}$$

where ν_0 denotes the transition rest frame frequency and γ is the relativistic factor of time dilatation. For atoms at thermal velocities, *e.g.* in a gas cell, the γ factor can be approximated by $\gamma \approx 1$

$$\nu' = \nu_0 \left(1 + \beta \cos\theta\right), \tag{3.2}$$

The number of atoms $\mathrm{d}n(v_z)$ with the velocity v_z in direction of the laser beam is given by the Maxwell-Boltzmann distribution (in the thermal equilibrium)

$$\mathrm{d}n(v_z) = \frac{N}{\langle v \rangle \sqrt{\pi}} \exp\left\{ -\left(\frac{v_z}{\langle v \rangle} \right)^2 \right\} dv_z, \tag{3.3}$$

with $\langle v \rangle = \sqrt{2kT/m}$ being the most probable velocity. If $\mathrm{d}n(v_z)$ is transformed to the corresponding frequency space, one obtains

$$\mathrm{d}n(\omega) = \frac{Nc}{\langle v \rangle \, \omega_0 \sqrt{\pi}} \exp - \left(\frac{c \left(\omega - \omega_0 \right)^2}{\langle v \rangle \cdot \omega_0} \right) d\omega. \tag{3.4}$$

From Eq. 3.4 it is obvious that the Doppler effect causes an (inhomogeneous) linewidth broadening which is described by a Gaussian function with a FWHM $\delta\nu_D$ of

$$\delta\nu_D = \frac{\nu_0}{c} \sqrt{\frac{8kT \cdot \ln 2}{m}}. \tag{3.5}$$

This effect causes a huge broadening (compared to the natural linewidth) of the order of several GHz for temperatures of 2000 K and wavelengths around 300 nm. To perform precision spectroscopy, one has to reduce the Doppler broadening drastically. This can be performed by collimating the atom beam and exciting the atoms under 90°. Also laser cooling is a powerful approach. However, the first one often suffers from a dramatic loss in sensitivity, whereas the second approach requires a dedicated cooling scheme that is only available for a small number of species. The technique of collinear laser spectroscopy offers a more general way to reduce this massive broadening of the optical spectra.
Kaufman [Kau76] and Wing [Win76] independently pointed out that the Doppler width of a resonance spectrum is strongly reduced if a fast atom or ion beam is superimposed with a narrow bandwidth laser beam. Consider an ion source operated at a temperature T emitting ions with a velocity characterized by a Maxwell Boltzmann distribution (Eq. 3.3). Collinear laser spectroscopy is based on the fact that the energy spread δE of an ion beam remains constant under electrostatic acceleration. Using the relation [Kau76]

$$\delta E \; = \; mv\delta v \tag{3.6}$$

it is obvious that the increase in the velocity v during acceleration to a velocity $v = \sqrt{\frac{2eU}{m}}$ must be accompanied by a reduction of δv. The latter is responsible for the Doppler broadening $\delta\nu_D$ by the transition with frequency ν_0 to $\delta\nu_D = \nu_0 \; \delta v/c$. The resulting Doppler width of the probed transition after acceleration is thus

$$\delta\nu_D = \frac{\nu_0 \cdot \delta E}{\sqrt{2eUmc^2}}. \tag{3.7}$$

Therefore, a reduction factor R of the velocity spread and thus of the Doppler broadening can be determined. Consider two ions $\left(v_1 = 0 \text{ and } v_2 = \sqrt{\frac{2kT}{m}} \right)$ being accelerated in an electrostatic potential U to their final velocities

$$v_1' = v_a = \sqrt{\frac{2eU}{m}}, \quad v_2' = \sqrt{v^2 + v_a^2} \approx v_a + v_2^2/(2v_a). \tag{3.8}$$

Therefore the difference in their velocity Δv after acceleration is

$$\Delta v = v_2' - v_1' = v_2 \cdot \underbrace{\frac{1}{2}\sqrt{\frac{kT}{eU}}}_{R}. \tag{3.9}$$

which is a reduction of the initial width by the factor R. It should be noted that this calculation is neglecting **all** broadening mechanisms of the probed absorption line including the natural linewidth. From Eq. 3.9 it is clear that the higher the acceleration voltage U the smaller is the resulting linewidth. A typically applied acceleration voltage is $U = 60$ kV. The Doppler broadening of the $2S_{1/2} \rightarrow 2P_{1/2}$ transition in ^{12}Be ions ($\nu_0 = 957.4$ THz) is according to Eq. 3.5 roughly 9 GHz at a realistic source temperature of 2200 K. Applying collinear laser spectroscopy reduces this linewidth to $\delta\nu_{D,60\text{ kV}} = \delta\nu_{D,0} \cdot R \approx 8$ MHz. The $2p_{1/2}$ state in beryllium has a life time of $\tau_{\text{nat}} \approx 8.(4)$ ns [And69] and therefore a natural linewidth of about 20 MHz. The expected linewidth is thus comparable to the natural linewidth. Typical values for the observed linewidth are about 50 MHz. This additional line broadening is due to the fact that the width of the energy spread δE is not only determined by the thermal distribution, but inhomogeneous fields inside the ion source can cause different start potentials of the ions. If a plasma ion source is used the linewidth will increase to several hundred MHz. However, other broadening mechanism must be considered, too. Besides the Doppler broadening, other (in)homogeneous line broadening effects might occur, such as *e.g.* saturation broadening, transient time broadening or AC Stark broadening. For this work, saturation broadening is also relevant: With increasing laser intensity, the rate of stimulated emission out of the excited state becomes larger, effectively shortening the lifetime of the upper state and therefore increasing the linewidth (saturation broadening). This effect should be investigated beforehand in order to find the optimum laser power.

Collinear laser spectroscopy is ideally suited to investigate optical transitions in short-lived ions or atoms in order to determine nuclear ground state properties, *i.e.* charge radii, spins and nuclear moments [Kau76, Ant78, Neu85].

However, it was also applied for tests of QED on helium-like species from Li^+ up to F^{7+} [Rii94, Sch93, Din91], ultra-trace isotope detection [Zim94, Wen99] and high precision voltage measurements [Pou82, Pou88, Goe04, Kri11].

The setup for collinear laser spectroscopy at COLLAPS is schematically shown in Fig. 3.9: A 60 keV mass separated ion beam enters the apparatus passing an electrostatic deflector pair and several quadrupole lenses guiding a shaped ion beam through the center of the beamline. The ion beam is then superimposed with a collimated laser beam. In contrast to other spectroscopic methods where the laser frequency is scanned across the optical resonance, it is common in the collinear technique to keep the laser frequency constant. The resonance is recorded using the so-called Doppler-tuning, *i.e.*, modifying the ion's velocity by applying an additional voltage ($U_{\text{Det}} = \pm 10$ kV) to the detection region. For anti-parallel propagation of laser and ion beam the laser frequency ν_L in the laboratory

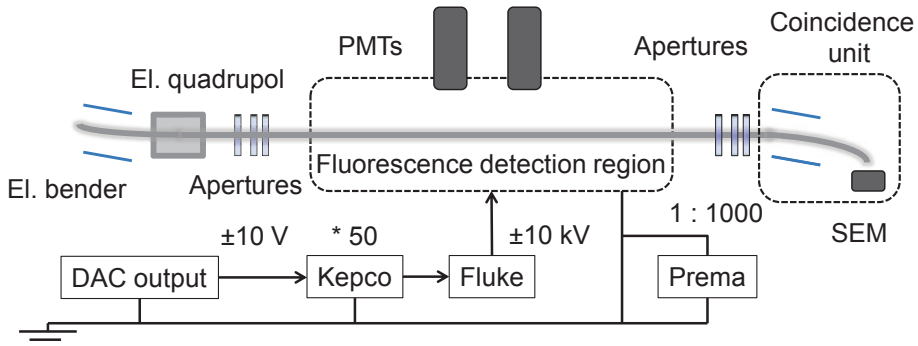

Figure 3.9: Setup for collinear laser spectroscopy at COLLAPS with applied voltages. For details see text.

frame is shifted in the rest frame of the ion according to

$$\nu = \nu_L \frac{1+\beta}{\sqrt{1-\beta^2}} \tag{3.10}$$

with

$$\beta = \frac{v}{c} = \sqrt{1 - \frac{m^2c^4}{(eU + mc^2)^2}}. \tag{3.11}$$

Hence, the additional voltage U_{Det} is varied in such a way that the Doppler-shifted laser frequency is shifted across the resonance frequency in the ion's rest frame. In order to avoid optical pumping into dark states it is required that the ion comes into resonance with the laser only in the fluorescence detection region (FDR). Therefore, the additional tuning voltage is applied to the FDR and the (first) photomultiplier mounted as close to the front end of the chamber as possible. However, it might be necessary for practical reasons (*e.g.* transition wavelength) to investigate neutral atoms. In this case charge exchange reactions - commonly with alkali vapor - can be used to neutralize the ions in flight. Such a charge exchange cell (CEC) is then placed immediately in front of the optical detection region. Then the Doppler-tuning voltage must be applied to the CEC and the distance between CEC and FDR should be as short as possible.
For most isotope shift measurements of short-lived nuclei, it is sufficient to keep the laser frequency constant and knowledge of the absolute frequency is only required to wavemeter precision (about 0.001 nm). However, for very light isotopes, high-voltage measurements and test of fundamental interactions and symmetries the absolute frequency must be determined with high accuracy as will be discussed below.
A large variety of detection techniques has been used in collinear laser spectroscopy over the last decades to observe the resonant interaction between the specific element and the laser photons. Among those are resonance ionization, $\beta-$asymmetry detection after optical pumping and state-selective ionization or charge exchange. However, the first and most general approach is optical fluorescence detection, since it is in principle suitable for every atomic species. But its efficiency is strongly dependent on the attributes of the atomic

spectrum and several approaches have been developed. Some of them will be discussed in the next section.

3.3.1 Optical Detection Limits in Collinear Laser Spectroscopy

An optical detection region should be optimized for collecting as many emitted fluorescence photons as possible but also to suppress scattered laser photons in order to improve the signal-to-noise (S/N) ratio. Usually, imaging optics are used to detect the collected fluorescence photons by a pair of photomultiplier tubes. However, this approach generally suffers from the relatively small solid angle that can be covered. A new approach is currently under development at TRIGA-LASER, where non-imaging optics is applied to collect the photons [Ham10].
In the classical fluorescence detection approach, collinear spectroscopy is suitable for stable and short lived radioactive isotopes. Many isotopes were investigated applying this technique world-wide. However, the main drawback is the low detection efficiency which makes this configuration not feasible for isotopes with low production rates ($< 5\ 000$ ions/s) in a reasonable time. The photomultiplier detects a background rate due to the scattered incoming laser light (major source), the ion beam and due to their own dark count rate. In order to achieve evaluable data of the hyperfine structure a signal to noise ratio (S/N) of at least 3 is recommended. Depending on the total detection efficiency ϵ_{tot} and measurement time t the minimum ion beam rate can be estimated. For a typical total detection efficiency $\epsilon_{\text{tot}} \approx 1 : 25\ 000$ an ion beam rate of $10^5 - 10^6$ ions/s is necessary to achieve a resonance after one hour with a background rate $b = 1\ 500/\text{mW}$. For that reason several methods were investigated in order to improve the sensitivity which is limited by the signal *and* the background, to expand collinear measurements to isotopes with lower yields. Two of these methods were tested for the beryllium spectroscopy and are shortly described in the following subsections.

Ion-Photon Coincidence Detection

In 1986 Eastham *et al.* [Eas86] presented a detection method to eliminate events from laser stray light. Therefore the optical detection is combined with a coincidence unit as shown in Fig. 3.10. The signal of the single-ion detector at the end of the beam line is used to create a coincidence gate for the photomultiplier signal. The latter must be delayed by the ion's time of flight from the optical detection region to the particle detector. Then, only those photons are accepted for the spectrum which are in delayed coincidence with a corresponding ion, all others are discriminated. The count rate for randomly gated coincidences D_R is the product of the ion beam intensity I, the background rate B and the transient time t through the detection region: $D_R = I \cdot B \cdot t$. Typically, the rate for random coincidences is rather low *e.g.* $D_R \approx 1\ 500\ [1/s] \cdot 300\ [1/s] \cdot 10^{-7}[s] = 0.05\ [1/s]$. An isobaric contamination of the ion beam increases the background rate considerably since the coincidence gate is triggered by mistake. Hence, this technique can only be used

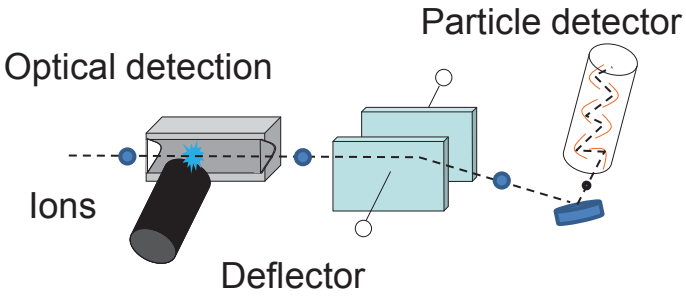

Figure 3.10: A coincidence detection unit. The ions are in resonance with the collinear propagating laser beam when passing the optical detection unit. The fluorescence photons are collected with a photomultiplier and a signal is sent to a coincidence unit. The corresponding ion is guided onto a metal plate when passing a deflector pair. The emitted electron is detected by a particle detector, such as MCP, and another signal is fed into the coincidence unit. Both signals can only be compared if the ion's time of flight is taken into account.

if there is none or only weak isobaric contamination.

This technique was further developed by Eastham [Eas91] using a position sensitive optical detection for the photons in order to resize the coincidence gate down to 20 ns. Moore *et al.* [Moo02] demonstrated collinear spectroscopy of a very short-lived barium isomer with an ion beam rate below 100 atoms/s.
An ion-photon coincidence detection unit was built during the diploma thesis of B. Sieber [Sie10] in Mainz. Its application and measurements on ^{40}Ca ions are presented in Chapter 4.3.

Bunching and Cooling of Ions Beams

A very efficient method to suppress background events from laser stray light was developed in Jyväskylä applying bunched ion beams [Nie00]. Therefore, a longitudinally segmented and gas-filled radio-frequency quadrupole [Her03] is used. The principle is shown in Fig. 3.11. The complete RFQ is located on a high-voltage platform and its potential is similar to the ion source potential. At the last segment the highest voltage is applied which serves as a potential well during accumulation. The ions injected into the RFQ loose energy in collisions with the buffer gas and are cooled to the buffer-gas temperature. After a few ms, they are confined inside the longitudinally potential minimum and can be extracted by switching the end electrode down as indicated in the lower part of Fig. 3.11. This results in the extraction of short and dense pulses with typical bunch widths of the order of $\tau \approx 1 - 5\ \mu s$ [Lun09, Her03]. Typical accumulation times t_{acc} are in the order of 10 to 100 ms. The horizontal and vertical emittances are well reduced and the energy spread is typically below 1 eV at 50 keV. Now, the detection of the resonantly scattered photons by the photomultiplier can be gated to the time that the bunch needs

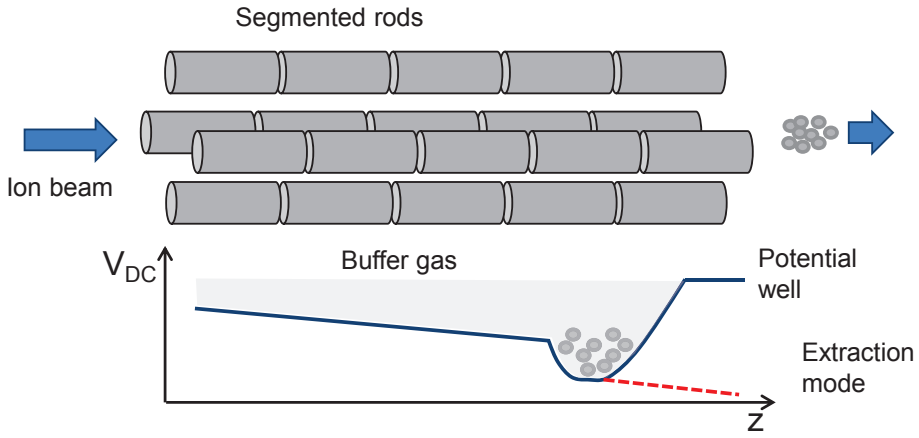

Figure 3.11: Principles of a radio-frequency quadrupole cooler and buncher. The ions enter a puffergas filled radio-frequency quadrupole (Paul trap), where an alternating rf-voltage is fed to each of the two opposite segmented rods. The ions are accumulated in the minimum of the axial DC-potential and loose their energy (of up to 60 keV) due to the interaction with a buffer gas to less than 100 eV. An extraction DC-potential applied to confine the ions is switched to ground to release a bunch of ions.

to pass the optical detection unit. As a rule of thumb, the background is suppressed by a factor of $k = \frac{t_{acc}}{\tau} \approx 10^4$. The use of the buncher is usually limited by space charge effects to less than $10^5 - 10^6$ ions in the trap. Since the trap is not able to distinguish between isobars the buncher will give rise to losses if the beam is highly isobaricly contaminated. However, during the last decade ion beam coolers and bunchers are widely adapted in collinear laser spectroscopy setups, like at Jyväskylä [Cam02, Nie00], ISCOOL [Pod04, Man09] or TITAN [Smi07, Lev10, Man11]. Also in the TRIGA-SPEC project the COLETTE RFQ, a donation from the MISTRAL experiment [Lun09], is now installed and under commissioning.

3.3.2 Combining Collinear and Anticollinear Spectroscopy

According to Section 2.4.1, isotope shift measurements are performed to determine the nuclear charge radii referring to a known charge radius of the reference isotope. Collinear laser spectroscopy has been applied to investigate medium and heavy nuclei, but rarely to the light species [Ott89].
In the original concept of collinear laser spectroscopy the resonance spectra are recorded by changing the ion's kinetic energy and therefore the velocity according to the Doppler formula. Taking the differential Doppler factor into account, one can convert the energy scale into a frequency scale. At this point it is obvious that the applied acceleration voltage has to be determined with high accuracy, *at least* to 10^{-5} for the very light species, in order to extract the transition frequency with an accuracy of about 1 MHz. It can be easily calculated that an undiscovered drift of the acceleration voltage from 60 kV to 59.995 kV

causes an artificial isotope shift of about 18 MHz between the neighboring isotopes ^{10}Be and ^{11}Be, which is huge compared to the required accuracy.
Usually, the applied high voltage for the acceleration of the ions at ISOLDE is specified to a relative accuracy of 10^{-4}, *e.g.* 60.000(6) kV. Even if an accuracy of 10^{-6} could be reached, the applied high voltage is not necessarily the beam energy, since the potential inside the directly heated ionization tube must be taken into account. Therefore it is obvious that it is not possible to perform optical isotope shifts of $Z \leq 10$ nuclei with sufficient accuracy.
Combined collinear and anticollinear spectroscopy on light helium-like ions were already performed by Riis *et al.* on Li^+ [Rii94], whereas Scholl *et al.* investigated Be^{2+} [Sch93] and Dineen *et al.* B^{3+} [Din91] in alternating parallel and anti-parallel geometry.
In 1982 Poulsen [Pou82] even suggested an approach to measure high voltages up to 100 kV with a relative accuracy of 10^{-6} relating the ion's velocity in collinear laser spectroscopy directly to frequency standards. This approach was tested at Mainz university for measuring the high voltage applied to the electron cooler at the ESR with highest accuracy [Kna00, Goe04]. In the framework of the LUST-experiment high voltages up to 50 kV were measured with accuracies up to 10^{-4} probing the velocity of calcium ions. At this point the limiting factor was the fact that a metastable state was used, which was not only populated in the ion source but also in the ion-atom collisions along the beamline and the self-made wavemeter which was used to determine the wavelength of the lasers with a relative stability of about 10^{-8}. Nowadays, optical frequencies can be measured with a femtosecond frequency comb with an accuracy better than 10^{-14} [Ude02].
Poulsen suggested combining collinear and anticollinear spectroscopy to perform voltage-independent measurements. The Doppler-shifted frequency $\nu_{c,ac}$ seen by the moving ions is related to the transition frequency ν_0 according to

$$\nu_c = \nu_0 \gamma (1 + \beta) \tag{3.12}$$

$$\nu_{ac} = \nu_0 \gamma (1 - \beta) . \tag{3.13}$$

If both frequencies $\nu_{c,ac}$ are measured at exactly the same ion velocity the formula

$$\nu_0 = \sqrt{\nu_{ac} \cdot \nu_c} \tag{3.14}$$

is valid.
The lightest element investigated by collinear laser spectroscopy before beryllium was neon[5] (Z=10) [Gei00]. The acceleration voltage at that time was calibrated using a peculiarity of the neon atomic spectrum. Therefore, only one laser was required, which was back-reflected at the end of the beamline.

[5] Please not that this is only true for isotope shift determination. At COLLAPS the nuclear moments of ^{9,11}Li and ^{11}Be have been determined earlier [Neu08, Gei99].

4 Laser Developments for TRIGA-LASER

This Chapter outlines the developments of the laser systems at TRIGA-LASER from its very first test towards the finalized setup for radioactive on-line spectroscopy. Since the spectroscopy of each isotopic chain requires another wavelength, several laser systems, starting from a simple diode laser up to a frequency comb stabilized Titan-Sapphire laser system have been installed and used for various spectroscopic investigations.

4.1 TRIGA-LASER Branch

As described in Chapter 2 ions of radioactive species are produced at TRIGA-SPEC either in an ECR or a surface ion source. After mass separation, accumulation and bunching the ions enter the ion beam switchyard, which deflects the ions into the TRIGA-LASER branch [Kra10]. An overview of the beamline is depicted in Fig. 4.1. Two pairs of quadrupole doublets in the connecting beamline are used to collimate the ion beam through the beamline. The first 10° electrostatic deflector is used to superimpose the ion beam with the laser beam. The deflector has a second port where an off-line ion source is installed. This source was used to commission TRIGA-LASER [Kra10]. An X-Y deflector pair allows to control the ion beam direction. To achieve a good overlap between the ion and the laser beam two adjustable apertures are added in front of the charge exchange cell (CEC) and behind the fluorescence detection region (FDR). If spectroscopy is performed on neutral atoms, the charge exchange cell is heated to typically 160°C. The FDR is located immediately behind the CEC. The shape and intensity of the ion beam can be investigated using the beam diagnostics unit. If required, a coincidence detection chamber is added [Sie10]. The laser beams in collinear and/or anticollinear geometry are coupled into the beamline via viewports that are mounted under Brewster-angle.

The off-line ion source consists of a resistively heated graphite tube which can surface ionize alkaline elements, earth-alkalines and some lanthanides. Extraction optics are used to form and shape the ions to a nearly collimated ion beam. The ion source is installed on a high voltage platform that can be raised to about 20 kV against the beam line at ground potential.

Depending on whether ions or atoms are investigated, the Doppler-tuning voltage is applied either to the FDR or to the CEC. The scanning voltage is generated by amplifying the output of a 10 V 16-bit DAC card with a Kepco BOP500 voltage amplifier (amplification factor 50). Hence, a scanning voltage of ± 500 V is available. This voltage range is not sufficient to cover the range required to scan from one isotope to the next. Therefore a Heinzinger PNChp10000 high voltage power supply is used to add up to ±10 kV to the

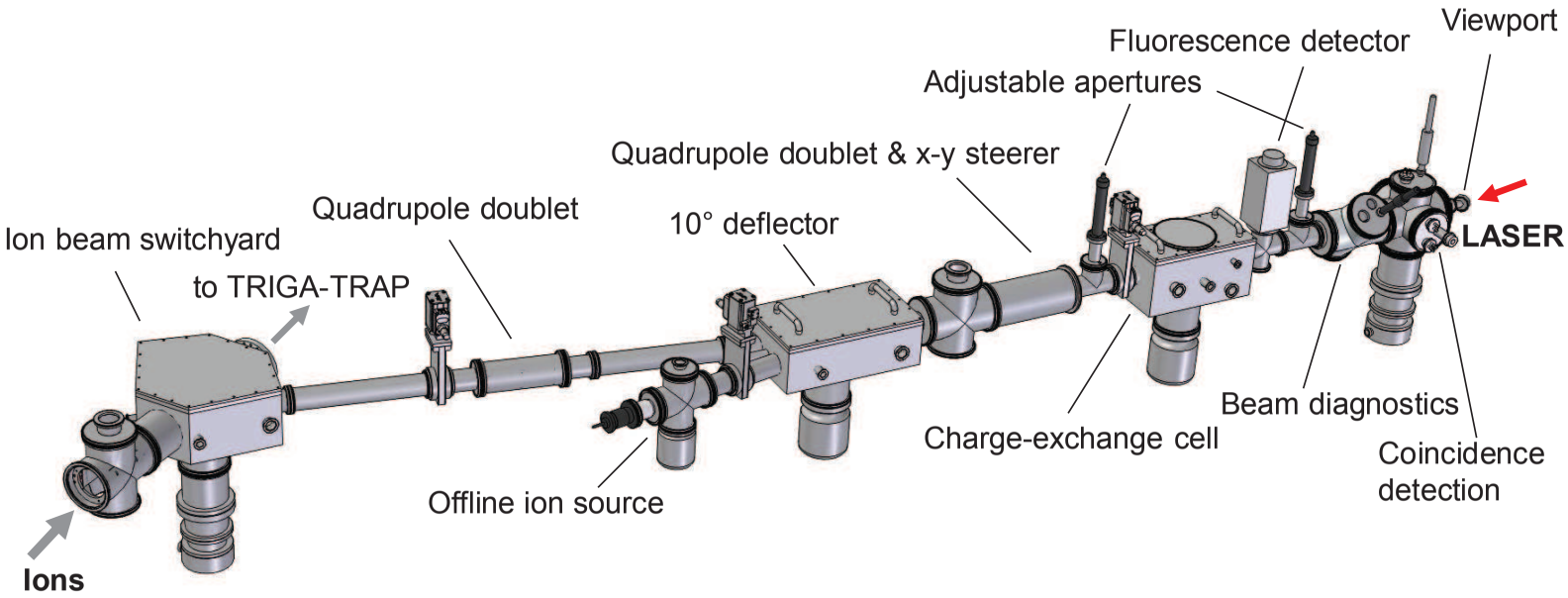

Figure 4.1: Layout of the TRIGA-LASER beamline [Kra10]. The 30 keV ion beam from the on-line ion source is deflected into the TRIGA-LASER branch in a switchyard. Two quadupole doublets along the beamline are used to collimate the ion beam. A 10° electrostatic deflector of the TRIGA-LASER branch is used to superimpose ion- and laser beam. A pair of quadrupole doublets and an X-Y steerer pair allows for ion beam tuning and shaping. Viewports at both ends of the beamline are installed under the Brewster-angle to avoid additional stray light from the laser beams. The resonance fluorescence is detected by a photomultiplier-tube. The charge-exchange cell for beam neutralization is followed by the FDR and a beam diagnostics section. A coincidence unit can additionally be adapted to the beamline.

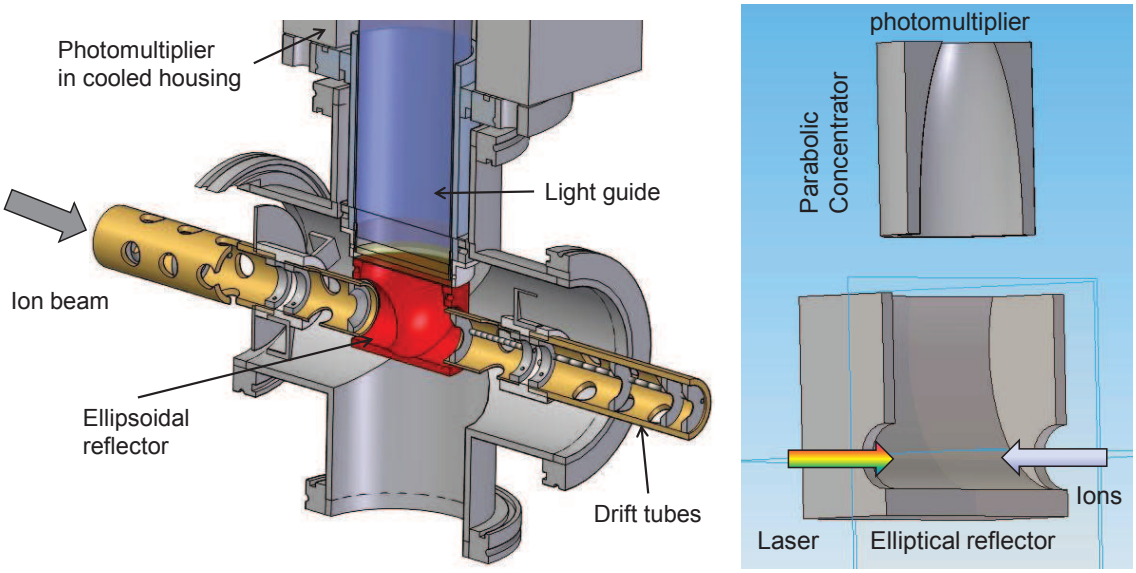

Figure 4.2: The two optical detection regions used at TRIGA-LASER during this thesis. In the first FDR [Kra10] (left) the ions or atoms pass four segmented drift tubes. The outer two are at ground potential and the inner two are connected to the mirror chamber and thus are on the scanning potential. The mirror chamber consists of an ellipsoidal copper mirror (red) which reflects the fluorescence photons to a light guide (blue) that transports the photons to a photomultiplier tube. The schematics of the second advanced optical detection unit [Ham10] (right) shows the reflector with an elliptical cross section that is translated along the ion beam path and focuses the light on a line in the focal plane. Straylight is suppresses by movable apertures and a conceptional parabolic concentrator, an element of non-imaging optics. The latter was optimized for an efficient detection of fluorescence photons in the UV region.

Doppler-tuning voltage. The Heinzinger device is mounted on a floatable platform and its ground potential is varied by the scanning voltage from the Kepco device. The total energy of the ions inside the FDR or the CEC, respectively, is therefore given by the sum

$$U_{\mathrm{tot}} = U_{\mathrm{acc}} \pm U_{\mathrm{post}} \pm U_{\mathrm{scan}} \tag{4.1}$$

of the ion source voltage U_{acc}, the Heinzinger post-acceleration voltage U_{post} and the scan voltage from the Kepco amplifier U_{scan}, which corresponds to voltages between $10 - 30$ kV for off-line and $20 - 40$ kV for on-line operation with the scan voltage of $U_{\mathrm{scan}} = \pm 500$ V. The high voltage is scaled down using a voltage divider (Julie Research KV-10R) with a relative accuracy of 10^{-4} and read out with an Agilent 34401A multimeter.
For the very first tests in 2009 the FDR consisted of an ellipsoidal reflector made of copper to reflect the fluorescence photons to a light guide that is connected to a photomultiplier tube (Hamamatsu R1017). This photomultiplier tube was chosen for the infrared-region

and has a quantum efficiency of about 5% at 800 nm. A detailed view of the fluorescence detection region is given in Fig. 4.2 (left) [Kra10]. The ions pass four segmented drift tubes before entering the reflector (red). For ion spectroscopy, the Doppler-tuning voltage is applied to the two inner drift tubes and the copper reflector to prevent interaction of the laser beam with the ions already outside the optical detection region (dark pumping). Fluorescence photons are reflected from the copper mirror to a light guide (blue) that transports the photons to a photomultiplier tube.
This copper reflector was constructed to investigate transitions in the near infrared (700-900 nm), but due to the insufficient reflectivity of copper at lower wavelengths it is not feasible for UV light without coating. It was constructed with the philosophy to collect as many fluorescence photons as possible and image them to the photomultiplier tube. Besides a very good optical efficiency, it also collects undesired scattered light very efficiently. Therefore, a new optical detection region, as depicted in Fig. 4.2 [Ham10], partially based on the principles of non-imaging optics, was commissioned. Based on optical simulations, an elliptical reflector geometry inside the vacuum chamber was combined with an aperture in the focal plane of the reflector and a so-called compound parabolic concentrator that bundles the light to the aperture of the photomultiplier. The combination was optimized to discriminate undesired straylight due to it's larger incident angle. The reflector as well as the concentrator were both silver coated which allows operation at wavelengths from the near ultraviolet to the near infrared.

4.2 A Diode Laser for Rubidium Spectroscopy

The first tests of the apparatus were carried out with a rubidium atom beam, since an ion (or atom) beam of alkali or earth-alkali elements is easily produced and the required wavelength of 780 nm can be delivered by low-cost laser diodes.
The rest-frame resonance frequency of the $5s\ ^2\mathrm{S}_{1/2} \rightarrow 5p\ ^2\mathrm{P}_{3/2}$ transition in atomic rubidium is $\nu_0(^{85}Rb) = 384.230\ 406\ 373(14)$ THz [Ste08a] and $\nu_0(^{87}Rb) = 384.230\ 484\ 468(62)$ THz [Ste08b] respectively. Hence, the isotope shift between ^{85,87}Rb is roughly 75 MHz but it should be noted that an additional artificial kinematical isotope shift of 2.2 THz at 10 keV beam energy occurs. According to the Doppler formula, the ions at 10 keV are in resonance with the laser in anticollinear geometry if the laser is operated at a frequency of about 384 043 THz. This corresponds to a wavelength of 780.643 nm. To generate laser light of this wavelength, a diode laser in littrow configuration [Ric95] was built. The principles of a diode laser are described quite well in literature. Therefore, the following paragraph gives only a short introduction to grating-stabilized diode lasers.

4.2.1 Laser Design

Diode lasers are attractive since they are low-cost devices that are highly reliable and do not require much maintenance under laser-laboratory conditions compared to Titan-

Sapphire oder dye laser systems. The active medium of a diode laser consists of several layers of doped semi-conductor materials (like AlGaAs or InGaAs). The spectral width is in the best cases a few tens of nm. The central emission frequency is determined by the bandgap between the valence band and the conduction band. However, it can be tuned within a range of typically a few 10 nm by temperature, current variation and by controlled external feedback (see below). The semiconductor material has a relatively high refractive index. Hence, in standard low-cost diodes these facets compose already a low-Q resonator with a reflectivity of more than 30% which already allows for laser oscillation. The emitted wavelength can be changed either by varying the temperature, which changes the optical path length inside the resonator, or by the injection current which influences the charge carrier density and thus the refractive index and the temperature. The disadvantage is that a variation of the temperature changes the frequency of the longitudinal modes and simultaneously shifts the gain profile in an uncorrelated manner. Consequently,

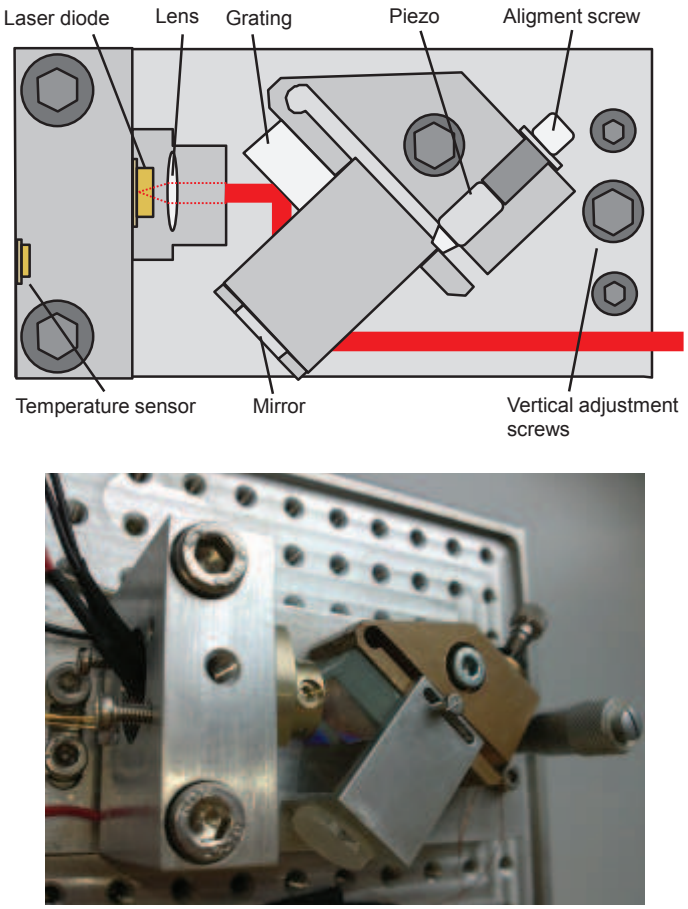

Figure 4.3: Top: Extended cavity diode laser in littrow configuration. The collimated laser beam hits a frequency selective grating where the first order is reflected back into the laser diode. The zeroth order is the laser beam used for the experiment. Bottom: A photo of the diode laser that was assembled for rubidium spectroscopy.

the laser frequency "jumps" at some point to a neighboring mode (mode-hopping), which excludes the operation in some frequency domains. But the main drawback is the spectral linewidth that is about 100 MHz, whereas for collinear laser spectroscopy, a frequency-stabilized narrow-linewidth (1 MHz) laser is mandatory. These limitations of a diode laser are overcome by means of an extended cavity setup. The layout of the grating-stabilized diode laser assembled for Rb is shown in Fig. 4.3. The laser diode is mounted in a lens tube. The lens collimates the laser diode output to an elliptical beam. The output beam falls on a grating (1800 lines/mm for 780 nm) which is tilted to the Littrow angle $2d\,\sin(\gamma) = k\,\lambda$. The Littrow equation states that the incident light diffracts at a wavelength λ under the Littrow angle γ if a grating with a spacing d of the order k is chosen for $k = 1$ the first *i.e.* order reflection is back reflected into the diode. The first order reflection provides the optical feedback into the laser diode. Hence, the cavity is formed between the diode's end facet and the diffraction grating. The grating's zeroth order reflection forms the output beam of the diode laser. An additional mirror is mounted parallel to the grating and fixed to the grating holder in order to reduce beam steering if the wavelength of the laser and thus the incident angle of the grating is changed via the alignment screw or with the piezo-electric transducer (PZT).
Best performance can be reached if laser diodes with anti-reflection (AR) coated end-facets are used. Due to the AR-coating no internal cavity between the diode's facets is formed which mostly suppresses the undesired mode-hopping that occurs if the internal cavity mode competes with the modes of the extended cavity. In this case, the spectral function of the diode is a convolution of the gain profile, the spectral dispersion of the grating and the external cavity modes. If the optical feedback is well aligned one mode of the external cavity can be selected which ensures single-mode narrow-bandwidth operation of the laser. Course wavelength adjustment is provided by the grating alignment screw whereas fine tuning and frequency stabilization can be achieved applying a voltage to the piezo electronic transducer glued on the horizontally grating adjustment screw. For frequency stabilization the bandwidth of the feedback loop is limited by the rather large mass of the grating and its support. Thus, the linewidth of the laser is typically of the order of 1 MHz, which is sufficient for the purpose of CLS. Applying a ramping voltage to the piezo causes a continuous frequency scan of several GHz without mode-hopping if the pivot point is chosen in such a way that the change of the cavity length and the tuning of the littrow angle is synchronous. However, as pointed out before, in collinear laser spectroscopy the laser frequency is usually fixed. Therefore, the frequency can be externally stabilized to an atomic or molecular reference like a cesium or iodine hyperfine transition with a servo loop. In this configuration linewidths of 100 kHz can be reached. The linewidth could be further reduced, applying a fast feedback loop that controls the laser diode current. However, this is not required for operation at TRIGA-SPEC.
Two extended-cavity diode lasers ECDL were built for spectroscopy on Rb and Pr. For the spectroscopy of rubidium a low-price laser diode (Sharp 781JA2C) was used. Diodes in this wavelength ranges are commonly applied in CD-R(W) drives, and the mass production makes them very cheap. A free running output power of more than 100 mW was achieved. With aligned optical feedback, the ECDL delivers in single mode operation about 75 mW at its limit. In order to ensure the lifetime of the diode, it was only oper-

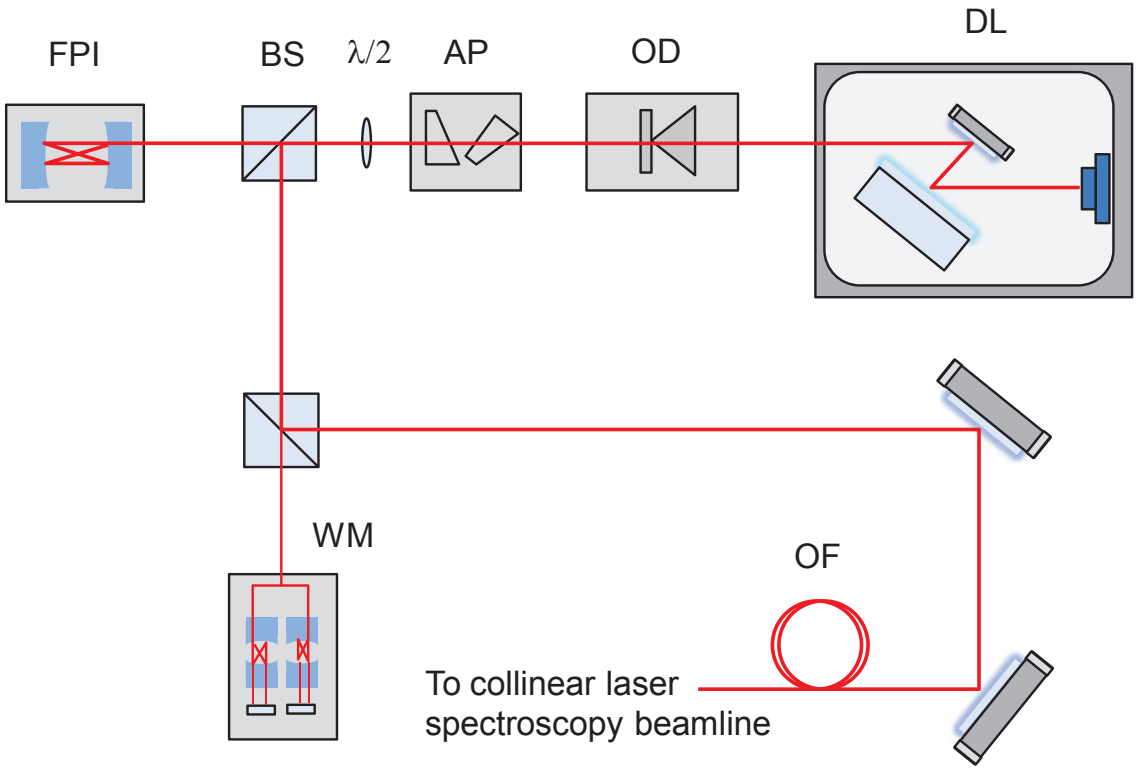

Figure 4.4: Laser setup for Rb spectroscopy. The diode laser (DL) is locked to a high finesse wavemeter (WM). The main beam is coupled into an optical fiber (OF) that is connected to the viewport of the collinear beamline. Single-mode operation is tracked by an fabry-perot-interferometer (FPI). (BS: Beamsplitter, OD: Optical diode, AP: Anamorph prism pair, $\lambda/2$: Waveplate).

ated at lower currents at output powers of 50 mW. Since the diode is not AR-coated the wavelength tuning range is limited between 778 and 786 nm. A photo of the diode laser is also shown in Fig. 4.3.
A schematic drawing of the complete laser setup is depicted in Fig. 4.4. The grating-stabilized diode laser (DL) emits an elliptically collimated laser beam. It passes an optical diode (OD) to avoid any back reflection into the laser diode which would disturb the single-mode operation. An anamorphic prism pair transforms the elliptical into a nearly round beam. A combination of a lambda half plate and a polarization beam splitter cube (PBS) is then used to divide the beam. A small part is fed into a Fabry-Perot-Interferometer to monitor the single-mode operation of the laser diode. With a second beam splitter another beam is created and fed into a wavemeter (WM - High Finesse WS/7) of the Fizeau Interferometer-type to monitor the laser's wavelength and to create a servo signal using a digital built-in PID regulator for frequency stabilization. The main beam (45 mW) is coupled into a 20 m long optical fiber (OF - Nufern 780HP) that transports the light to the collinear beamline. The transmission through the fiber is roughly 50%. Hence, a

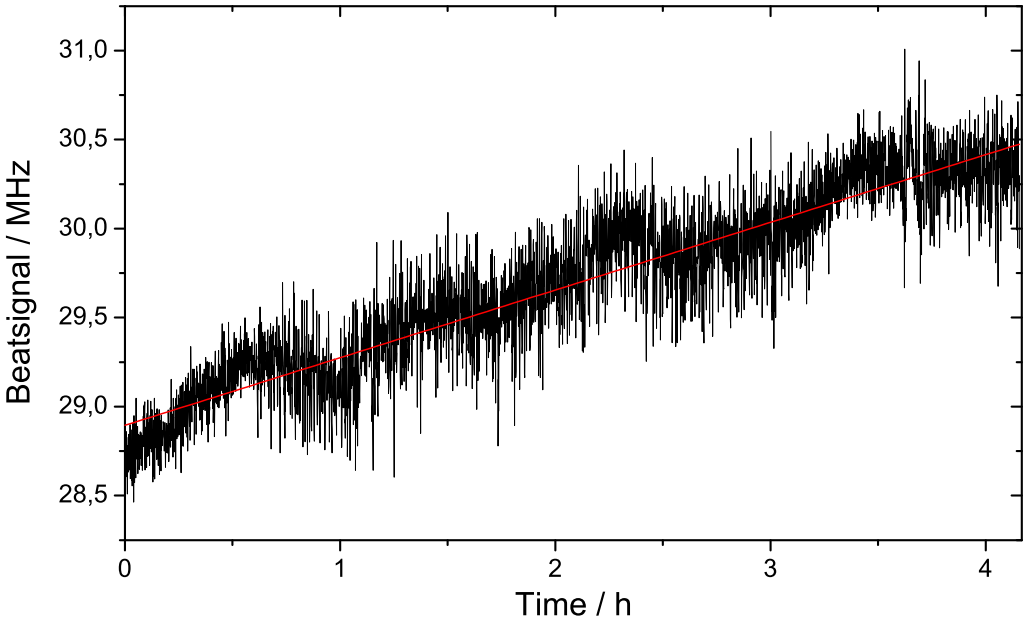

Figure 4.5: Frequency drift of an extended-cavity diode laser with a inexpensive budget laser diode (Sharp 781JA2C) recorded by beating against a frequency comb. The drift-corrected standard deviation after 4 hours is about 260 kHz and a frequency drift of 1.5 MHz is observed.

power of up to 20 mW is available for collinear spectroscopy.
The stability of the locked diode laser under laboratory conditions (minimal noise, air condition, dust-free air) was measured with a frequency comb FC1500 from Menlo Systems. Figure 4.5 shows the time evolution of the recorded beat signal between a frequency comb mode and the stabilized diode laser over 4 hours. The beat signal is electronically detected at about 30 MHz. The data acquisition always integrates over one second. Thus, short-term fluctuations can not be recognized. A measure of the degree of stability is the drift-corrected standard deviation which is about 260 kHz. A frequency drift of 1.5 MHz after 4 hours was observed. Such a drift could be caused by temperature fluctuations that slightly change the optical pathlength in the Fizeau-interferometer's etalon of the High Finesse wavemeter. Consequently, the wavemeter determines a slightly shifted wavelength of the laser and tries to compensate for this by changing the laser frequency. For collinear spectroscopy this stability is sufficient in most cases since the reference isotope and the isotopes under investigation are measured repeatedly by quickly switching between them. However, this result was achieved under laboratory conditions and would be worse if the laser and particularly the wavemeter are placed in the reactor hall. For that reason, additional vibration isolation material (sorbothane sheet - 6.5 mm thickness) was put around the diode laser housing. This sheet absorbs up to 95% of the impacting energy and hence improved the passive stability of the laser inside the reactor hall.

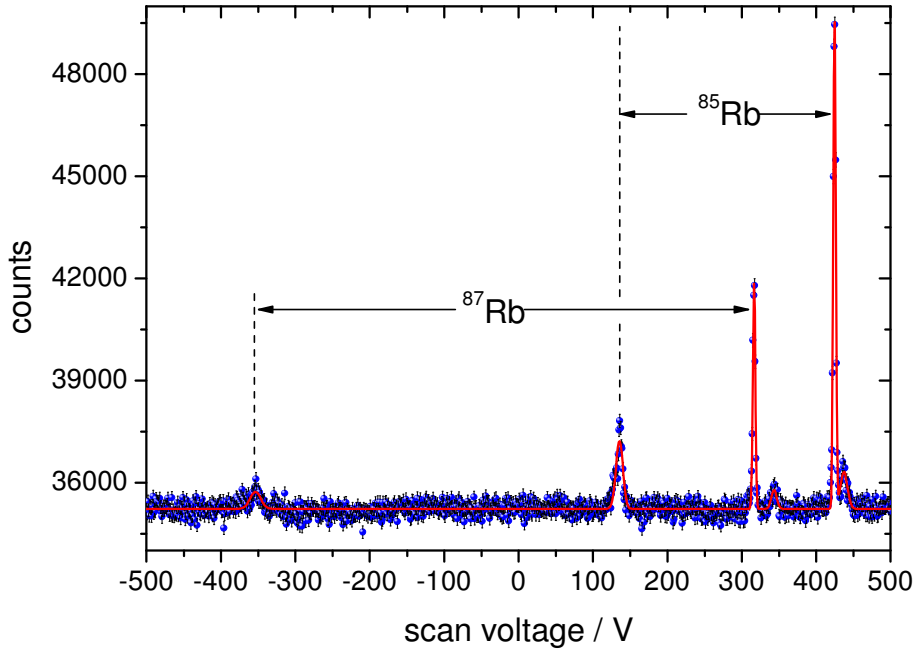

Figure 4.6: The hyperfine structure of stable rubidium isotopes. The isotope shift between ^{85,87}Rb is only 75 MHz. The depicted spectrum is the sum of 10 scans with a dwell time of 20 ms per channel and 1 V stepsize and an atom beam intensity of about $1.2 \cdot 10^8$ atoms/s [Kra10]. Only the strongest components of the hyperfine structure are visible.

4.2.2 First Test Experiment

A stable 10-keV ion beam of rubidium ^{85,87}Rb was produced with the off-line ion source by surface ionization. The transmission of the ion beam through the beamline was about 70% measured with a faraday cup inside the 10° deflector and after the charge exchange cell. A charge exchange efficiency with potassium vapour of nearly 100% was demonstrated at heating temperatures of about 200°C and atom beam currents up to 60 nA were easily achieved [Kra10]. In this experiment the cell was heated to 140°C according to an charge-exchange efficiency of only 10%. Such a low temperature was chosen to minimize additional collisions of the atoms inside the CEC which leads to losses of the kinetic energy and therefore to asymmetric lineshapes.
The laser beam was attenuated to 1.5 mW at the entrance window. A transmission of nearly 95% was achieved at a PMT background rate of about 15 000 cts/s. Spectroscopy was performed with an atom beam flux of about $2 \cdot 10^8$ atoms/s measured on a faraday cup behind the charge exchange cell. Lacking a mass separator, the measured beam flux includes all isotopes that are produced in the surface ion source. The laser was stabilized at a wavelength of $\lambda = 780.643$ nm.
Spectra of one of the two fine-structure doublets, namely the $5s\ ^2\mathrm{S}_{1/2} \rightarrow 5p\ ^2\mathrm{P}_{3/2}$ transition, were recorded applying the Doppler-tuning voltage $U_{\mathrm{scan}} = \pm 500$ V at the charge

Table 4.1: Ground state splitting of the $5s_{1/2}$ level and isotope shift of stable rubidium ^{85,87}Rb measured as a first test at the TRIGA-LASER collinear beamline . The values are compared to the literature values from [Pen62, Bar91]. The first uncertainty of the experimental values is the statistical uncertainty and the second one is the systematic uncertainty arising from the limited knowledge of the acceleration voltage $\left(\frac{\Delta U}{U} = 10^{-4}\right)$. All values are in MHz. Taken from [Kra10].

	TRIGA-LASER	Literature
^{85}Rb	3034(1)(6)	3035.732(50)
^{87}Rb	6835(1)(6)	6834.682(50)
^{85,87}Rb	−77(2)(6)	−78.095(12)

exchange cell. A typical spectrum of ^{85,87}Rb is shown in Fig. 4.6. Two of the main peaks represent the transition in ^{87}Rb and the other two in ^{85}Rb as indicated. The isotopes ^{85,87}Rb exhibit a nuclear spin I of $I = 5/2, 3/2$, respectively, that couples to the total angular momentum J. The atomic angular momentum $F = I + J$ takes values of $F = 2, 3$ $(1, 2)$ in the ground state ^{85,87}Rb and $F' = 1, 2, 3, 4$ $(0, 1, 2, 3)$ in the excited state. Thus, six hfs components are expected per isotope but only three of them are visible in Fig. 4.6. This is caused by the weakness of the ofter transitions, optical pumping and the relatively high background. A detailed analysis of the rubidium hyperfine multiplet, can be found in [Kra10]. A multiple voigt profile (red) is fitted to the observed peak structure. From these peaks, the ground state splitting of the strongest hyperfine level is calculated and compared to the literature values in Tab. 4.1. The results agree very well, demonstrating the reliability of the laser spectroscopy and the collinear beamline. Hence, this spectroscopy was used in [Kra10] to investigate the performance of high voltage power supplies and a voltage divider.
During these test measurements it was found that the environment of the reactor hall is not an ideal place to operate narrow-bandwidth lasers. Since the reactor hall is operated in under-pressure regime, pressure changes of the order of typically 2 mbar arise whenever one of the halldoors is opened. Additionally, temperature fluctuations between 21°C and 28°C were tracked inside the reactor hall. This, and the unavoidable noise in the hall, where several experiments are installed, cause massive disturbances to the laser. As a result, the laser jumps out of lock or even starts mode-hopping prohibiting long-term measurements.

4.3 MOPA Diode Laser System with a Tapered Amplifier

Most of the transitions to be investigated at TRIGA-LASER require laser light in the UV region somewhere between 300 - 450 nm. For example, an accessible transition in atomic molybdenum is the $4d^5(^6\mathrm{S})5s \rightarrow 4d^5(^6\mathrm{S})5p$ which requires light of 390 nm or

the $4d^5(^6\mathrm{S})5s^2 \rightarrow 4d^5(^6\mathrm{S})5s(^7\mathrm{S})5p$ transition in atomic technetium which is accessible at 430 nm. Further refractory elements with transitions in this range are niobium (412 nm) and rhodium (396 nm).
During our off-line tests we focused on the wavelength range around 390 nm. In general there are two options available to produce that wavelength with diode lasers required for the spectroscopy on Ca^+ and Pr^+. While commercial laser diodes in the 370 - 490 nm regime are in principle available, they are expensive, often not AR coated and have a very limited tuning range. In most cases the threshold current for laser operation is very close to the operating current which makes the lasing process very sensitive to the applied diode current. Furthermore, hand-selected diodes that can cover the desired wavelength are even more expensive and their wavelength tuning range is typically limited to only a few nm. Therefore it appeared more practicable to set up a master-oscillator power amplifier (MOPA) system in the red or infrared range which is then frequency doubled to obtain the required light in the blue or UV-region. The master oscillator produces the narrow-linewidth laser light and is frequency stabilized. However, higher powers than the typically available 50 mW from the ECDL is required for efficient frequency doubling. Therefore a so-called tapered amplifier is used to amplify the ECDL output. These amplifiers are electronically pumped semiconductor-layers with fully AR-coated facets. The active medium can be operated with high currents (commonly up to 4 A) without laser operation. Amplifier chips are mainly available for the wavelength range of 670 - 1120 nm. A schematic drawing of such an amplifier is shown in Fig. 4.7. Several layers of semiconductor materials form the active amplifier region. In order to keep the power density constant a tapered area is necessary. The input facet has a waist of a few ten μm and is followed by a waveguide for spectral mode cleaning. The output facet has a width of a few hundred μm and the total length of a chip is typically a few mm. Seeding powers of a few mWs are sufficient and can be amplified to an output power of several Watts without significant amounts of amplified spontaneous emission (ASE). The MOPA was designed to perform spectroscopy on Ca^+ and Pr^+ ions. Ca^+ served for the characterization and development

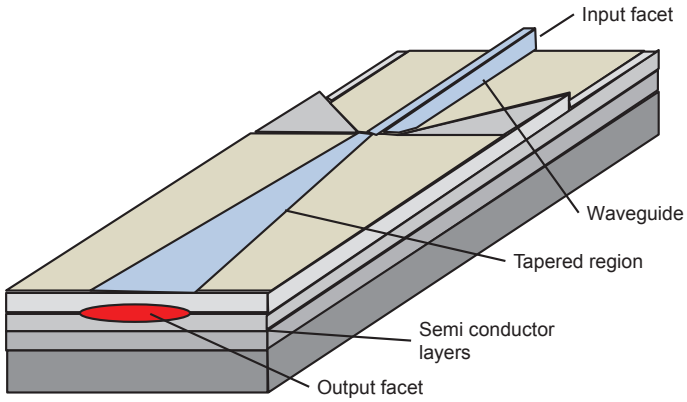

Figure 4.7: Schematics of a tapered amplifier chip. An electronically pumped semiconductor transition with AR coated end facets amplifies the input beam. The tapered layout region ensures a constant power density distribution.

of the new FDR and the ion-photon coincidence detection unit. The stable $^{40}Ca^{+}$ has two dipole transitions from its ground state to the excited states: $4s\ ^2S_{1/2} \rightarrow 4p\ ^2P_{1/2,3/2}$. In order to drive these two transitions a wavelength of 397 nm and 393 nm, respectively, is required. Finally, the $4f^3\ 6s(^5I_4) \rightarrow 4f^3\ 6p(4H_3)$ transition in $^{141}Pr^{+}$ at a wavelength of 390 nm was investigated for an on-line experiment at ISOLDE [Fro13].

4.3.1 The Master Oscillator

As a master oscillator a second ECDL as shown in Fig. 4.3 was constructed and equipped with an AR coated laser diode (Eagleyard Photonics 0840-06010-1500-SOT02-0000). The diode shows an emission spectrum which is shifted to shorter wavelengths compared to the manufacturer's specifications. A tuning range between 782 and 840 nm and a maximum output power of 30 mW at 810 nm was demonstrated. At the desired wavelength of 786 nm up to 10 mW laser power are produced. The polarization is parallel to the long axis of the elliptical output beam. The efficiency of a grating is higher if the polarization of the incident light is parallel to the grooves, but the resolution improves with the number of grooves that are illuminated. Hence the long axis should be perpendicular to the grooves and the polarization must be perpendicular to the long axis. For that reason a $\lambda/2$ waveplate is inserted between the collimation lens and the grating. The diode laser was again externally stabilized to the High Finesse wavemeter WS7. The stability of the frequency-stabilized diode laser was measured with the frequency comb. Figure 4.8 shows the time evolution of the beat signal between the frequency comb mode and the stabilized diode laser over 900 s. The standard deviation is about 350 kHz. A negligible frequency drift of 180 kHz was observed. As discussed above, these results are not reproducible if the laser is placed inside the reactor hall due to the unfavorable conditions.

4.3.2 The Tapered Amplifier

The setup of the MOPA system is shown in Fig. 4.9. The 10 mW output beam of the diode laser passes an optical diode (OD) to avoid any back reflection into the master oscillator which would cause frequency instabilities. It should be noted that the amplification of the TA is to a large part determined by the coupling efficiency of the seeding light into the waveguide of the TA. Therefore, the input beam from the diode laser must be transformed in shape (TEM00) and size to the waveguide mode. Thus, an anamorph prism pair (AP) is used to transform the elliptical beam into a round beam with a 1.5 mm waist. The collimated beam is coupled into the waveguide of the tapered amplifier (TA) with two mirrors. In the initial setup, an additional optical fiber was used for mode cleaning before the TA. However, it was later removed since the waveguide of the TA itself acts as a mode cleaner. Any back reflection into the TA causes instabilities and has therefore to be avoided by another optical isolator. The output power measured behind the optical isolator against the current applied to the TA is plotted in Fig. 4.10.

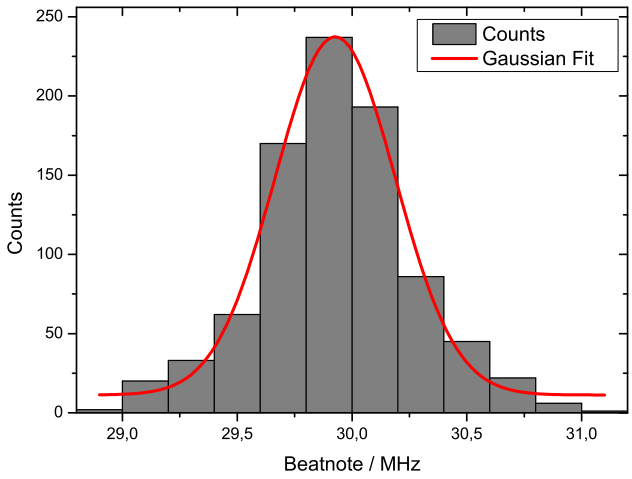

Figure 4.8: The frequency drift of the extended-cavity diode laser built for the spectroscopy of Pr^+ at 793 nm was measured detecting a beat signal between the diode laser and a frequency comb mode. The laser is again stabilized to the wavemeter (details see text). The standard deviation, taken as the FWHM of the Gaussian fit (red), is about 350 kHz over a period of 900 s. A negligible drift of 180 kHz was observed.

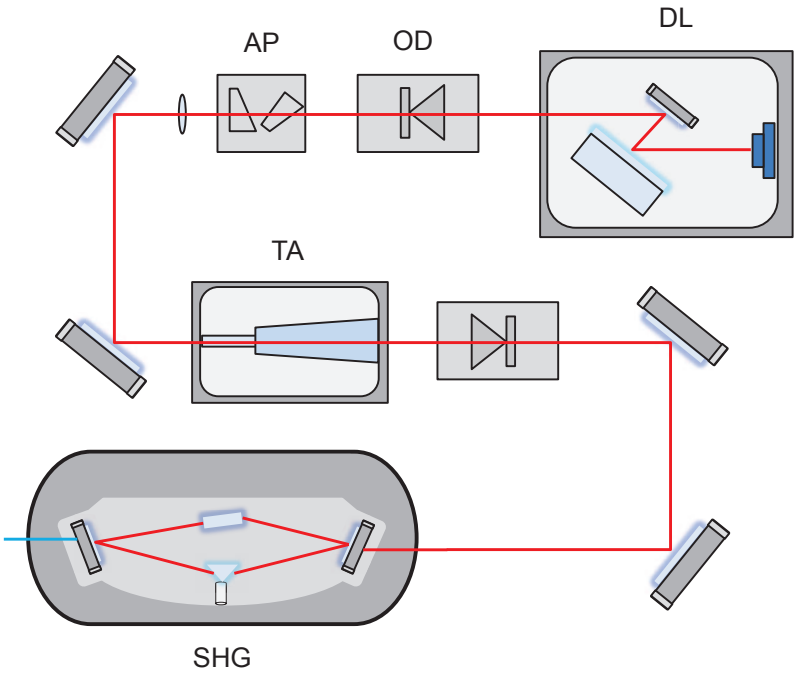

Figure 4.9: Setup of the MOPA system with a frequency doubler. The diode laser (DL) is protected against any back reflections by an optical diode (OD). The elliptical output beam of the diode laser is transformed into a round beam by passing an anamorph prism pair (AP). Two mirrors are used to couple the light into the tapered amplifier (TA). Another optical diode protects the TA against undesired back reflections. The amplified output beam is coupled into a second harmonic generator (SHG).

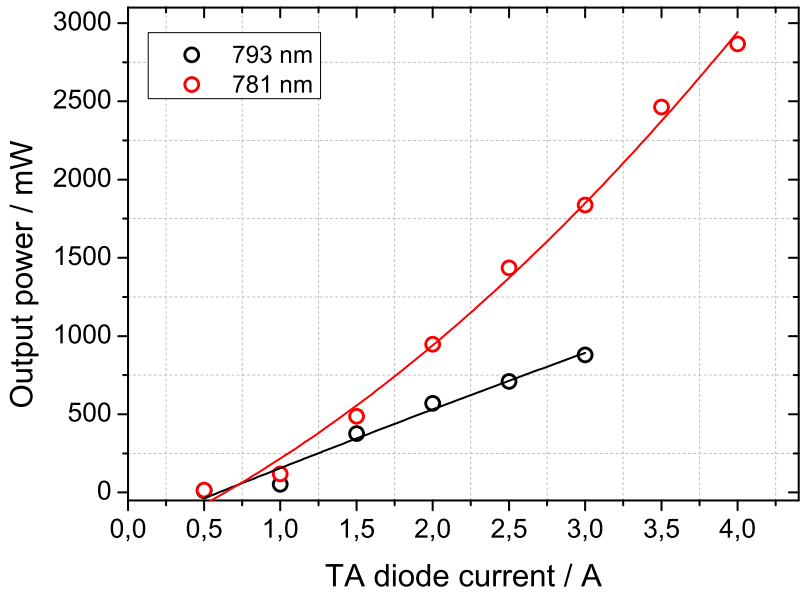

Figure 4.10: Output power of the tapered amplifier at 781 nm and 793 nm as a function of pumping current at a power of 12 mW. Note that the output at 4 A was measured with an input power of 25 mW.

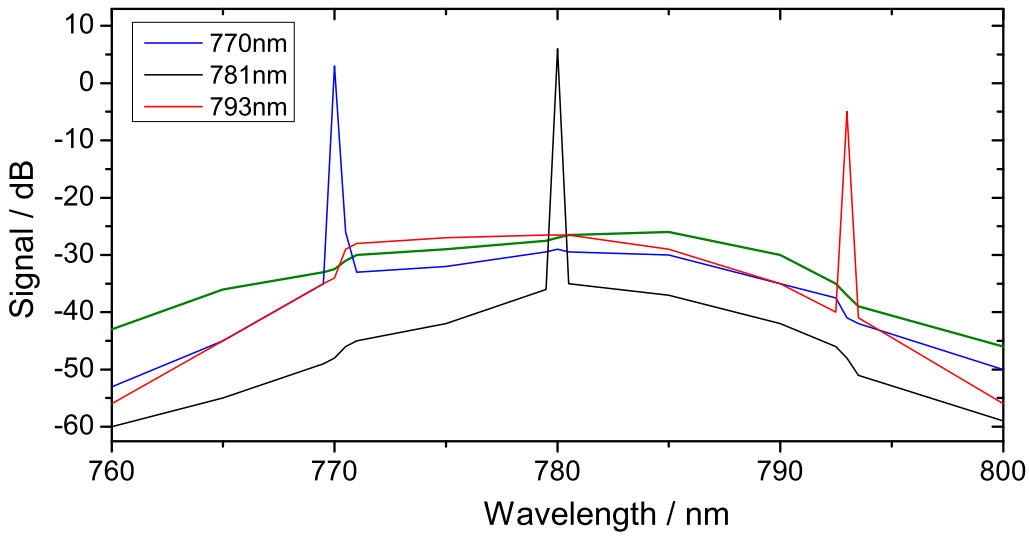

Figure 4.11: Emission spectrum of the tapered amplifier (TA) operated at 4 A diode current and seeded with different wavelengths in the center and at the edges of the amplifier gain profile. The green line shows the spectrum of the amplifier in absence of a seed laser. The TA was operated at a temperature of 21°C constantly during the measurements at 770 nm and 781 nm and at 25°C at 793 nm.

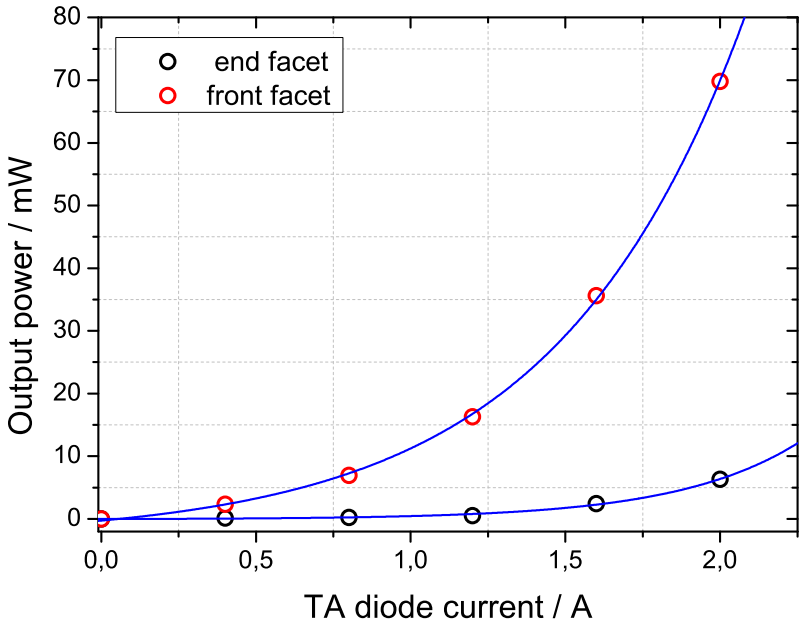

Figure 4.12: Amplified spontaneous emission of an AR coated tapered amplifier (TA) diode that occurs without seeding versus the TA diode current. The TA diode emits several tens of mW back to the master oscillator. An optical diode must be used in order to avoid any back reflection into the master oscillator. At least one tenth of the front facet's output is unfavorable amplified spontaneous emission.

Since the TA is not specified to amplify wavelengths outside the range of 775 - 784 nm, the emission spectrum was shifted to larger wavelengths by operating the TA chip at 25°C instead of the factory settings at 21°C[1]. The emission spectrum of the tapered amplifier output was measured with an optical spectrum analyzer at different wavelengths and is depicted in Fig. 4.11. Seeding the TA chip at the center of the amplifier gain profile (781 nm) results in sidemode suppression of about 42 dB, whereas operation at the edges of the gain curve a suppression of 30 dB for 770 nm and of 20 dB at 793 nm was obtained. As already mentioned, amplifier devices deliver also spectral components that are caused by an amplified spontaneous emission (ASE). The fraction of ASE is estimated measuring the output power of the TA chip at the front- and backside in the absence of a seed laser. The results are also included in Figs. 4.11 and 4.12. For safety reasons only half of the maximum current was applied to the TA diode during this measurement. Above 2 A, more than 10 mW of ASE is emitted from the input facet towards the direction of the seeding source. Therefore an optical isolator of at least 40 dB is required to protect the seeding laser. In contrast, the front facet emits at this current about 100 mW of ASE. Even though wavelengths outside the specifications can be amplified to a few hundred

[1]It was further observed that the TA heats up quite quickly and the temperature watchdog is not able to control the temperature at 4 A for several hours. Therefore additional cooling fins and heat-conductive paste were added for a better heat conduction to the huge laser table. However, during the measurements it was not necessary to drive the TA diode with more than 2.5 A.

Table 4.2: Typical operation parameters of the MOPA system installed at TRIGA-LASER.

Characteristic	Ca^+	Pr^+
Wavelength /nm	397	390.5
DL power /mW	10	30
MOPA power (at 2.5 A) /mW	720	1430
ASE suppression /dB	20	42
SHG output /mW	15	140
SHG efficiency	2%	10 %

mW (as shown in Fig. 4.10), they are "contaminated" by a large amount of ASE. As an example, the TA seeded at 793 nm with 12 mW input power emits about 500 mW but at least 20% of the laser radiation is unfavorable ASE. However, the amplified output beam is then coupled into an enhancement cavity for frequency doubling which removes the largest part of the ASE.
In total, two different laser diodes had to be used to generate the required wavelengths for Ca^+ and Pr^+. Since the wavelength for Pr^+ is in the central of the amplification gain of the TA at 781 nm, this wavelength was used to characterize the MOPA system. The laser diode was changed against an uncoated model Sanyo DL7140-201S which emits about 30 mW in the ECDL configuration at 781 nm. About 12 mW are coupled into the TA diode. The output power of the TA diode at this wavelength increased by far compared to the operation with a seeding wavelength at 793 nm as shown in Fig. 4.10. Typical operation parameters are summarized in Tab. 4.2.

4.3.3 Frequency Doubling

The non-linear process of frequency doubling is widely used to generate the second harmonic of the laser's fundamental wavelength. For that purpose the fundamental laser wavelength is focused inside a crystal of *e.g.* barium beta borate BBO or lithium triborate LBO. In case of continuous-wave lasers the conversion efficiency of single-path frequency doubling is rather low: a few mW are obtained with 1 W fundamental power. Therefore the power is enhanced using a commercial enhancement-cavity in a delta (Spectra Physics Wavetrain) or a bow-tie (Tekhnoscan frequency doubler) configuration.
The fundamental laser light was mode-matched to the fundamental mode of the respective resonator before being directed into one of the frequency doubling cavities. Even though the output beam of the TA has an elliptical beam profile an aspheric lens for mode-matching into the frequency doubler was sufficient to achieve hundreds of milliwatts in the second harmonic. Although the obtained conversion efficiency of about 10% is well below the typical values for commercial frequency doublers (typically 40% at such input powers) the output exceeds the desired power of 10 mW by one order of magnitude. After

beam shaping using two cylindrical lenses the UV light was coupled into a single mode fiber (Nufern S405HP) and a transmission of about 40% towards the collinear beamline was obtained.

4.4 Spectroscopy of Ca^+ and Pr^+ Ions

Several spectra of $^{40}Ca^+$ were recorded to benchmark the new optical detection chamber in the UV-region. A typical spectrum with an ion beam current of about 200 pA and 0.5 mW laser power is shown in Fig. 4.13 (left). A voigt profile was fitted to the resonance curve using a χ^2-minimization method. The Lorentzian linewidth is about 29 MHz which is close to the natural linewidth of 23.5 MHz and the Gaussian contribution is 56 MHz. A detection efficiency of one photon per 1000 ions was observed [Ham10]. The signal-to-noise ratio (SNR) in the spectrum is above 150 at an ion beam current of 200 pA from the off-line ion source. The production rate of the neutron-induced fission products at the

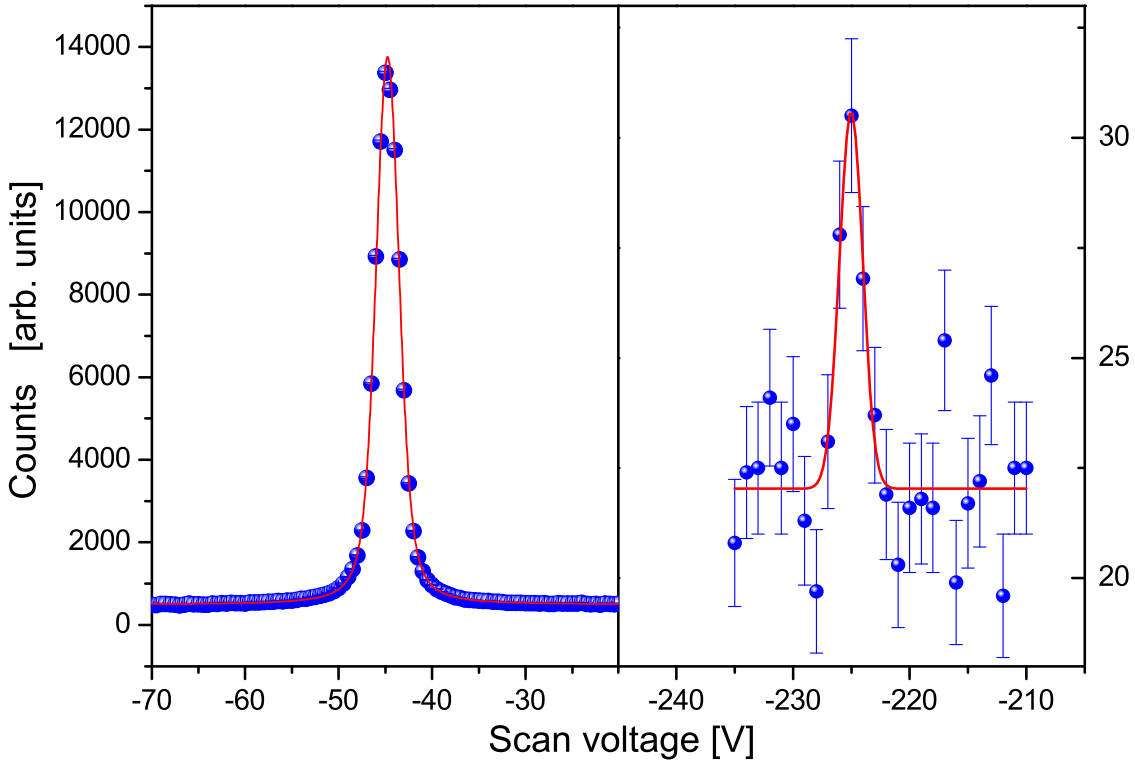

Figure 4.13: Resonance spectra of stable $^{40}Ca^+$ in the $4s\ ^2S_{1/2} \rightarrow 4p\ ^2P_{3/2}$ D_2 transition. The left spectrum is the sum of ten individual scans at an ion beam current of 200 pA and a laser power of 0.5 mW. A voigt profile (blue) fits well to the resonance curve. The ion-photon coincidence spectrum (right) was recorded at an ion beam current of only 9000 ions/s and summed up for 20 minutes.

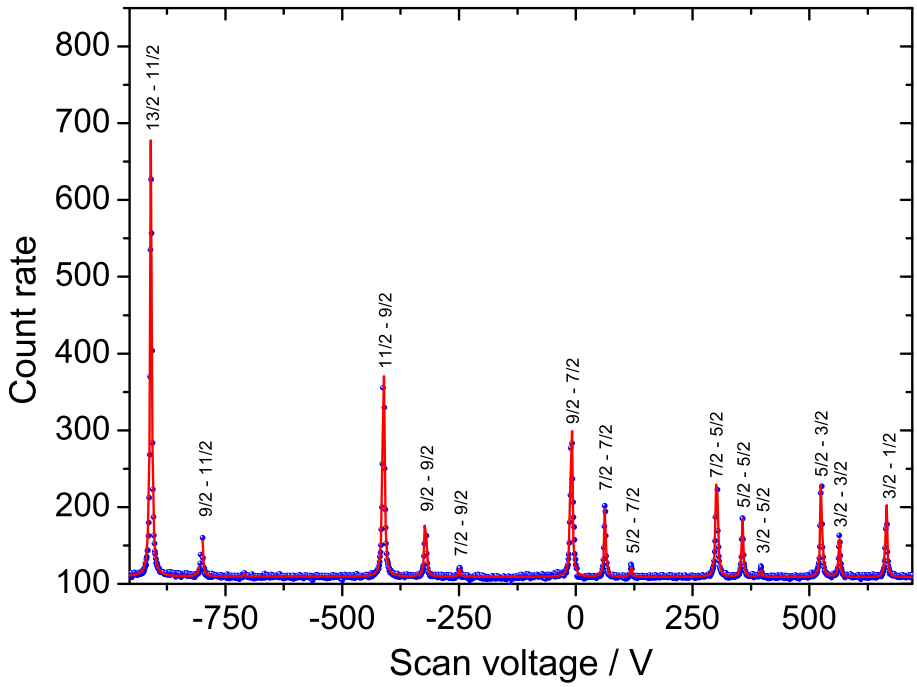

Figure 4.14: The hyperfine multiplet of the investigate the $4f^3\ 6s(^5I_4) \rightarrow 4f^3\ 6p(4H_3)$ transition in stable $^{141}Pr^+$ (black). The change of the angular momentum J to $J = 4 \rightarrow J' = 3$ and a nuclear spin $I(^{141}Pr) = 5/2$ results in a total of 15 hyperfine transitions. They are fitted by a multiple Voigt profile (blue) to extract A- and B-factors of the hyperfine structure and the center of gravity. For more details see [Fro13].

on-line ion source will be much lower and ion beam currents well below 1 pA are expected continuously decreasing with increasing distance from the valley of stability. An evaluable spectrum can be achieved by increasing the measurement time up to hours or even days provided that the laser system is stable over the measurement time and the background is low. The stability of the wavemeter, as demonstrated above, is not sufficient. Moreover, a frequency comb is available and will allow to lock the laser to a well-known absolute frequency for very long times as will be shown below. As mentioned in Chapter 3.3.1 a photon-ion coincidence detection unit enhances the SNR especially at low ion beam currents which enables the detection of resonance spectra at ion beam currents in the fA range in time scales of a few hours with a reasonable SNR. For that purpose a photon-ion-detection unit was commissioned [Sie10]. It was used for spectroscopy of Ca^+ ion beam currents of 9000 ions/s. After 20 minutes a resonance spectrum was recorded which is shown in Fig. 4.13 (right). Within that time no resonance was visible in the purely optically detected spectrum without coincidence condition. Specification measurements resulted in a detection efficiency enhancement by a factor of about 100 [Sie10]. Coincidence detection was also used for the beryllium spectroscopy described in Chapter 5. However, it is only of limited applicability for the spectroscopy at TRIGA-LASER, since most of the fission products will suffer from a large isobaric background that cannot be discriminated.

The MOPA system was further used to investigate the $4f^3\ 6s(^5I_4) \rightarrow 4f^3\ 6p(4H_3)$ transition in stable $^{141}Pr^+$. A typical spectrum of the hyperfine multiplet is depicted in Fig. 4.14. The ion beam current was about 400 pA and the laser beam attenuated to 900μW. Fitting a multiple Voigt function to the hyperfine multiplet (red line) provides the A- and B-constants of the hyperfine structure as well as the magnetic moment. According to the reference isotope $^{141}Pr^+$ the magnetic moment of the radioactive $^{140}Pr^+$ is to be investigated at COLLAPS/ISOLDE. The latter delivers significant information for many different narrative accounts for the GSI Oscillations [Lit08] that are controversially discussed in the literature.

4.5 Frequency Comb Stabilized Titanium Sapphire Laser System

The laser systems described so far were adapted for a single transition in one ion species. All of them were operated inside the reactor hall on a small laser table that fitted besides the collinear beamline. To overcome both problems, the limited stability of laser operation in the hall and the large effort required to adapt a diode laser system for each ion species, a more versatile laser system was installed in the laser lab and and optical connection between the reactor hall and the laser lab was established.
To cover a broad spectral range, a Titanium Sapphire ring laser Ti:Sa (Sirah MATISSE TS) was installed in the laser lab. It is pumped by a frequency-doubled diode-pumped Verdi V18 (Nd:YVO4) solid state laser at 532 nm. The spectral bandwidth of the gain medium, a titanium-doped sapphire crystal, covers a wavelength range of 700 to 1030 nm. A schematic view of the MATISSE ring laser is shown in Fig. 4.15. The path of the pump beam (green) is adjusted by the two pump mirrors in such a way that it passes the first cavity folding mirror and is focused into the Ti:Sa crystal to match the mode diameter of the cavity down to a few hundred μm. This ring resonator consists of six mirrors, two curved folding mirrors which create the focus at the crystal between the two piezo mirrors for varying the cavity length, an out-of-plane mirror (OP), and an output coupler.
A terbium-gallium-garnet plate placed in a strong permanent magnetic field forms an optical diode. Based on the Faraday effect the polarization of the light is rotated when passing the crystal and the rotation direction is independent of the propagation direction. The out-of-plane mirror rotates the polarization for a second time. The polarization of a light wave propagating counter-clockwise is rotated by -2° due to the out-of-plane mirror and re-rotated +2° by the optical diode. A light wave propagating clockwise has its polarization rotated +2 degrees twice and therefore experiences additional losses due to the Brewster surfaces of the optical elements inside the resonator. If light propagates the ring resonator in only one direction, standing waves do not exist and the unfavorable spatial hole burning and the accompanying mode competition is suppressed.
Single-mode operation is obtained by reducing the gain for all other modes so that only one longitudinal resonator mode can oscillate. For that purpose three additional frequency-selective elements are installed. Coarse wavelength adjustment is performed with the birefringence filter which resizes the width of the active gain profile to several THz. It

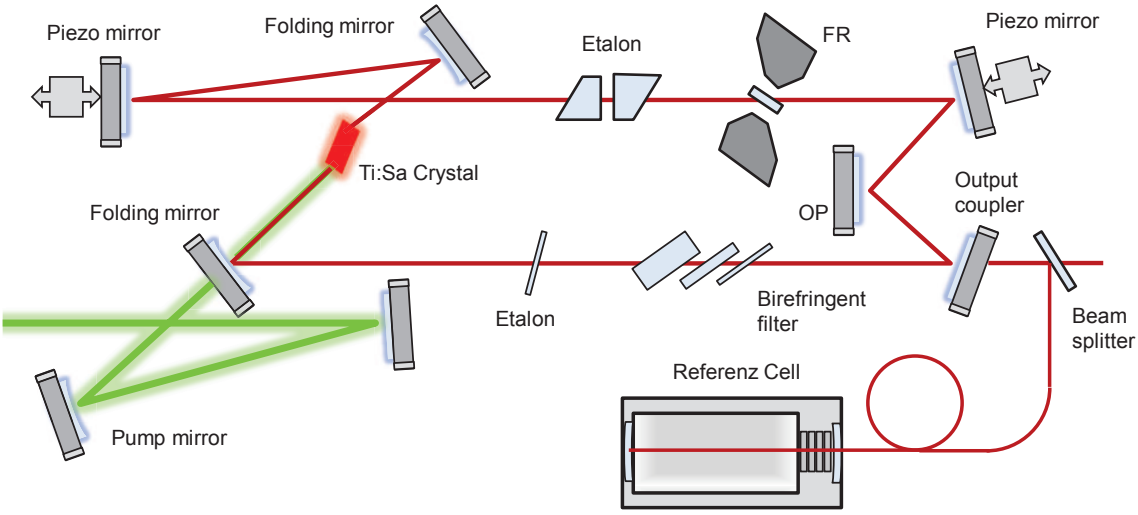

Figure 4.15: Schematic view of the MATISSE TS laser. Six mirrors form a ring cavity. Single-mode operation is achieved with several frequency selective elements, a birefingent filter, a thick and a thin etalon and the ring resonator itself. Unidirectional lasing is ensured by the combination of an out-of-plane (OP) mirror and a Faraday Isolator (FR). Laser frequency drifts are detected with a temperature-stabilized reference cell and compensated using the piezo-driven mirrors.

basically consists of three quartz plates with a thickness ratio of 1:3:15 and uses the birefringence to rotate the polarization for all except one frequency. Only for one frequency range the combined effect of all three plates compensates and the polarization is not rotated. For all other frequencies the rotated polarization increases cavity losses and laser oscillation is suppressed. The next frequency-selective element is a thin quartz etalon (400 μm) which selects modes with a free spectral range of about 250 GHz. Further frequency selection is performed by a narrow-bandwidth thick etalon with a free spectral range of 20 GHz. The cavity of the ring laser itself has a length of about 1.7 m. Therefore the free spectral range of the cavity is 165 MHz. All elements must be tuned in order to achieve a single mode operation of the laser.
Fine tuning of the wavelength is achieved by changing the length of the cavity. A piezo transducer stacked to the tuning mirror corrects drifts with a low bandwidth. Faster corrections are done with the tweeter mirror.
Dependent on the ambient conditions of the laser, the frequency drifts some 100 MHz on time scales of a few minutes. To eliminate these drifts, the resonator length is stabilized to a temperature-stabilized high-finesse cavity. The output coupler of the laser separates a small fraction of the laser beam into an optical fiber that is connected to the reference cavity. Inside the cavity this beam is further divided into two beams of equal intensities. The first one is coupled into the reference resonator and its transmission function detected with a photodiode. A reference point at half of the peak height is set automatically and serves as a servo signal for the stabilization of the length of the ring resonator. Laser power

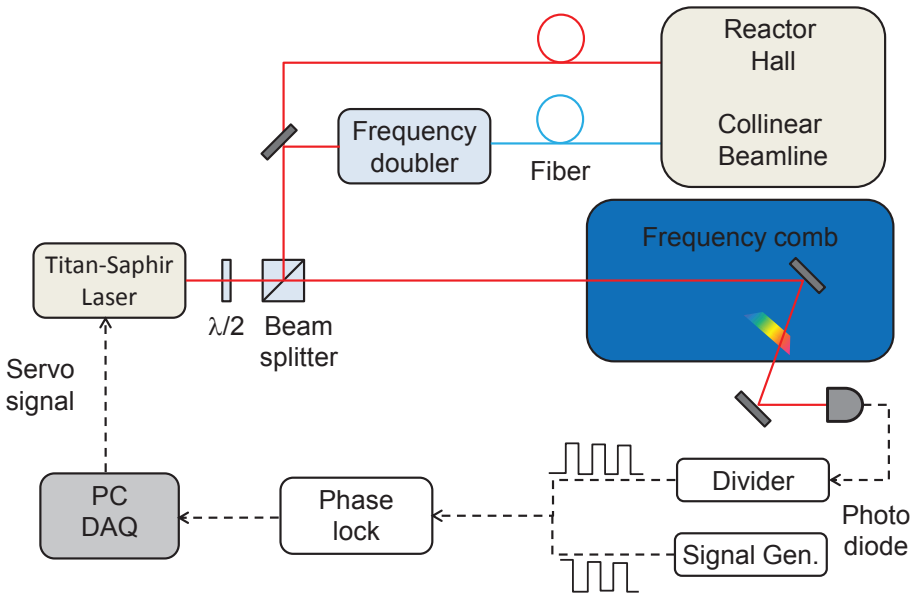

Figure 4.16: A stabilization setup for the titan:sapphire MATISSE laser at TRIGA-LASER. The frequency drift is eliminated by stabilizing the laser's frequency to a frequency comb. The output of the Ti:Sa laser either directly coupled into an optical fiber or passes a frequency doubler and the second harmonic is then coupled into the second fiber for the blue and near-UV region. The fibers guide the light along 150 m to the collinear beam line inside the reactor hall.

fluctuations do not influence the servo signal, since the second beam from the optical fiber do not pass the cavity, but serves as an intensity reference. Even though this stabilization cell is temperature stabilized, ambient temperature and pressure changes still influence the stabilization cell and thus lead to a slow drift in the locking point. Such so-called long-term drifts can be eliminated if the stabilization cell is again stabilized to a reference, *e.g.*, an ultra-stable cavity or a molecular or atomic reference. For that purpose one of the resonator mirrors is stacked on a piezo transducer to control the length and thus the position of the transmission peaks of the stabilization cell. If an error signal $(0 - 3)$V generated by a servo loop is fed into the external input of the control box it is applied to the reference cavity piezo and the frequency of the laser will follow the reference. With such a setup long-term fluctuations are strongly suppressed, whereas the correction of fast short-term fluctuations are limited to about 70 kHz/100 ms by the bandwidth of the servo system. This can be increased using an EOM inside the cavity as it is available for the MATISSE TX which offers linewidths of less than 30 kHz/100 ms. In the TS configuration with the MOS-2 mirror set and a pump power of 18 W the MATISSE TS laser emits about 4 W in a frequency range of 770 - 860 nm and up to 5 W are achieved around 782 nm. For high precision laser spectroscopy experiments the laser frequency must be stabilized to an accuracy of 1 MHz or better. The MATISSE TS laser is therefore directly stabilized to a frequency comb. The setup is schematically drawn in Fig. 4.16.

A variable part of the laser output, usually a few milliwatts, is coupled into a frequency

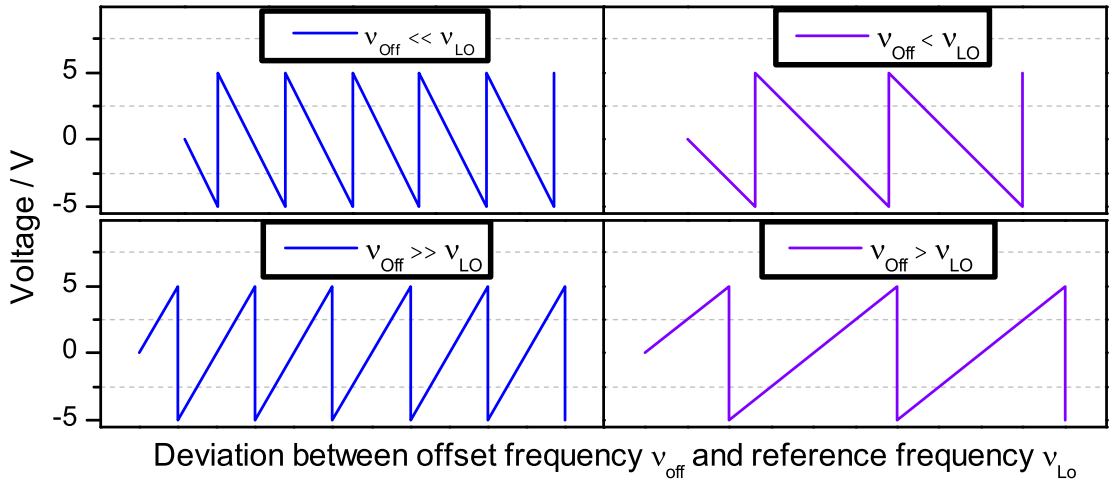

Figure 4.17: Servo signals from a phase comparator. The graph A (B) in the upper trace shows the servo signals from a phase comparator when the offset frequency ν_{Off} is (much) lower than the reference frequency ν_{LO}. Whereas in graph C (D) in the lower trace the offset frequency ν_{Off} is (much) higher than the reference frequency ν_{LO}. The slope of the sawtooth-like signal is proportional to the deviation of the offset frequency ν_{Off} and the reference frequency ν_{LO}.

comb (Menlo Systems - FC1500) where an optical beat between a comb mode and the laser mode is detected on a fast photodiode. Its intensity is directly modulated with the frequency difference between the laser and the comb mode. A digital phase-locked loop is used to compare the beat signal frequency with the set frequency. Therefore the beat signal is fed into a frequency divider that divides the frequency by a given ratio between 2 and 256 and converts it into a TTL signal which is subsequently delivered to the phase-lock loop. A TTL signal from a signal generator that is locked to an atomic clock, which also serves as a reference for the frequency comb itself, is the local oscillator signal for the phase-lock loop. The latter detects the rising and falling slopes of both signals: A rising slope of the local oscillator (LO) increases the internal counter of the phase comparator by 1 and the rising slope of the photodiode signal decreases the counter by 1. The local oscillator, in this case derived from a 10 MHz rf reference, is compared against the offset beat note detected with the photodiode. The counter register is converted into an analog voltage proportional to the relative phase. Figure 4.17 schematically shows the output signal for two cases: In the upper trace (A) the offset frequency ν_{Off} is much lower than the local oscillator frequency ν_{LO} and a sawtooth-like signal with a steep falling slope is created. In Graph (B) the offset frequency ν_{Off} approaches the ν_{LO} and thus, the slope becomes flat. The slop is zero, if $\nu_{\mathrm{Off}} = \nu_{\mathrm{LO}}$. On the other hand, the slope of the sawtooth-like signal rises when the offset frequency ν_{Off} is above the reference frequency ν_{LO} as depicted in (C) and (D) accordingly. Thus, it was not possible to lock the Ti:Sa laser directly with this signal by feeding it into the MATISSE stabilization electronics. The MATISSE laser can

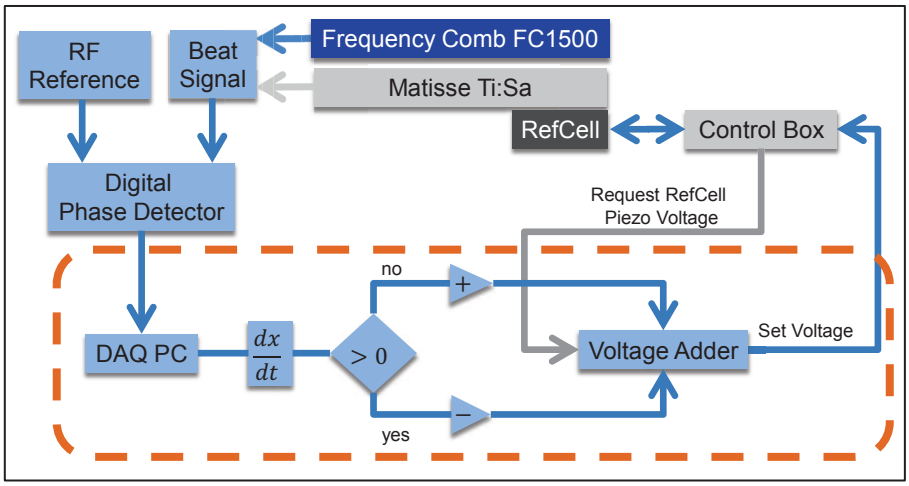

Figure 4.18: Stabilization scheme to lock the frequency of the MATISSE Ti:Sa laser to a mode of the optical frequency comb FC1500 from Menlo Systems. Items in the orange box are controlled by the LabVIEW Virtual Instrumentations (VIs). For details see text.

be stabilized using a PID regulator programmed in LabVIEW. The servo signal from the phase comparator significantly differs from a classical error signal which is proportional to the difference between the reference value and the laser frequency. The output of the phase comparator is rather a time-integrated error signal. Differentiating the servo signal from the phase comparator thus results in a signal that is proportional to the deviation of the offset frequency to the reference. This can be used to compensate the drift of the reference cell of the MATISSE laser.
For that purpose a LabVIEW Virtual Instrumentation (VI) was implemented. A scheme of this stabilization loop is shown in Fig. 4.18. A beat note between the MATISSE Ti:Sa laser and a mode of the optical frequency comb is detected on a fast photo diode and fed into a digital phase detector. An RF signal serves as a reference. The output of the phase comparator is read into LabVIEW using a National Instruments DAQ card NI-6221. This signal (compare Fig. 4.17) is than derived by time to determine the deviation of the offset beat and the reference. According to the sign of the derivative the servo voltage will be increased or decreased by a fixed step size to compensate the drift of the cavity. The size of the steps can be defined by the user. A typical step size is $5 \cdot 10^{-6}$.
This simple locking scheme leads to statistical fluctuations around the reference value, because the step size is fixed. The quality and long-term stability was measured similarly to the long-term measurement of the stabilized diode laser. In this case the beat signal of the Ti:Sa laser with the frequency comb used for the stabilization can be directly used to evaluate the stability. A standard deviation of about 350 kHz was obtained. As will be shown in Section 4.6, this value can be improved by at least a factor of 10 if PID regulator is used. Furthermore, in Section 4.6 the more unstable dye laser version was used and hence, a much higher stability of a Ti:Sa laser is expected.
Avoiding the phase comparator would be one way to achieve an improved locking loop.

Table 4.3: Properties of the MATISSE TS laser measured in the laser lab while locked to the frequency comb. Note that the tuning range depends on the assembled mirror set and the pump power.

Characteristic	Value
Spatial mode	TEM00
Beam diameter	1.4 mm
Linewidth	55 kHz rms / 1 sec
Long-term stab.	350 kHz rms / 1 h
Intensity fluctuations	1% rms
Output power @ 782 nm	1.1 W / 7 W pump
	5 W / 18 W pump
Tuning range	740 - 870 nm @ 15 W pump

Due to the detection of the beat signal between the laser mode and a comb mode a simple frequency offset locking scheme with a frequency discriminator that converts the frequency difference in a DC voltage proportional to the deviation from a set value could be used. Some properties of the MATISSE laser when locked to the frequency comb are summarized in Tab. 4.3. Note, that the given value for the long-term stability is preliminary and will be improved with a direct frequency offset locking scheme by approximately a factor of 10. Another advantage of the software PID regulator becomes apparent considering that the lab PC is accessible via remote connection. During experiments at the TRIGA beamline each frequency selective element of the ring resonator can be tuned as well as frequency locked from any PC (or even smart phones) which is connected to the internet.

4.5.1 Frequency Doubling of the Ti:Sa Laser

Second- and Fourth-Harmonic Generation (SHG, FHG) allows to cover a considerable part of the UV and blue region of the spectrum to be covered with a Ti:Sa laser. In principle SHG with the Ti:Sa radiation produces light in the region from 350 to 500 nm and FHG would make the range from 200 nm to 250 nm available[2]. While frequency doubling is regularly used for collinear laser spectroscopy, frequency quadrupling has so-far not been applied. The reason is the considerable effort of setting up two frequency-doubling stages but also the limited amount of the second harmonic that is usually available for the second doubling step. At ISOLDE, spectroscopy in the $5s\ ^2\mathrm{S}_{1/2} \rightarrow\ 5p\ ^2\mathrm{P}_{3/2}$ transition of Cd^+ ions is planned at 215 nm. Two options were available for the production of this laser light: either a dye laser pumped with the UV light of an Ar-ion laser or frequency quadrupling of a Ti:Sa laser. The second option was realized in Mainz using the MATISSE TS laser, the Tekhnoscan FD-SF-07 and a Spectra Physics Wavetrain frequency doubler. Frequency

[2]Light below 200 nm can not be produced by SHG since all crystals become opaque for these wavelengths

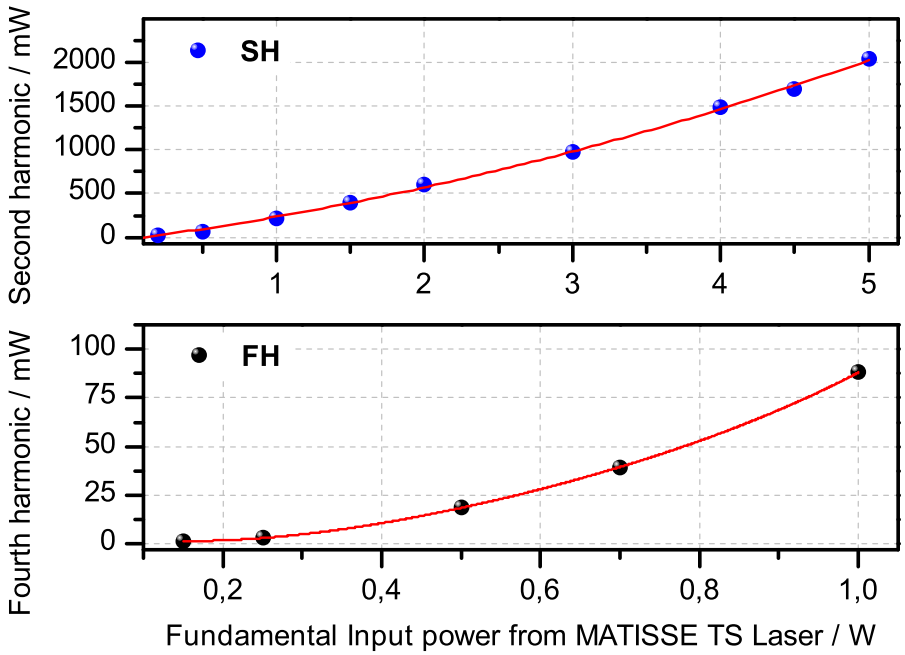

Figure 4.19: The upper graph shows the obtained output power in the second harmonic relative to the fundamental input power of the MATISSE TS and the lower graph the fourth harmonic output power relative to the fundamental input power.

doubling and quadrupling with the MATISSE was demonstrated and some results are shown in Fig. 4.19. The MATISSE was operated at 860 nm and an output power up to 4 W was obtained. The Tekhnoscan, equipped with a lithium triborate (LBO) non-linear crystal, was used as the first frequency doubler. A maximum conversion efficiency of 40% was reached with about 2 W of second-harmonic radiation. The cavity remained locked for hours without considerable losses in power. The amplitude noise is about 2% of the second harmonic output. Overall, this is to much power for spectroscopy but strongly facilitates the next doubling step. Therefore the elliptical output of the Theknoscan was shaped with cylindrical lenses and mode-matched into the Wavetrain cavity. For the second frequency doubling a beta barium borate (BBO) crystal was employed and the resulting power is also plotted as a function of the fundamental Ti:Sa power entering the first doubling stage in Fig. 4.19. The data points were fitted with a fourth-order polynom and the result fits the datapoints quite well. At the maximum power of the Ti:Sa, up to 100 mW at 215 nm were obtained, which is a conversion efficiency of the order of 2%. A photo of this setup is shown in Fig. 4.20. Stable operation for more than 5 hours without re-locking was demonstrated. The observed power fluctuations were below 3% in the fourth harmonic.
While the diode laser systems described so far could be operated in the reactor hall, this is not the case for the Ti:Sa laser due to safety reasons. Hence, the laser must be operated in the laser laboratory and the light guided with single-mode optical fibers into the reactor hall and to the beamline. Therefore one fiber for the infrared (Nufern 780 HP) and two

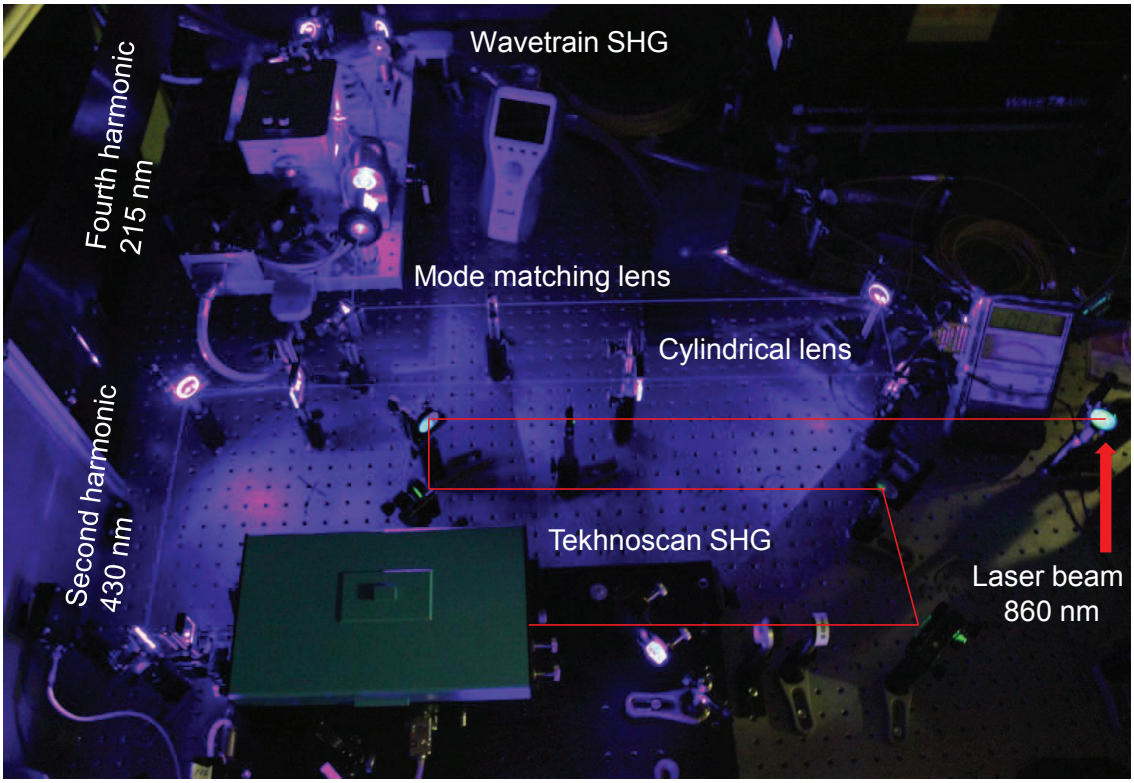

Figure 4.20: Photo of the frequency quadrupling setup. The MATISSE Ti:Sa laser (not shown here) was operated at 860 nm with an output power of 2 W. The IR beam (red) is mode matched to the cavity mode of a Tekhnoscan FD-SF-07 frequency doubler by two convex lenses. In this picture the second harmonic laser beam at 430 nm measured about 650 mW and is clearly visible. In total three cylindrical lenses were used to collimate x- and y-axis of the second-harmonic beam. Another convex lens was mode-matching the beam into a Spectra Physics Wavetrain frequency doubler. Up to 100 mW in the fourth harmonic at 215 nm were observed.

fibers for the visible - near-UV region (Nufern S405-HP) were installed to bridge gap of approximately 180 m between the laser and the beamline. In first tests a transmission of about 30 - 40 % was achieved using the UV fiber and more than 60% for the near IR fiber. It should be noted that the transmission strongly depends on the spatial mode profile and the beam shape and diameter should be adapted to obtain the desired TEM00 mode profile.

4.6 Frequency Stabilization of a MATISSE DS Laser

The last laser development concerns a MATISSE DS dye laser with absolute frequency stabilization for the BeTINa experiment (see Chapter 5). Previously, the old Coherent

699-21 dye lasers were used. Since they are 25 years old, the alignment screws show massive hysteresis and instabilities causing power drops and a quite difficult alignment procedure.
For the BeTINa experiment it is of utmost importance to avoid any long-term drift of the laser. Hence, the MATISSE DS was either stabilized to a molecular hyperfine transition or directly to the frequency comb.
The cavity of the MATISSE DS dye laser version matches exactly that of the Ti:Sa depicted in Fig. 4.16. Besides the replacement of the active medium *i.e.* the Ti:Sa crystal against a dye nozzle and the use of only a single focusing pump mirror, the slightly changed geometry of the setup needs an additional displacement rhomb which is inserted into the beam to close the cavity. Pumped with the 2^{nd} harmonic of a Nd:YAG or Nd:YVO_4 laser at 532 nm the MATISSE dye laser covers the optical wavelength range above 550 nm. Wavelengths below 550 nm can be produced using an Ar^+ pump laser operated at 355 nm or 488 nm.
The dye laser was operated at 626 nm with DCM solved in 2-Phenoxy-Ethanol (PE) and pumped with 8 W of a VERDI V8. More details are given in Chapter 5. The short-term linewidth settled somewhere about 150 kHz rms / 100 msec. As described in Section 4.5 for the Ti:Sa version, the MATISSE DS was also stabilized to a comb mode via the LabVIEW VI. The time evolution of the detected beat note at 30 MHz is shown in Fig. 4.21 (left). The standard deviation over a period of more than 2.5 h is about 550 kHz. The long-term excursions compared to the Ti:Sa setup is ascribed to fast fluctuations in the dye jet.
Frequency modulation (FM) saturation spectroscopy of the hyperfine structure in iodine as described in [Kri08] provides a classical error signal which can directly be used as an input signal for the LabVIEW based PID regulator.
A beat signal against the frequency comb was recorded over 4 h after locking the dye laser to iodine which is shown in Fig. 4.21 (right). The improvement is striking, the standard deviation for the long-term operation now decreased to 45 kHz. This value is very similar to what has been observed with the Coherent 699 dye lasers using a hardware PID regulator. For that reason the MATISSE DS laser was locked to the hyperfine transition of molecular iodine during the BeTINa experiment, while the second Coherent 699 dye laser was locked to the frequency comb.
In principle the MATISSE could also be stabilized by applying a servo signal to the reference cavity. However, the tries to do where in vain. The reason is a large amplification factor of about 50 that is applied to the external servo-signal fed into the control box. This factor can not be modified without soldering resistors on the circuit board of the servo loop electronics. The external input for the servo signal accepts an analog voltage between $0 - 3$ V. The latter corresponds to a frequency hub of about 100 GHz. Hence, a 1.5 mV signal applied to the external input will change the laser's frequency by at least 50 MHz. To achieve a control accuracy of 1 MHz, the PID regulator must regulate in voltage steps well below 0.01 mV. No hardware servo loop could be closed in order to lock the laser. As a last try the resistors on the circuit board were changed to decrease the amplification factor from 50 to 5. This corresponds to a voltage step width below 0.1 mV for a control accuracy of 1 MHz. Even with the modified circuit board all trials to lock the laser with

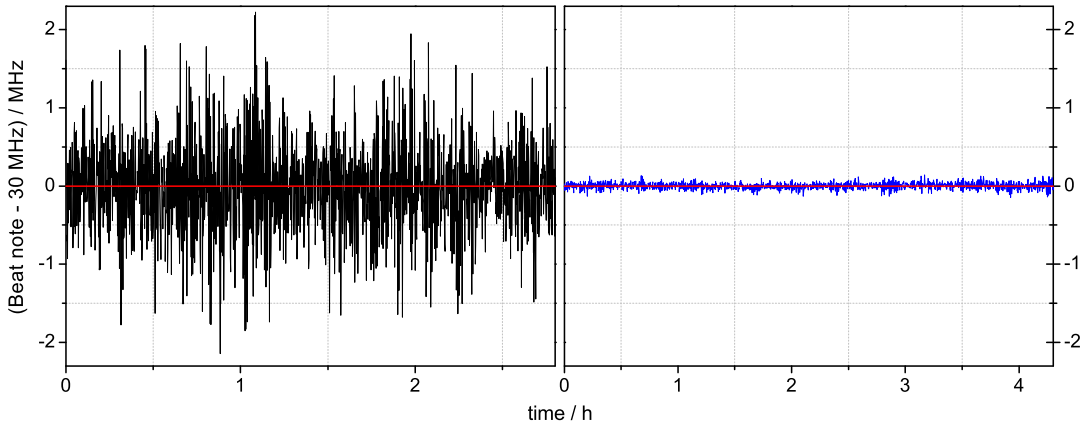

Figure 4.21: The MATISSE DS version externally stabilized to either a frequency comb (left) or to a molecular reference (right). It is obvious that a much higher precision was achieved when locking the dye laser to the molecular reference.

a hardware failed. In contrast, the resolution of the 16-bit DAC-Card of the MATISSE Controller is limited to $\frac{1}{2^{16}} = 0.000015 = 0.015$ mV which is the smallest possible voltage step width. Hence, using the LabVIEW PID regulator the MATISSE laser can be locked quite well. Furthermore, the reached stability well below 100 kHz is for most of the laser spectroscopic experiments sufficient and offers remote control of the laser's frequency.

5 The BeTINa Experiment

The determination of the charge radius of the lightest elements requires a very accurate isotope shift measurement and atomic mass-shift calculations with spectroscopic accuracy, as discussed in the theory section 2.5. Isotope shift measurements of $^{7,9,10,11}Be^{+}$ were performed in 2008 in combined collinear and anticollinear spectroscopy using a complex frequency comb based laser system. But at that time measurements on ^{12}Be were not feasible, because the method was not able to cope with the low production rate of ^{12}Be, which was three orders of magnitude lower than that of ^{11}Be. Within this work, ion bunching and cooling with ISCOOL has been tested and a photon-ion coincidence technique was implemented at COLLAPS. This lead to a significantly increased detection efficiency and allowed the measurement of ^{12}Be. Moreover, the laser system was modified and partly replaced by a state-of-the-art MATISSE dye laser. In the framework of the laser developments for TRIGA-LASER this MATISSE dye laser could be characterized and different locking schemes investigated. One of the stabilization setups is currently in use for the MATISSE Titanium Sapphire version in Mainz.
The change of the rms nuclear charge radius, is calculated as the difference between the optical isotope shift measurement and the theoretical mass shift calculation, divided by the field shift constant C[1] (see Eq. 2.22). The latter indicates the sensitivity of the transition to the change in the rms nuclear charge radius. For the $2s \rightarrow 2p$-transition in lithium the corresponding field shift factor is $C_{\mathrm{Li}}^{2s\rightarrow 2p} = -2.4565$ MHz/fm^2 whereas for beryllium it amounts to $C_{\mathrm{Be}}^{2s\rightarrow 2p} = -16.9$ MHz/fm^2. Since in both cases simple $2s \rightarrow 2p$-transitions are taken into account, the increase can be explained by the fact that the valence electron in the beryllium ions is more tightly bound and has a larger probability for diving into the nucleus. Therefore, the factor C_{Be} basically determines the required precision of the laser spectroscopic measurements. Hence, compared to the cases of He and Li the requirements are slightly relaxed. An estimation can be carried out using a Gaussian error propagation based on Eq. 2.22 which leads to

$$\Delta r_c^A = \frac{1}{2r_c^A}\sqrt{(2r_c^9\Delta r_c^9)^2 + \left(\frac{\Delta\delta\nu_{FE}^{A,A'}}{F}\right)^2} \tag{5.1}$$

To obtain a relative accuracy better than 1% for the nuclear charge radius, the isotope shift measurement must be performed with an absolute accuracy of about 1.6 MHz.
The differential Doppler shift, *i.e.* the Doppler Shift in frequency for a 1 V change of the

[1] It should be noted that for the lithium measurements [Ewa04, San06, Noe11] the $2s \rightarrow 3s$ two-photon transition was used with an even smaller field shift factor of $C_{\mathrm{Li}}^{2s\rightarrow 3p} = -1.51$ MHz/fm^2.

ion beam energy is given by

$$\delta\nu_{\mathrm{diff}} = \frac{\partial\delta\nu_D}{\partial\delta U} = \frac{\nu_0}{mc^2}\left(e + \frac{e\left(mc^2+eU\right)}{\sqrt{eU\left(2mc^2+eU\right)}}\right). \tag{5.2}$$

At 30 keV $\delta\nu_{\mathrm{diff}}$ differs significantly for ^{12}Be and ^{11}Be with

$$\delta\nu_{\mathrm{diff}}^{^{12}\mathrm{Be}} = 31\ \mathrm{MHz/V} \tag{5.3}$$

$$\delta\nu_{\mathrm{diff}}^{^{11}\mathrm{Be}} = 29\ \mathrm{MHz/V}. \tag{5.4}$$

Thus, an uncertainty δU in the voltage measurement leads to an artificial isotope shift of $\Delta\left(\delta\nu_{\mathrm{IS}}^{11,12}\right) = \left(\delta\nu_{\mathrm{diff}}^{^{12}\mathrm{Be}} - \delta\nu_{\mathrm{diff}}^{^{11}\mathrm{Be}}\right)\cdot\delta U \approx 6$ MHz. Consequently, the acceleration voltage would have to be measured to a relative precision of $10^{-5} - 10^{-6}$ to ensure the required accuracy. However, this is not feasible at ISOLDE, even though high-voltage dividers with a relative accuracy of 1 ppm exist [Tue09] and have been applied at ISOLDE [Kri11]. Measuring the applied voltage does not result in the same accuracy for the ion beam energy since additional uncertainties in the starting potential of the ions inside the resistively heated crucible must be taken into account. This will be further discussed in the next chapter. For the beryllium measurements, a different approach was chosen. The combination of superimposing a collinear and an anticollinear laser beam with the ion beam allowed to overcome the precise determination of the applied high voltage. Without the knowledge of the ion beam's absolute velocity β the transition rest-frame frequency ν_0 can be deduced from absolute frequency measurements of the collinear ν_c and anticollinear ν_{ac} lasers according to

$$\nu_c = \nu_0\cdot\gamma(1+\beta) \tag{5.5}$$

$$\nu_{ac} = \nu_0\cdot\gamma(1-\beta) \tag{5.6}$$

$$\nu_0^2 = \nu_c\cdot\nu_{ac}. \tag{5.7}$$

However, it must be highlighted that Eq.5.7 remains valid only if the absolute laser frequencies are determined simultaneously for exactly the same ion velocity β.

5.1 Production of Beryllium Isotopes at ISOLDE

As described in Section 3.2, the radioactive beryllium isotopes were produced by impinging a 1.4 GeV pulsed proton beam onto a thick uranium carbide target. Due to the large ionization potential of beryllium of about 9.4 eV the resonance ionization laser ion source RILIS [Fed08] was used to efficiently ionize the beryllium isotopes. A two-photon resonant ionization process into an auto ionizing state was applied. As depicted in Fig. 5.1 a pulsed frequency-doubled dye laser operated at 234.9 nm excites an electron from the $2s^2\ ^1\mathrm{S}_0$

ground state into the $2s2p\ ^1P_1$ excited state. A second dye laser was operated at 297.3 nm to pump into the $2p^2\ ^1S_0$ auto-ionizing state. For that purpose, new Sirah Cobra pulsed dye lasers were used. An efficiency of about 7% was reached. The RILIS offers a very high beam purity and a much smaller energy distribution compared to a plasma source, which would have been the only alternative. As listed in Tab. 3.1 the ion beam intensity decreases from ^{11}Be to ^{12}Be by at least three orders of magnitude. Even though ^{12}Be is a spin zero nucleus and, thus, does not exhibit a hyperfine structure, a beam intensity of about 1000 ions/s is not sufficient to perform classical collinear laser spectroscopy solely based on fluorescence detection. Therefore the pulse structure and cleanliness of the delivered ^{12}Be was employed to suppress background events as discussed below.

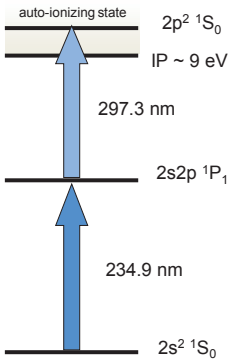

Figure 5.1: Resonant laser ionization scheme for beryllium atoms.

5.2 Beryllium Ion Beam Structure

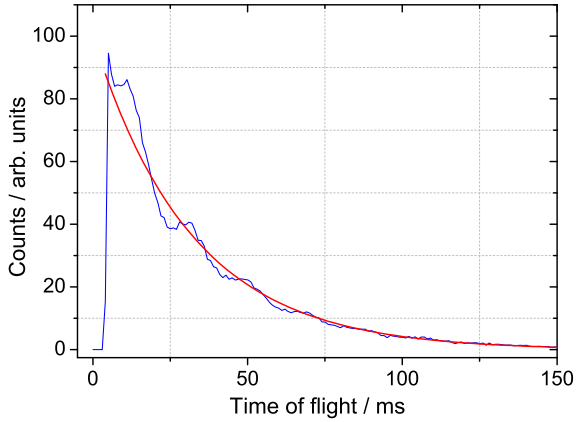

Figure 5.2: Release curve (blue) of beryllium ions from the ISOLDE ion source RILIS measured with a secondary electron multiplier in the COLLAPS beamline. An exponential decay curve (red) is fitted to the release curve which was integrated over 100 proton pulses with a resolution of 0.2 ms/channel.

Pulses of about $3 \cdot 10^{13}$ protons were applied to the UC_x target. The average time between two proton pulses was about 4 s. Since the half-life of ^{12}Be is 21.50(4)ms [Aud97], it is expected that the release of ^{12}Be ions will last for only a few 10 ms after each pulse. Hence, a release curve of resonantly ionized ^{12}Be atoms was recorded with a secondary electron multiplier that was installed at the end of the COLLAPS beamline. Ion events were fed into a multi-channel analyzer triggered by the proton pulse and the result is plotted in Fig. 5.2. The release curve was integrated over 100 proton pulses with a resolution of 0.2 ms/channel. The integrated area under the release curve is 1 200 000 counts which corresponds to a total release of 12 000 ions/pulse. The maximum amount observed during the beamtime was about 15 000 ions/pulse, while a typical value was about 8 000 /pulse. About 2-3 ms after the proton pulse the first

ions appear at the beamline[2]. This delay is not determined by the time of flight of the ions, which is of the order of about 20 μs, but rather by the recovery-time of the high-voltage at the ion source after the proton pulse. The ISOLDE HV is pulsed down before the proton pulse impinges on the target to reduce the load on the high-voltage supplies. This is discussed in detail in [Kri11] (see appendix). After the initial steep rise a roughly exponential decay is observed. The red line is an exponential fit to the decay curve and results in a half-life of $T_{1/2} \approx 21.9(8)$ ms being in excellent agreement with the literature value of 21.50(4)ms [Aud97]. At mass 12 practically no isobaric contamination was observed, which is reflected by the fact that the release curve asymptotically approaches zero. This was expected since all mass-12 isobars $\left({}^{12}\mathrm{C}, {}^{12}\mathrm{B}, ..\right)$ cannot be surface ionized and will also not be resonant with the RILIS lasers. These are excellent conditions for the application of a photon-ion coincidence technique, since random coincidences between scattered light and isobaric ions are practically absent. It has to be mentioned that fluctuations in the proton beam intensity and repetition rate strongly influence the time structure of the ion beam. Since the target is mainly heated due to the proton impact, a variation in the pulse distance significantly changes the diffusion time out of the target and therefore the number of Be ions delivered to COLLAPS beamline after the pulse. Thus, a normalizing procedure is required which is naturally provided by the ion-photon coincidence signal as discussed below.

5.3 Cooling and Bunching of Be Ions

Since the production rate of ^{12}Be is rather low, the sensitivity of the collinear spectroscopy measurement must be increased in order to achieve spectra in a reasonable time interval (several hours). A common way to do this is the usage of a cooler and buncher as it is now also available at ISOLDE. A test beamtime investigating ^{9}Be using bunched beams from ISCOOL[3] was performed at ISOLDE. However, the transmission of the ions through the buncher was measured to be 5%. Most of the operational cooler and buncher devices include helium as a cheap and non-in flammable buffer gas. This is also true for ISCOOL. But the helium-beryllium mass difference is quite small. Hence, the loss of 95% of the beryllium ions is ascribed to this scattering processes with the He atoms. As a result the bunch would include only 250 of the 5000 ions. For that reason the usage of the ISCOOL device in collinear spectroscopy of beryllium ions was abondomded. However, at TRIUMF it was demonstrated that cooling and bunching is possible even for the 8 ms isotope ^{11}Li, if hydrogen is used as a buffer gas [Smi08].
Due to the unsuccessful attempts with cooling and bunching, the sensitivity of collinear laser spectroscopy had to be increased using a different technique. The isobarically pure ion beam offered the possibility to use the ion-photon coincidence technique. Therefore

[2] The first release curves recorded during the beamtime showed a slow rise on the ion signal only after about 20 ms. This was caused by a defect of the high-voltage supply and resulted in a drop of the release efficiency of more than a factor of 2. The high voltage platform was switched to the second HV-supply which did not show this behavior.

[3] ISolde COOLer and buncher

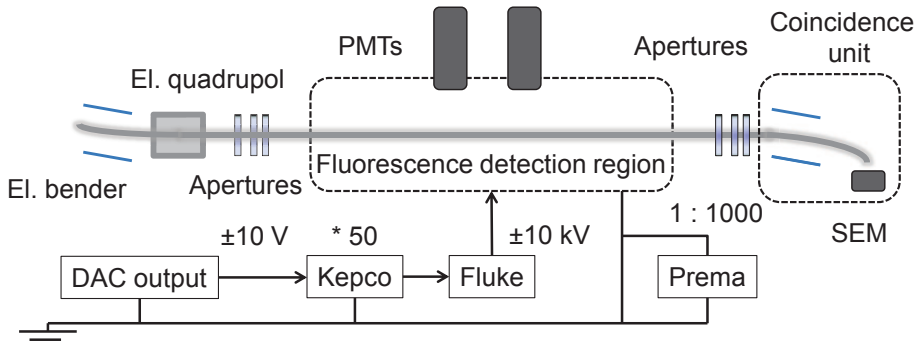

Figure 5.3: Schematics of the COLLAPS beamline and its high-voltage power supplies. A 10° electrostatic deflector guides the ion beam to the center of the beamline. An electric quadrupole collimates the beam through the apparatus. The deflector housing of the fluorescence detection unit is floated on a high voltage to provide the Doppler-tuning voltage (details explained in the text). The individual ions are detected using a secondary electron multiplier (SEM) behind the fluorescence detection.

a secondary electron multiplier (SEM) was installed after the fluorescence detection for single-ion detection as depicted in Fig. 5.3. The complete coincidence unit consists of a SEM with an amplification of $\approx 10^8$, a pulse shaping amplifier followed by discriminator, and the coincidence electronics.

5.4 The COLLAPS Beamline

The collinear spectroscopy beamline was commissioned at the ISOLDE facility in the early Eighties [Neu81] and continuously improved. Developments were focused on the fluorescence detection region, but also a photon-particle coincidence unit was developed. Meanwhile, a cooler and buncher ISCOOL is available at ISOLDE to compensate the lower yields of exotic isotopes and has been used for spectroscopy on copper [Fla11] and Ga isotopes [Man11b]. The current configuration of the COLLAPS fluorescence detection region (FDR) is similar to the one at TRIGA-SPEC as shown in Fig. 5.3. Modifications for the BeTINa experiment are discussed in detail in the following sections. Here, details of the electronic setup used for Doppler-tuning as shown in Fig. 5.3 are briefly explained. A 16 bit DAC card controlled by the data acquisition program delivers a DC voltage between ±10 V. This is fed into an amplifier device (Kepco BOP 500M) which amplifies the input signal with a fixed factor of about 50. The obtained voltage of ±500 V is the available scan voltage U_{scan}. If an isotopic chain is measured it is convenient to apply an additional offset voltage to the fluorescence detection region. Then the laser frequency can be kept constant for each isotope. Therefore a Fluke power supply (Fluke 410B) is used to generate an offset voltage U_{offset} up to ±10000 V. The final voltage applied to the fluorescence detection region is $U_{\mathrm{det}} = U_{\mathrm{scan}} + U_{\mathrm{offset}}$. During a scan U_{det} is directy measured by a high voltage divider (Julie Research 1:1000) connected to a digital voltmeter

(Prema). In this configuration a relative accuracy for the voltage of 10^{-4} is reached. As discussed above this accuracy is not sufficient for the spectroscopy of the very light species like beryllium.

5.5 Setup and Specification of the frequency comb Based Laser System

The hyperfine structure of the beryllium isotopes in the $2s\ ^2\mathrm{S}_{1/2} \rightarrow 2p\ ^2\mathrm{P}_{1/2}$ D1-transition and $2s\ ^2\mathrm{S}_{1/2} \rightarrow 2p\ ^2\mathrm{P}_{3/2}$ D2-transition is depicted in Fig. 2.7. The transition wavelength in the rest frame is about 313 nm and depending on the hyperfine structure splitting either one, three or four peaks are observable. The laser system that was installed at COLLAPS for the BeTINa experiment is depicted in Fig. 5.4. For anticollinear excitation a frequency doubled Nd:YVO_4 laser (Verdi V18) was operated at 9 Watts to pump a Coherent 699 dye laser. The dye solution was prepared solving Sulforhodamin B (1.75 g/l) in ethylen glycol with a small amount of methanol. The dye circulator was running at 8 bars and cooled to 12°C. With a fresh load of dye up to 900 mW output power was achieved. The power decreased continuously during the first two hours before it stabilized at about 700 mW for several hours. The second Coherent 699 dye laser used during the first run of the BeTINa experiment was replaced by a Sirah MATISSE DS dye laser as described in the previous chapter. In this case, DCM dissolved in 2-Phenoxy-Ethanol (1.35 g/l) served as the dye solution. The dye circulator cooled the solution to 12°C and pumped it with 16 bars through the dye nozzle. Another Verdi (V8) provided about 8 Watts for pumping. In this configuration we achieved an output power of about 1.2 Watts. To obtain the 313 nm a four mirror bow-tie configuration (Tekhnoscan FD-SF-07) second harmonic generator (SHG) was used for the collinear laser, while the anticollinear laser beam was frequency doubled in a two-mirror delta cavity (Spectra Physics Wavetrain). Due to the limited space in the laser lab, the frequency doublers were placed next to the beamline. Two 25 meter long large mode-area (LMA-20) fibers guided the fundamental output of the dye lasers into the ISOLDE hall to the COLLAPS beamline. The coupling efficiency for the collinear laser was about 60% and for the anticollinear laser 70%. Several lenses and an optical isolator caused further losses and about 600 mW entered the Tekhnoscan frequency doubler and 450 mW the Wavetrain SHG. In both cavities BBO crystals converted the fundamental wavelength to 20 mW and 8 mW, respectively. The elliptical output beam was shaphed using cylindrical lenses to a round collimated beam with 4 mm diameter. Several mirrors guided both UV beams into the COLLAPS beamline where they were carefully superimposed with the help of two irises over a distance of 3 meters. A collinear and anticollinear remote controlled beam shutter were installed to block laser beam before entering the beamline.

An especially important aspect of the laser system is the precise frequency stabilization of both dye lasers. In contrast to ordinary collinear spectroscopy, the BeTINa experiment requires a well-known absolute frequency of the lasers. Therefore, a small fraction (30 mW) of the MATISSE main beam was fiber coupled into a frequency-modulated saturation

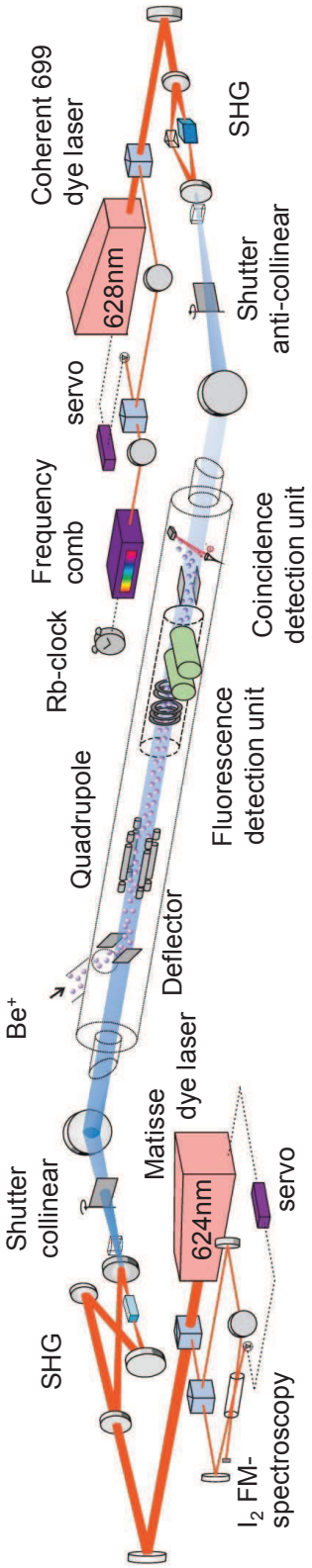

Figure 5.4: Experimental setup for the BeTINa project at ISOLDE. Two frequency-doubled dye lasers were used to drive the $2s\ ^2\mathrm{S}_{1/2} \rightarrow 2p\ ^2\mathrm{P}_{1/2,3/2}$ transitions in beryllium. The dye laser operated for excitation in collinear geometry (624 nm) was stabilized to a hyperfine transition of molecular iodine and the servo loop splices the error signal to the tuning elements of the dye laser. The output is coupled into a second harmonic generator and the UV light at 312 nm guided by mirrors into the beamline if it is not blocked by the collinear beam shutter. Similar to that, the second dye laser is directly locked to the frequency comb where an atomic clock serves as a reference. After frequency doubling to 314 nm the UV light passes the beamline anticollinearly to the ion beam if the anticollinear beam shutter is open. The laser beams are superimposed with the beryllium ion beam which is deflected by electrostatic deflector pair. The resonance fluorescence is detected in the fluorescence detection unit. Which is followed by the installed photon-ion coincidence detection unit.

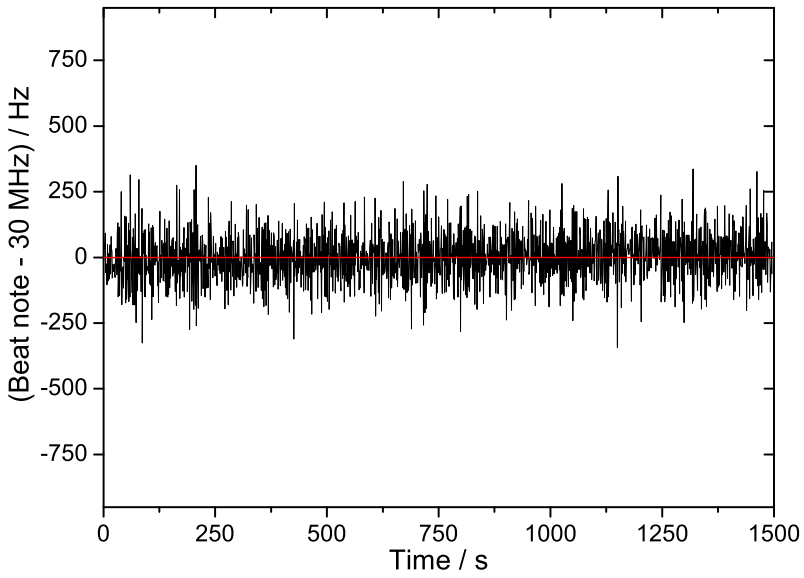

Figure 5.5: long-term drift of the Coherent 699-21 dye laser locked to a frequency comb. Each data point represents the beat signal averaged over 1s. A standard deviation of $\sigma = 196$ Hz is observed.

spectroscopy setup [Kri08]. Scanning the laser's frequency across the well-known hyperfine structure of molecular iodine $^{127}I_2$ delivered dispersion signals (suitable for locking a laser) due to the phase sensitive detection. In total 12 transitions in iodine are suitable for frequency locking the collinear laser close to the desired Doppler shifted frequency depending on the applied acceleration voltage between 30 - 60 kV. The demodulated servo signal was fed into a 16-bit DAQ card (NI 6221) and processed in the MATISSE control software that includes a PID regulator programmed in Labview. It generates a servo signal that is sent via a USB connection back to the MATISSE control box. The latter splits the signal into a low frequency and a high frequency part which are delivered to the low-bandwidth (200 Hz) tuning mirror and the high bandwidth (several MHz) tweeter mirror, respectively. In this way the MATISSE laser was stabilized with high accuracy and a long-term drift avoided. The long-term stability was measured by beating the frequency-stabilized MATISSE dye laser against the FC 1500 frequency comb (Menlo systems). The result is shown in Fig. 4.21 and exhibits a standard deviation over 4 hours of about 45 kHz.
The second dye laser, a Coherent 699-21, was directly stabilized to the frequency comb via the digital phase-lock as described in Chapter 4.6. A fast photo diode detects the beat signal between a comb mode and the Coherent 699 dye laser. A sensitive phase comparator (Menlo systems - DXD100) detects the phase difference between the beat signal and a reference signal. In this case a 10 MHz RF reference from a Rb atomic clock serves as the reference. The clock is long-term stabilized against a 1-s GPS signal provided by a GPS receiver. A fast PI regulator (Menlo systems - PIC 210) generates a servo signal that is fed into the control box of the dye laser to keep the phase constant. This phase lock loop stabilizes the dye laser accurately to any chosen frequency. The long-term stability

was measured detecting a beat signal against the frequency comb. The result is shown in Fig. 5.5. The standard deviation over 1500 seconds is about 200 Hz.
To determine the isotope shift of the beryllium isotopes, the absolute frequency of the dye lasers must be known. To determine the frequency of the iodine-stabilized MATISSE laser, a beat signal with the frequency comb was recorded for several hundreds of seconds. From this the absolute laser frequency ω_L is calculated according to

$$\omega_L = n\omega_{\text{rep}} \pm \omega_{\text{ceo}} \pm \omega_{\text{beat}}, \tag{5.8}$$

where ω_{rep} denotes the repetition rate of the frequency comb, n the mode number of the frequency comb mode nearest in frequency to the single-mode dye laser and ω_{ceo} the carrier envelope offset frequency. The (comb) mode number is calculated from a wavelength measurement using a High Finesse WS7 wavemeter accurate to about 50 MHz, which is only half of the repetition rate of the frequency comb. The repetition rate is set manually at an RF generator close to 100 MHz. The beat signal frequency ω_{beat} is taken as the mean value of the beat measurement. Its sign can be determined by changing the repetition frequency of the comb slightly. Decreasing the repetition frequency will reduce the beat frequency if the laser frequency is smaller than the closest comb mode $(-)\omega_{\text{beat}}$ and increase the beat signal if the laser frequency is above the closest comb mode $(+)\omega_{\text{beat}}$. Increasing the repetition rate will lead to the opposite effect. The same holds for the sign of the offset frequency ω_{ceo}. In this case the pump laser power of the frequency comb has to be changed. Note that the offset frequency ω_{ceo} itself is stabilized to 20 MHz during each measurement, but due to the frequency doubling a value of $\omega_{\text{ceo}} = 40$ MHz has to be used. These measurements are described in detail in [Kri08]. For a chosen subset of lines, required for the measurements of ^{12}Be, the measurements were repeated with the MATISSE laser and results are listed in Tab. 5.1. A major change compared to the old setup is that the rubidium clock (Stanford Research Systems PRS10) serving as a reference for the frequency comb was now locked via a GPS antenna to the time standard. In 2008 [Kri08] all absolute frequencies determined during the BeTINa experiment were afflicted with a total uncertainty of 580 kHz dominated by the uncertainty of the Rb-clock contributing with 410 kHz. The remaining part of 170 kHz was due to the reproducibility of the locking point over several months. The Rb-clock uncertainty was estimated from the manufacturer's specification of the fractional uncertainty caused by an "aging-drift" of up to $5 \cdot 10^{-10}$/year, additional to the $5 \cdot 10^{-11}$ uncertainty after calibration. During the 2008 measurements the last calibration was several months ago and thus caused the relatively large uncertainty. The GPS tracking eliminates this uncertainty and calibrates the atomic clock to the GPS time standard, which decreased the uncertainty from 410 kHz to 19 kHz. The average deviation for the iodine frequencies between the 2008 and 2010 measurements is less than 200 kHz which indicates that the systemaitc uncertainty was probably overestimated.
One very important point should be noted: In the BeTINa experiment the lasers were stabilized in their fundamental frequencies, but spectroscopy of the transitions in beryllium required the second harmonic of the laser frequencies. In that case the errors are correlated and therefore the uncertainty of 19 kHz fully propagates to 38 kHz for the ab-

Table 5.1: Absolute frequencies of the a1 hyperfine transition in molecular iodine measured during the BeTINa experiment. The uncertainty of all experimentally determined frequencies is 190 kHz dominated by the part of 170 kHz due to the reproducibility of the locking point over several months, whereas the calculated frequencies are afflicted with an uncertainty of 3 MHz [Kno04].

Iodine line No.	a1 HFS transition	Frequency (theory) / MHz	Frequency (experiment) / MHz	Deviation /MHz
1	R(62)(8-3)	479 804 454.67	479 804 355.09	-0.42
2	R(70)(10-4)	479 823 072.75	479 823 072.58	0.17
3	P(64)(10-4)	479 835 709.4	479 835 708.96	0.44
4	R(60)(8-3)	479 870 011.92	479 870 012.2	0.35
5	R(58)(8-3)	479 933 416.07	479 933 416.36	-0.29
6	R(56)(8-3)	479 994 568.08	479 994 568.11	-0.03
7	R(54)(8-3)	480 053 468.95	480 053 469.06	-0.11
8	R(52)(8-3)	480 110 119.57	480 110 119.59	-0.02
9	R(50)(8-3)	480 266 578.9	480 266 578.59	0.31
10	R(48)(8-3)	480 314 237.19	480 314 236.83	0.36
11	R(42)(8-3)	480 359 649.42	480 359 649.13	0.29
12	R(40)(8-3)	480 402 816.3	480 402 815.78	0.52

solute frequency of the Be^+ transition. This is, however, a reduction to about 5% of the previous uncertainty of 820 kHz. It must be stressed that the additional uncertainty of the measured iodine frequency (170 kHz) only has to be taken into account if the values are to be compared with calculations of the iodine frequency or are being used to extract hyperfine parameters. For the purpose of the BeTINa experiment, the locked laser frequency was directly measured during the beamtime and it is not important whether this indeed agrees with the exact iodine transition frequency.

5.5.1 Measurement Procedure

The collinear dye laser (MATISSE DS) was stabilized in frequency to a particular hyperfine transition of iodine as listed in Tab. 5.1 depending on the beryllium isotope and the total acceleration voltage U_{tot}. Usually, about 3-4 iodine lines were suitable for each isotope for a fixed ISOLDE acceleration voltage, the range being limited by the ± 10 kV reacceleration voltage applicable at the fluorescence detection region. For example, if the acceleration voltage is set to $U_{\mathrm{tot}} = 40\,000$ V and $^9Be^+$ is the ion of interest, the iodine lines No. 5,6,7,8 are suitable to cover the complete hyperfine structure. The highly accurate mass shift calculations in combination with the absolute frequency of the D1 and D2 transitions for the reference isotope ^{9}Be allow to calculate the frequency of the center of mass position for all isotopes within a few MHz accuracy. Thus, it is possible to calculate exactly at which

Table 5.2: Locking frequencies of the dye lasers and the collinear and anticollinear resonance position as the center of gravity. If the collinear laser is stabilized to iodine line No. 6 from Tab. 5.1 all isotopes of interest ^{9,10,11,12}Be can be investigated changing the anticollinear laser frequency and the offset voltage, respectively.

	^{9}Be^{+}	^{10}Be^{+}	^{11}Be^{+}	^{12}Be^{+}
iodine line ν_{I_2} /MHz	959 989 128.2	959 989 128.2	959 989 128.2	959 989 128.2
laser locked ν_{699} /MHz	954 418 029.7	954 452 802.8	954 480 138.1	954 504 812.3
transition ν_0 /MHz	957 199 652.5	957 216 962.9	957 231 212.5	957 243 042.6
post acceleration /V	4 500	1 000	-2 500	-6 000
collinear cg /V	35 541	39 001	42 486.8	45 964.7
& anticollinear cg				

frequency the anticollinear laser (Coherent 699) has to be locked to observe the center of gravity at the same acceleration voltage.
The direct lock to the frequency comb has the advantage that by choosing the right repetition rate of the comb the dye laser can be locked at exactly the right frequency.
Table 5.2 shows an example using the iodine line No. 6 at a total acceleration voltage of 40 kV at ISOLDE. Using the known transition frequency ν_0 of ^{9}Be, the post-acceleration voltage can be determined at which the resonance appears

$$U_{\mathrm{pos}} = \frac{(\gamma - 1) \cdot M\left(^{9}\mathrm{Be}\right) \cdot c^2}{e}. \tag{5.9}$$

If this Doppler tuning is applied, the anticollinear laser is also at resonance if it is stabilized at $\nu_{ac} = 954\ 418\ 029.7$ MHz. In this way both spectra in collinear and anticollinear geometry could be recorded by Doppler-tuning simultaneously without changing the scanning range. After having both lasers set to the well defined frequencies the frequency doublers were locked and the second harmonic beams superimposed with each other and with the ion beam. This was enforced by a pair of irises located in the beamline. Shutters placed in front of the viewports of the COLLAPS beamline are controlled by the data acquisition system. As soon as a scan was started the data acquisition software MCP (synchronized to the proton pulse) opened the collinear shutter. The Doppler-tuning voltage was scanned with a dwell time of 22 ms per voltage step and the scan range was divided into 200 - 800 channels depending on the hyperfine splitting of the respective isotope. Reaching the last channel, the collinear shutter was closed and the anticollinear shutter opened and an anticollinear scan was performed. A spectrum is the sum over 50 - 200 single scans for each direction. Depending on the yield of the isotope, recording a spectrum took about 3 minutes for ^{10}Be, 10 minutes for ^{9}Be and 30 minutes for ^{11}Be. In case of ^{12}Be this scanning procedure was slightly changed: Data was only taken for 60 ms after the proton pulse then the shutters were switched from the collinear to the anticollinear configuration and the next proton pulse was used for the anticollinear spectrum. Before the next pulse,

the Doppler-tuning voltage was changed and the shutters switched again to the collinear configuration. A scan of ^{12}Be is a sequence of 20 data points. A spectra was thus obtained by integrating over 200 - 400 scans which took about 2 - 4 hours. Therefore, with such a scanning procedure, spectra in both geometries were recorded quasi simultaneously for all isotopes which eliminates any fluctuations in the acceleration voltage by averaging.

5.6 Lineshape Studies of ^{9}Be and ^{10}Be

Both isotopes ^{9}Be and ^{10}Be served as a reference during the beamtime. The advantage of ^{10}Be is the absence of hyperfine structure. This makes it ideal as a reference for the other even isotope ^{12}Be for two reasons: The scanning time is strongly reduced compared to the large hyperfine structure of ^{9}Be and both isotopes should experience similar recoil effects since both provide a closed two-level system without dark pumping. This will be discussed in detail below.
Reference spectra of ^{9}Be as well as of ^{10}Be were studied and compared to the spectra from 2008 during a first test beamtime in 2010 and the coincidence unit was commissioned.
Figure 5.6 depicts the optical hyperfine spectra of the D1 transition in ^{9}Be^{+} for collinear (left) and anticollinear excitation (right). The count rate is plotted versus the scanned frequency range calculated by multiplying the Doppler-tuning voltage with the differential Doppler factor[4]. The acceleration voltage U_{ISOLDE} was 35 kV and the spectra are obtained taking the integral of 20 individual scans at an ion beam current of about 430 pA. The laser power was attenuated to 3 mW in both directions with a beam diameter of approximately 3-4 mm. A multiple Voigt profile with 8 peaks (red line) is fitted to the data points. Each of the resolved four hyperfine transitions, shows a small satellite peak on its left. This peak was already observed in the first BeTINa run and is separated from the corresponding main peak by almost exactly 4 V. Comparing the collinear and anticollinear spectra it is obvious that these satellite peaks always occur on the low-energy tail in the Doppler-tuned spectrum. Since the satellite does not occur as a "mirror image" in the right part of the figure and its distance is independent from the acceleration voltage - which means that the frequency separation from the main peak depends on the acceleration voltage - it becomes clear that it must be a kinematic effect. The satellite peaks represent a "ghost" image of the real spectrum shifted by 4 V, hence it must occur from the interaction of the laser with ions that have lost 4 eV of kinetic energy and, thus, require additional acceleration to become resonant with the laser frequency. The energy loss of 4 eV can be explained by collisional excitation of the 2s $\rightarrow$ 2p transition. If the ion is excited to the $2p$ state in an inelastic collision with a residual gas atom, the energy required for the excitation (4.03 eV) is taken from the ions kinetic energy. The photon is afterwards emitted and the energy is lost.
At a typical pressure of 10^{-6} mbar inside the beamline, the particle density at room

[4]For fitting, the voltage scale was converted to frequency point by point and thus the small deviation between the linear approximation and the real voltage to frequency relation was taken into account.

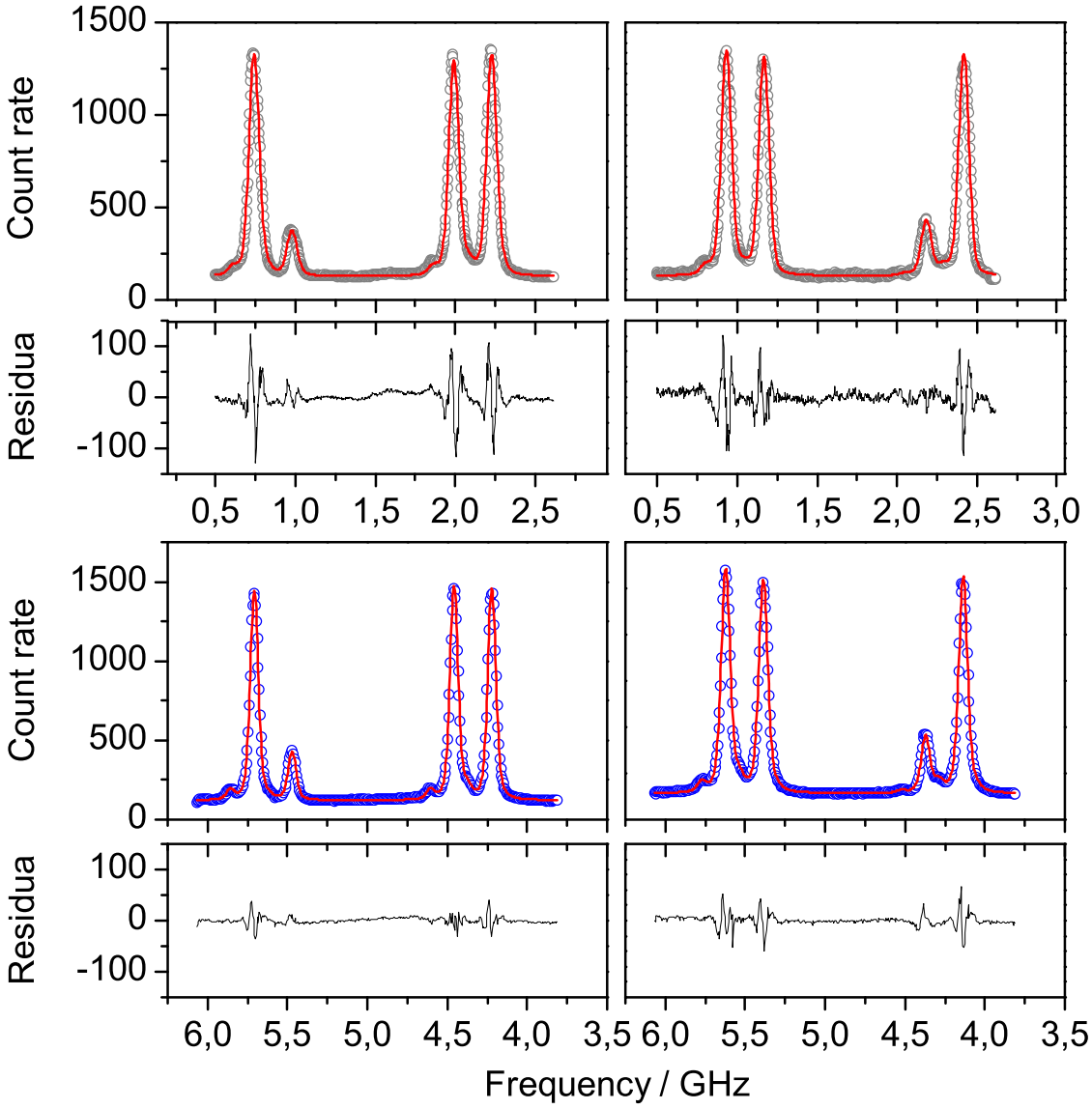

Figure 5.6: Optical hyperfine spectra of the $2s\ ^2S_{1/2} \rightarrow 2p\ ^2P_{1/2}$ transition in $^9Be^+$ for collinear (left) and anticollinear excitation (right). The lower spectra were taken at 35 kV ISOLDE voltage and are the sum of 20 individual scans with a resolution of 400 channels in 2010 whereas the upper spectra were taken in 2008 at 50 kV and are the sum of 50 individual scans with a resolution of 800 channels. The spectra are fitted with a multiple Voigt profile (red line). It is striking that the linewidth is significantly smaller in the 2010 beamtime even though this effect is partially covered by the smaller differential Doppler shift at 50 kV (39.5 MHz/V at 35 kV and 33 MHz/V at 50 kV).

temperature is about

$$n = \frac{N}{V} = \frac{p}{k_B \cdot T} \approx \frac{10^{-6} \cdot 100}{1/40 \cdot 10^{-19} \cdot 16} \frac{\mathrm{N}}{\mathrm{m^2 Nm}} \approx 2.5 \cdot 10^{16} \frac{1}{\mathrm{m^3}}. \tag{5.10}$$

Using the expression $\bar{\lambda} = \frac{1}{n\sigma}$ for the mean free-path and the geometrical cross section $\sigma = \pi r^2$ with $r \approx 10^{-10}$ m, we obtain for the excitation probability along $l = 20$ m of beamline $P = l/\bar{\lambda} = l \cdot n \cdot \sigma = 20 \cdot 2.5 \cdot 10^{12} \cdot 3 \cdot 10^{-16} \approx 1.5\%$.
The intensity ratio of the main peak and the ghost in Fig. 5.6 is about 5% for the very left peak, which is in reasonable agreement with the calculation considering that the pressure is only roughly estimated and might be considerably higher in the source region.
An additional slight asymmetry at higher energies is observed in the 2008 spectra of Fig. 5.6 (upper row). At that time, care was taken of this effect by introducing a third component for each peak, having a fixed positive offset voltage.[5] However, the strength of this contribution was strongly fluctuating during the 2008 beamtime. It was particularly pronounced in the spectra of ^{10}Be for the D2 line. This was another reason to carefully check systematic effects on ^{10}Be during the 2010 test beamtime before using ^{10}Be as a reference. Spectra from both beamtimes are compared in Fig. 5.7. A collinear spectrum of the $2s\ ^2\mathrm{S}_{1/2} \rightarrow 2p\ ^2\mathrm{P}_{1/2}$ transition in $^{10}\mathrm{Be}^+$ is shown in graph *a*), taken at an ion beam of 10 pA and summed over 50 individual scans. A double Voigt (red line) is fitted to the peak which has a FWHM of 40 MHz. Treating the 2008 spectrum in (*b*) similarly shows that it is rather asymmetric and the FWHM amounts to about 70 - 80 MHz. Both spectra are superimposed in graph *c*) on axis where the peak center are shifted on top of each other and the areas are normalized. The differences are striking in this plot, please note that the conversion of the voltage-axis in (*a*) and (*b*) into frequency, separates the satellite peak from each other since the differential Doppler shift is different. A similar comparison is shown in graph (*d*) for the D2 line.
It is obvious that the asymmetry observed in 2008 is absent or at least strongly reduced in the new spectra. Even though the acceleration voltage was much lower than in 2008 a narrower and very symmetric peak shape was recorded. The origin of the asymmetric shoulder could not be clarified in 2008 but since it appears to be induced by ions that have more energy it was tentatively assigned to ions that were ionized at a different location inside the heated ionization pipe and thus started at a different potential. This "speculation" was supported by the observation that changes at the RILIS, *e.g.* realignment, were often accompanied by a sudden change of the shoulder intensity.
Therefore, the disappearance of the right shoulder as well as the smaller linewidth could be correlated to a much better focusing of the RILIS laser beams into the ionization tube. It should be mentioned that the run in 2010 was the first one with new solid-state pump lasers at RILIS which replaced the old copper vapor laser.

[5] In a detailed study [Zak10] is was shown that the collinear and anticollinear approach is rather tolerant against such asymmetries provided that they appear similarly in both spectra. There the D2 line was fitted with one, two and three Voigt profiles, resulting in an absolute shift of ^{10}Be of up to 15 MHz in an individual spectrum. But, combining both spectra results in a variation of ν_0 which was far less than 100 kHz.

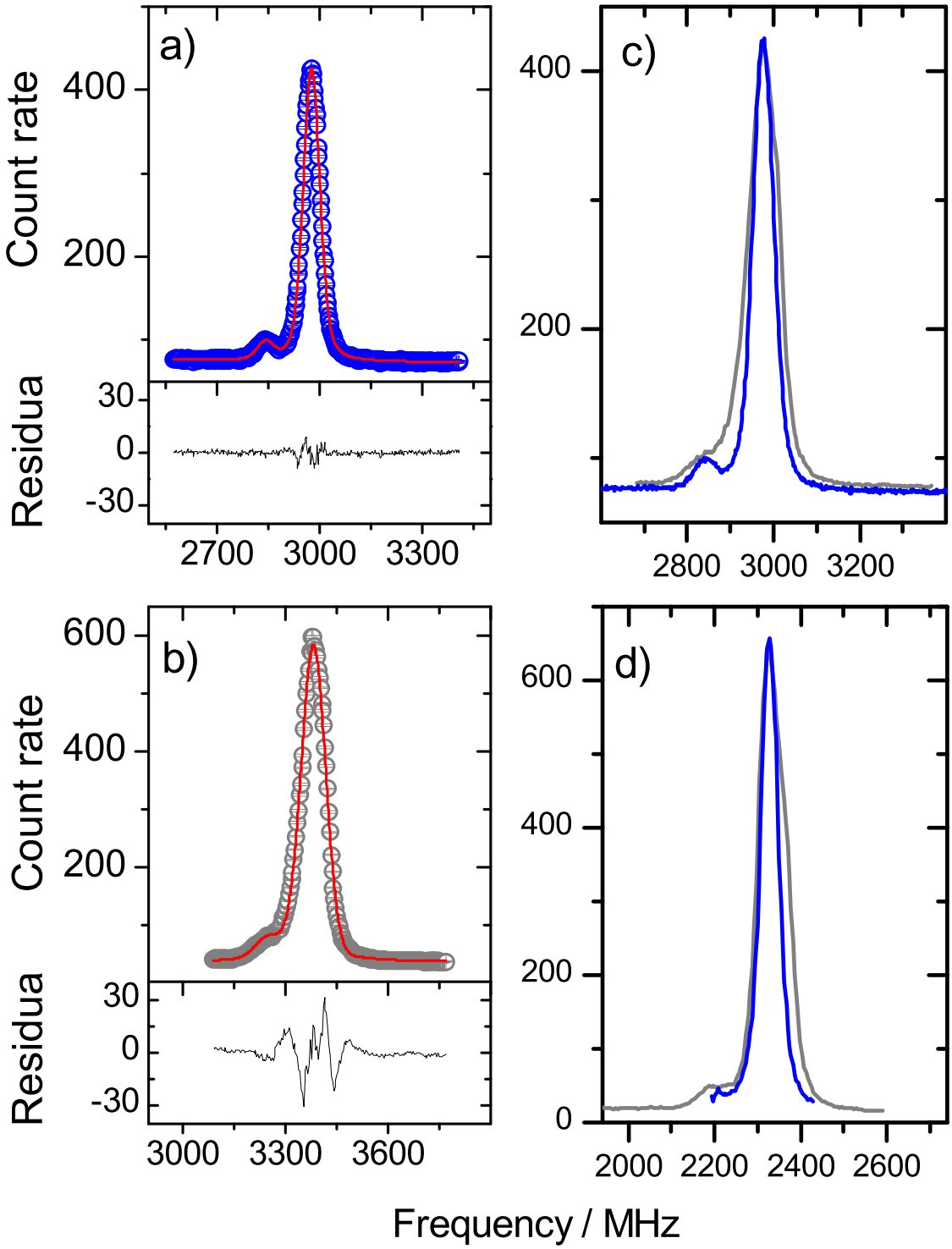

Figure 5.7: Resonance spectra of the $2s\ ^2S_{1/2} \rightarrow 2p\ ^2P_{1/2}$ transition in $^{10}Be^+$. Trace *a*) depicts the spectrum from 2010 fitted with a double voigt profile. In contrast to *b*) which shows the spectrum from 2008 in which the peak has twice the linewidth (80 MHz) compared to the peak in *a*) (40 MHz). In graph *c*) both peaks are superimposed according to their center positions and in *d*) the same is shown for the D2 line. The asymmetric peak structure observed in 2008 on the right is absent in the recent measurements. The scale for the residua is normalized to the peak maxima. The clearly improved line profile in the 2010 measurements is obvious.

5.6.1 Lineshape Fitting

From the investigations a fit routine was derived which calculates the hyperfine transitions according to the nuclear spin and the angular momentum of the involved electronic states. First, the Casimir formula is used to derive the peak positions based on the interval factors. According to [Kre04] the experimentally observed line shape is well approximated by a Voigt profile. To account for the satellite peak each hyperfine component is considered as a main peak and a satellite peak shifted by -4 V. During the χ^2 minimization the Lorentzian linewidth is kept fixed to the natural linewidth of 19.64 MHz while the Doppler width is a free parameter but common to all peaks in the spectra. The interval factors, the intensities of the main peaks and the center of gravity (cg) are free parameters of the fit. The ratio of the main peak to satellite peak intensities is also a free parameter but again common to all pairs of a fit. The third peak component used in 2008 to account for the larger asymmetry (for details see [Tie09, Zak10]) is completely removed. The cg frequencies ν_c and ν_{ac} obtained from fitting the quasi-simultaneously recorded collinear and anticollinear spectra, respectively, are then used to calculate the absolute transition rest-frame frequency ν_0. Before doing so, one must note that equation $\nu_0 = \sqrt{\nu_c \cdot \nu_{ac}}$ can only be used if the cg of both spectra coincides, which is usually not the case. But since the experimental conditions were chosen accordingly, the center of gravities deviate in all cases by a small voltage $\delta U \ll 1$ V. This difference can be taken care of by calculating the frequency shift, *e.g.*, of the collinear laser, required to let the cg of both spectra coincide. In first approximation[6], the required shift can be calculated by

$$\delta\nu = \delta\nu_{\text{diff}} \cdot \delta U \tag{5.11}$$

using the differential Doppler shift in Eq. 5.2. Referring to Eq. 5.11 the transition rest-frame frequency ν_0 is then calculated according to

$$\nu_0 = \sqrt{(\nu_c - \delta\nu_{\text{diff}} \cdot \delta U) \cdot \nu_{ac}}. \tag{5.12}$$

5.7 Systematic Uncertainties

The absolute transition frequencies ν_0 are afflicted with statistical as well as systematic uncertainties. Since each measurement was repeated for at least five times, the statistical uncertainties are derived from the standard deviation, which is typically of the order of several hundred kHz. The systematic uncertainties are discussed in detail in [Kri08, Tie09, Zak10] and are only summarized here.
The following modifications at the experimental setup were found to have no significant influence on the determined absolute transition frequencies:

[6] This linear relationship is justified by the very small differences δU and the introduced uncertainty can be safely neglected.

- stabilizing the collinear dye laser to different hyperfine transitions in molecular iodine
- varying the ion beam focusing
- using a focused but still parallel laser beam instead of a collimated beam
- changing the offset voltage at the fluorescence detection region or exchanging the power supply

5.7.1 Laser-Ion-Beam Alignment

It was found that the largest systematic uncertainties are caused by a possible misalignment of the laser beams relative to each other or to the ion beam. There are mainly two cases which have to be discussed:
If both laser beams are perfectly superimposed to each other but misaligned relative to the ion beam by an angle α, the Doppler formula becomes angle dependent

$$\nu_{c,ac} = \nu_0\gamma(1 \pm \beta \cdot \cos\alpha). \tag{5.13}$$

Consequently, the transition rest frame frequency ν_0 changes to

$$\nu_0 = \frac{1}{\gamma}\sqrt{\frac{\nu_c \cdot \nu_{ac}}{1-\beta^2 \cdot \cos^2(\alpha)}} = \sqrt{\frac{1-\beta^2}{1-\beta^2\cos^2(\alpha)}}\sqrt{\nu_c \cdot \nu_{ac}} \tag{5.14}$$

which results in an additional uncertainty

$$\Delta\nu_0 \approx \nu_0 \cdot \frac{\alpha^2\ \beta^2}{1-\beta^2} \approx \nu_0 \cdot 10^{-12} \approx \text{few kHz}. \tag{5.15}$$

The effect is small because the frequency shifts occurring in both directions are of opposite sign. The situation is different if only one laser beam is misaligned relative to the ion beam. Under the assumption that the second laser beam is perfectly overlapped with the ion beam Eq. 5.14 changes to

$$\nu_0 = \frac{1}{\gamma}\sqrt{\frac{\nu_c \cdot \nu_{ac}}{(1-\beta \cdot \cos(\alpha))(1+\beta)}} = \sqrt{\frac{1-\beta}{(1-\beta\cos\alpha)}}\sqrt{\nu_c \cdot \nu_{ac}} \approx \left(1-\beta\alpha^2\right)\sqrt{\nu_c \cdot \nu_{ac}}. \tag{5.16}$$

The uncertainty $\Delta\nu_0$ can be approximated according to

$$\Delta\nu_0 \approx \beta\alpha^2 \cdot \sqrt{\nu_\mathrm{c} \cdot \nu_\mathrm{ac}}. \tag{5.17}$$

Hence, the correction is only linear in β and a misalignment of 1 mrad between one laser and the ion beam causes a frequency shift of about 1.15 MHz. Two irises are inserted into the beamline with a distance of more than 2 meters to achieve a good overlap of all three beams. During the experiment the apertures were closed down to 5 mm. The diameter of the laser beams was measured to about 4 mm. The diameter of the ion beam was

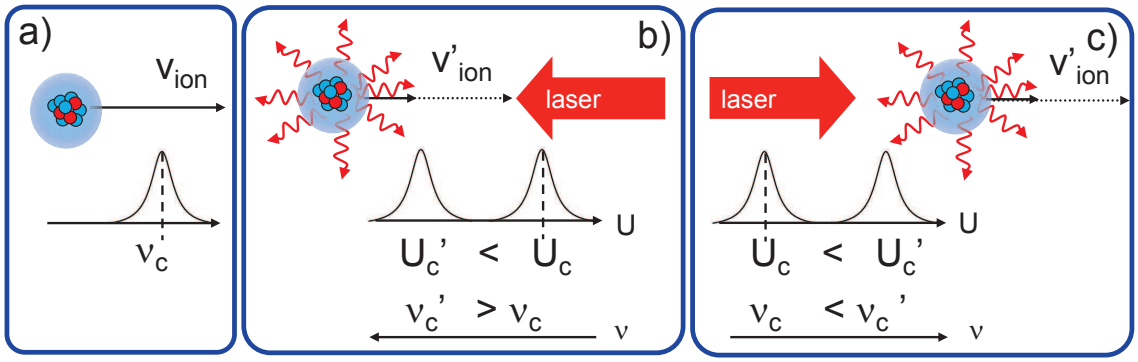

Figure 5.8: Illustration of the photon recoil effect. The directed photon absorption parallel and anti-parallel to the ion beam can cause a shift of the transition frequency to higher frequencies in both cases.

estimated to be smaller than 6 mm by closing the irises and measuring the transmission through the beamline.
De facto, this effect was investigated during the BeTINa beamtime in 2008 in detail by misaligning the collinear laser beam up to about 0.5 mrad. Finally, it was concluded that the laser alignment has a small effect on the absolute transition frequency and a systematic uncertainty of about 500 kHz was derived as a conservative estimate.
One of the major sources of systematic uncertainty in the 2008 beamtime was the estimated influence of a possible recoil shift, particularly in the case of ^{10}Be. This was further investigated in order to reduce its contribution.

5.7.2 Photon Recoil Shift

As already mentioned, the two even isotopes ^{10,12}Be exhibit no hyperfine splitting due to their vanishing nuclear spin. Therefore, both $2S \rightarrow 2P$ transitions in ^{10,12}Be$^+$ form a two-level system in which photons from the resonant laser beams can repeatedly be scattered. This effect is illustrated in Fig. 5.8 (a). An ion travels along the beamline with the velocity v_{ion}. In case of a resonant laser interaction (b) the photons of the anticollinear laser are directionally absorbed, but the excited ion will emit the photon isotropically. Hence, the photon recoil in absorption will systematically accelerate in collinear and deceleration in anticollinear geometry decelerate. This effect shifts the transition frequency ν_c to more positive and ν_{ac} to more negative post-acceleration voltages. But in the frequency domain this effect shifts both frequencies ν_c as well as ν_{ac} to higher frequencies $\nu_c' > \nu_c$ and $\nu_{ac}' > \nu_{ac}$. Thus, the calculated rest frame frequency is always too large $\nu_0' = \sqrt{\nu_c' \nu_{ac}'}$. It should be noted that the isotropic emission will only lead to a broadening of the transition. The hyperfine structure of the odd isotopes limits the number of photon interactions since the ion will soon be pumped into the hyperfine states of the ground state that does not interact with the laser (dark states). Hence, it is assumed that the photon recoil affects the even isotopes ^{10,12}Be$^+$ much more than the odd ones, like ^{9,11}Be$^+$. Since the yield of

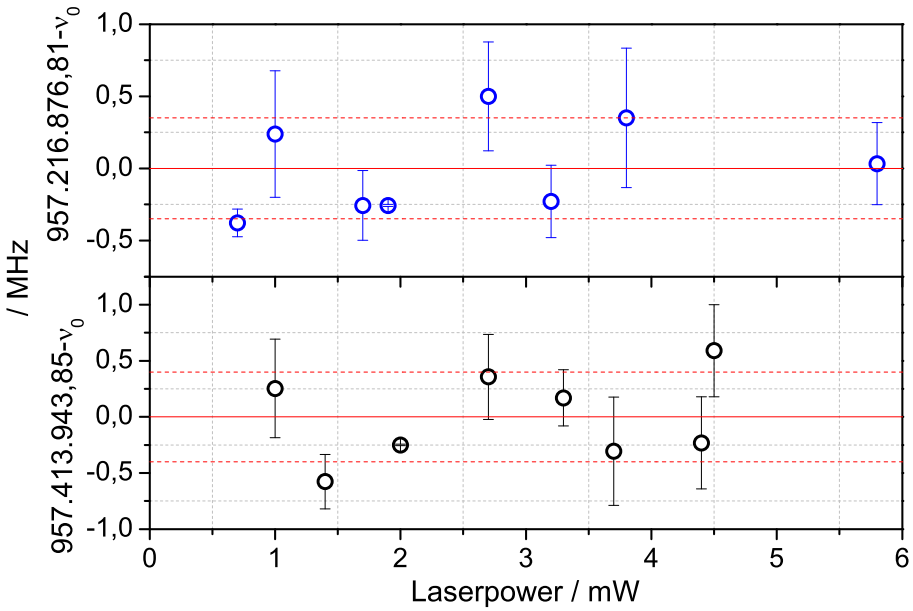

Figure 5.9: Measured absolute frequencies in the D1 (upper trace) and D2 transition (lower trace) of ^{10}Be as a function of laser power for equal power in both beams. The solid line represents the average transition frequency of all measurements with dashed lines representing the standard deviation. The error bar of each individual data point corresponds to the standard error of the mean for typically three measurements. No systematic frequency shift is observed.

^{10}Be is several orders of magnitudes larger than that of ^{12}Be, this effect was investigated on ^{10}Be. For that purpose the absolute transition frequency was determined as a function of the applied laser power ranging from 0.3 to 8 mW. These measurements were carried out in three steps: First, the laser power of the anticollinear laser was changed and the laser power of the collinear laser was kept constant. Then the measurement was repeated varying only the collinear laser intensity. Finally, both laser powers were increased simultaneously, which should lead to an even larger effect.
The results for the last case are summarized in Fig. 5.9. Plotted are the determined absolute frequencies ν_0 as a function of the laser power. The upper graph shows the deviation of each individual measurement to the absolute frequency determined for the D1 and the lower graph for the D2 transition. It shows that - within the statistical uncertainty - the peak position remains unaffected with increasing laser power. No difference occurred if one laser power was kept fix or if both laser powers were increased simultaneously. Obviously the number of resonant interactions with the laser beam is not sufficient to cause a measurable recoil shift even at the maximum laser power of 8 mW. Since a systematic effect was not observed and the recoil shift contributes only differentially to the isotope shift, a conservative upper limit of 100 kHz was taken into account for $\Delta\nu_{\mathrm{Ph}}$ which was achieved by fitting a linear function to the data points.
As mentioned above the Lorentzian linewidth of the Voigt profile is fixed to the natural

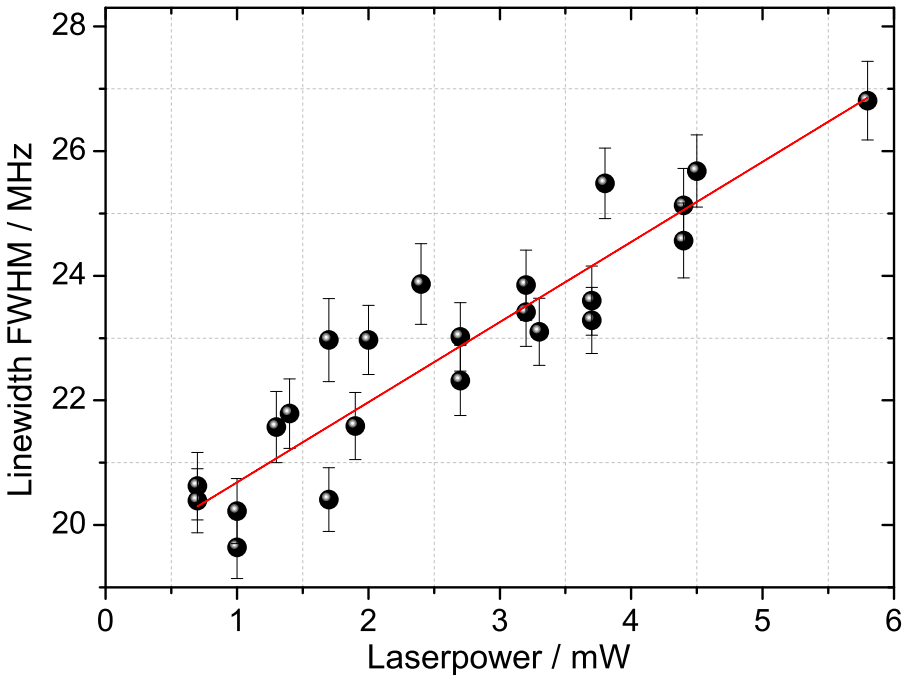

Figure 5.10: Gaussian contribution to the full width half maximum FWHM as a function of laser power. A linear function (red line) is fitted to the data. The power broadening can be estimated to (1.28 ± 0.12) MHz/mW

linewidth. But an increase of laser power leads to saturation broadening which is a homogeneous broadening mechanism and therefore contributes to the Lorentzian linewidth. Hence, the fitting routine must accommodate for the increasing width by enlarging the Gaussian contribution. Figure 5.10 shows the Gaussian contribution (FWHM) to the linewidth as a function of laser power for the collinear spectra. Similar results were achieved for the anticollinear interaction. The effect of power broadening is clearly visible and can be roughly estimated by fitting a linear function to the data points[7]. From this fit the effect of power broadening the linewidth is obtained to be (1.28 ± 0.12) MHz/mW.

5.8 Setup of the Photon-Ion Coincidence Detection

The resonant excitation of the $2s\ ^2\mathrm{S}_{1/2} \rightarrow 2p\ ^2\mathrm{P}_{1/2}$ transition in $^{10}\mathrm{Be}^+$ as shown in Fig. 5.7 was used to optimize the photon-ion coincidence detection unit. The maximum count rate of the SEM installed at COLLAPS is a few MHz, thus the ion beam had to be attenuated. The second dye laser from RILIS was blocked and the ionization limited to a non-resonant ionization with the first-step laser. In this configuration we detected an ion beam rate of

[7] The right treatment would have been to have the Lorentzian linewidth as a free parameter of the fit and perform the χ^2 reduction with the realistic power broadening formula $\Delta\nu = \Delta\nu_0\sqrt{1+S}$

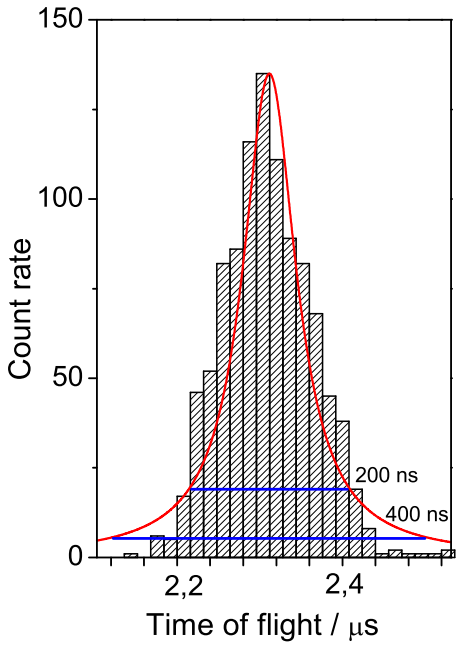

Figure 5.11: Time of flight spectrum of $^{10}Be^{+}$ taken with a multi channel analyzer. A photon signal was used as the start, whereas the stop was provided from the coincident ions. A Lorentzian is fitted to the histogram.

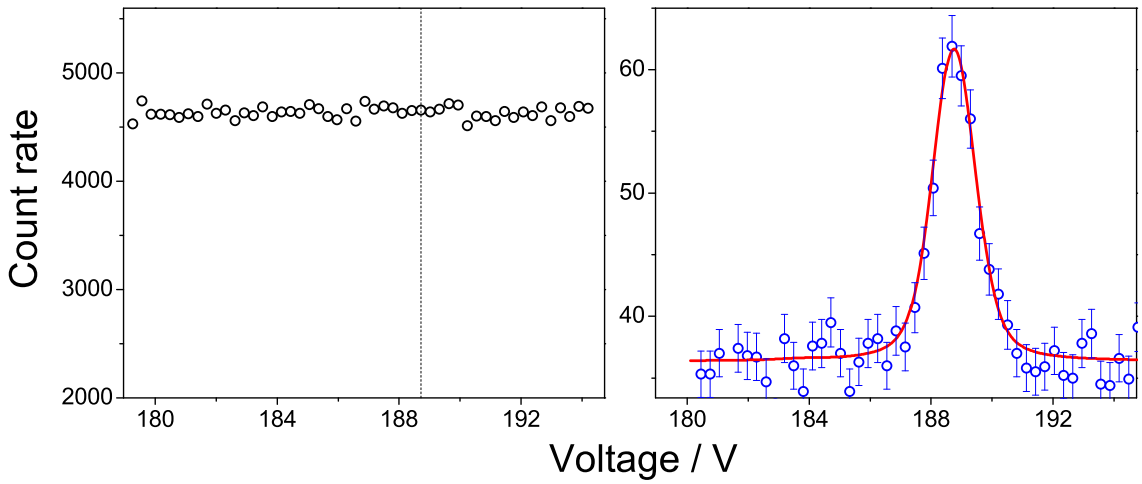

Figure 5.12: Comparison of conventional optical fluorescence detection (left) and photon ion coincidence detection (right) at an ion beam of 30 000 ions/s. The optical spectrum shows only stray light (the resonance curve is totally covered by the stray light and for illustration only it is depicted where it is expected (dashed line). In the photon-ion coincidence spectrum a clear resonance is observable.

about 30.000 ions/s with the SEM. The post acceleration voltage was tuned to the peak center to obtain a large number of fluorescence photons. A multi channel analyzer (MCA SRL-211) was used to measure the ion's time of flight (TOF) from the FDR to the SEM. The MCA was triggered by the photon signal and the SEM signal provided the stop. A spectrum is depicted in Fig. 5.11. A clear maximum is observed at 2.3 μs and the center of the delay gate for the coincidence condition is set accordingly. It was found that the spectrum is well described by a Lorentzian profile. The food-width of the TOF signal is about 200 ns but a rather conservative coincidence gate of 370 ns was used. Similar to the setup at TRIGA-LASER in Mainz an FPGA digitally delayed the photomultiplier signal accounting to the ion's time of flight to avoid deadtime of the coincidence electronics.
The coincidence detection was then tested using the attenuated ^{10}Be beam. The signals from the photomultiplier were fed into a scaler for conventional detection and into the ion-photon coincidence unit. Those events that were in delayed coincidence with an ion event were recorded by a second scaler. A spectrum was integrated for a total of 15 min. Figure 5.12 shows a comparison of the conventional optical fluorescence spectrum (left) and the coincidence spectrum (right). In the conventional ungated spectrum the resonance curve is totally covered by the background from laser stray light, whereas the optical spectrum detected in delayed coincidence with the corresponding ion signal shows a nice and clear curve. The background by stray light is reduced roughly by a factor of about 100. This is close to the expected reduction R of

$$R = \frac{1}{30 \cdot 10^3 \text{ions/s} \cdot 3.7 \cdot 10^{-7} \text{s}} \approx 90. \tag{5.18}$$

Due to the very low production rate for $^{12}Be^+$ a TOF spectrum using the MCA can not be recorded within a reasonable time. Thus, the settings for the delay and the gate width were calculated according to the difference in mass and the corresponding difference in velocity. The transition rest frame frequency ν_0 of ^{10}Be was determined from the coincidence spectrum in Fig. 5.12 and compared to the conventional optical spectrum at higher beam intensity, *e.g.* Fig. 5.7. The deviation was smaller than the pure statistical uncertainty of about 300 kHz.

5.8.1 Spectroscopy of Short-lived Be-12

For the investigation of $^{12}Be^+$ a proton pulse impinged the target every 3-5 seconds. According to the release curve the extraction of the ions were done within 60 ms after the proton pulse. Resonance spectra of the $2s\ ^2S_{1/2} \rightarrow 2p\ ^2P_{1/2,3/2}$ transitions in $^{12}Be^+$ were obtained using the technique of delayed photon-ion coincidence detection. A typical spectrum observed during the beamtime is shown in Fig. 5.13. Such a spectrum is the sum of 180 individual scans which were recorded in about 8 hours. Similar to all other measurements the laser power was kept at 3 - 4 mW. A signal to noise ratio (S/N) of the order of about 10 was obtained after integrating for about two hours. Due to the low production rate the Doppler-tuning voltage was restricted to about 200 MHz (6 V scanning voltage), so that only the main peak was observable. The symmetric spectra are

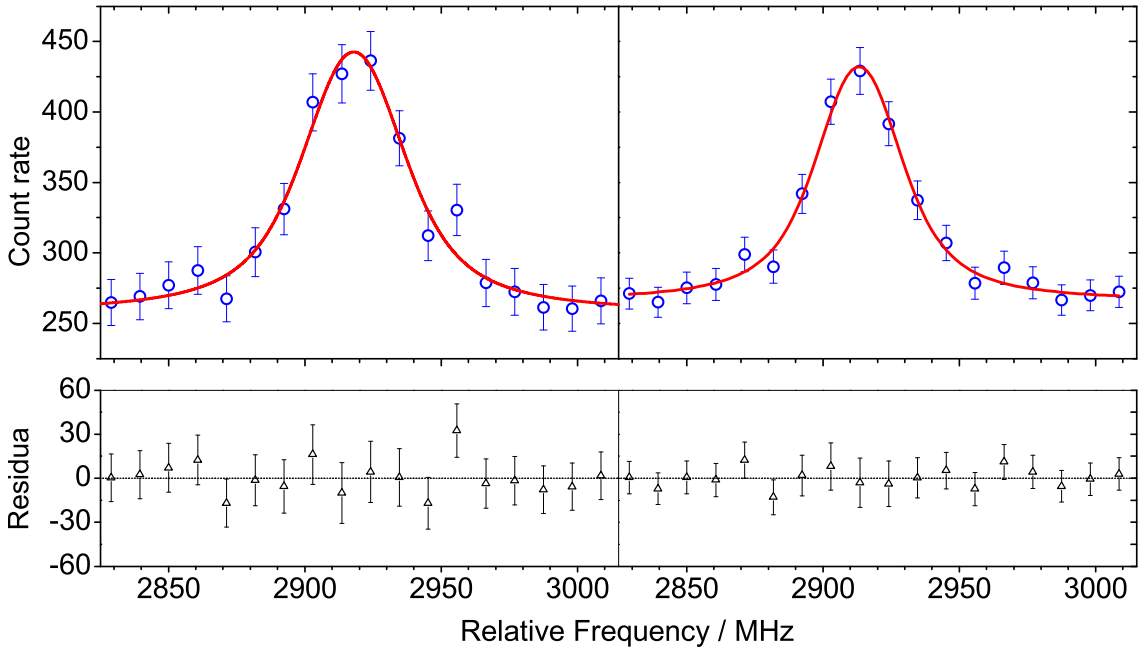

Figure 5.13: Resonance spectra of the $2s\ ^2S_{1/2} \rightarrow 2p\ ^2P_{1/2}$ transition in $^{12}Be^+$ in collinear (left) and anticollinear direction (right). The RILIS production rate was about 8000 ions/pulse and scans were integrated for 2 hours. The laser power was about 3 mW. The data points are fitted with a single Voigt profile with the Lorentzian fixed to the natural linewidth. Below the resonance profile (red) the residuals of the fit are displayed.

thus fitted with a single Voigt profile. The Lorentzian contribution was kept fixed to the natural linewidth which is about 20 MHz. Similar to the spectra of all other beryllium isotopes, a linewidth of 40 MHz was observed with a Gaussian contribution of 30 MHz. The lower trace in Fig. 5.13 shows the residua of the corresponding Voigt fit, which affirms a symmetric peak structure. The reduced χ^2 is about 1.1 in both cases. The statistical uncertainty given by the standard deviation of all measurements is less than 300 kHz. In the same way the D2 transition (the transition strength equals the D1 transition) was investigated. After each spectrum (recording time about 2 hours), the measurement was interspersed in order to perform three reference scans on $^{10}Be^+$. In this way, each spectrum can be directly related to the reference scan.
The detection efficiency ϵ_{det} of the coincidence detection setup for $^{12}Be^+$ can be calculated using the data presented in Fig. 5.13. The background level b is about 260 counts and the signal height about 180 counts. The sweep time per channel was set to 100 ms. A total of 180 individual scans were summed up which corresponds to a total of 18 s for each channel. The ion flux was measured to about 8000 ion/pulse from which the detection efficiency ϵ_{det} is obtained using the count rate in resonance

$$\epsilon_{\text{det}} = \frac{8000 \text{ ions} \cdot 18 \text{ s}}{180 \text{ photons}} = 800 \text{ ions/photon}. \tag{5.19}$$

Table 5.3: Hyperfine constants A_{2s} and A_{2p} for $^{9,11}Be^{+}$ and the magnetic moment of ^{11}Be extracted from the measurements and comparison with the BeTINa beamtime in 2008 [Tie09].

A	A_{2s}	A_{2p}	μ	Source
9	-625.001(149)	-118.028(082)	ref.	[Tie09]
9	-625.164(343)	-118.112(199)	ref.	this work
11	-2677.665(774)	-505.470(499)	-1.6816(8)	[Tie09]
11	-2676.974(987)	-504.974(676)	-1.6819(11)	this work

This is an excellent value and about a factor of 20 improvement compared to the 2008 BeTINa run where an efficiency of 15 000 ions/photons was determined. A similar efficiency was also calculated for the reference isotope ^{10}Be, investigated with classical fluorescence detection. This enhancement is related to a careful alignment and the installation of newer photomultiplier tubes which have a significantly higher quantum efficiency in the UV region (20% compared to 5%).

5.9 Results

5.9.1 Absolute Transition Frequencies

In total 31 (19) spectra of ^{10}Be and 27 (12) spectra of ^{12}Be for the D1 (D2) transition were recorded during the beamtime. Additionally 7 and 5 spectra of ^{9}Be and ^{11}Be, respectively, were taken to compare the results to the 2008 beamtime. Fitting was performed with the procedure described in Section 5.6.1. For each pair of spectra, the center of gravity and the respective rest frame frequency was obtained according to Eq. 5.7. For the odd isotopes $^{9,11}Be$ the hyperfine splitting factors A_{2s} and A_{2p} were also extracted. These are listed in Tab. 5.3 and compared to data from the 2008 beamtime. Uncertainties are calculated as the standard deviations of all measurements. Due to the rather limited number of spectra recorded for these isotopes, the accuracy is not competitive to that reached in 2008, but all values agree within their statistical uncertainty. Absolute frequencies are determined from Eq. 5.12. The results are summarized in Tab. 5.4. The absolute transition frequencies ν_0 are listed with the statistical uncertainty in squared brackets which is the standard deviation of all measurements. The uncertainty given in round brackets is the corresponding total uncertainty which also includes the systematic uncertainties that contribute according to Section 5.7. The individual contributions are listed in Tab. 5.5. Most significant improvements compared to 2008 are the GPS tracking of the Rb-clock that served as a reference of the frequency comb and the systematic study of an assumed photon recoil effect. As mentioned in Section 5.5 all absolute frequencies determined during the beamtime in 2008 were afflicted with an uncertainty of the Rb-clock contributing

Table 5.4: The absolute transition frequency ν_0, isotope shift ν_{IS}, field shift ν_{FS}, change in the mean square nuclear charge radius $\delta\langle r^2\rangle$ and the absolute radius R_c. The uncertainty given in squared brackets is the statistical uncertainty and in round brackets the total uncertainty. The reference radius $R_c\left({}^9\mathrm{Be}\right) = 2.519(12)$ fm is used to determine the nuclear charge radius R_c. Each radius was extracted with a relative uncertainty of about 1% whereby the uncertainty of the reference radius $\Delta R_c\left({}^9\mathrm{Be}\right)$ dominates the total uncertainty. Note, that ^{7}Be was not investigated anymore, therefore the given values are determined from the 2008 data but with due to the investigations of the photon recoil effect.

Isotope	ν_0 /MHz	$\delta\nu_{IS}^{9,A}$ /MHz	$\delta\nu_{\mathrm{FS}}$ /MHz	$\delta\langle r^2\rangle$ /fm^2	R_c /fm
^{7}Be$^+$	957 150 316.15[76](92)	-49 236.88(97)	-11.10(99)	0.66(6)	2.646(16)
^{9}Be$^+$	957 199 553.40[12](55)	0	0	0	2.519(12)
^{10}Be$^+$	957 216 876.84[42](66)	17 323.45(83)	13.01(83)	-0.77(5)	2.361(17)
^{10}Be$^+$ D2	957 413 942.17[44](70)	17 325.6(16)	13.0(16)	-0.77(9)	2.361(24)
^{11}Be$^+$	957 231 118.11[10](55)	31 564.71(73)	4.42(72)	-0.26(4)	2.466(15)
^{12}Be$^+$	957 242 944.86[33](61)	43 391.46(80)	1.29(79)	-0.08(5)	2.503(15)
^{12}Be$^+$ D2	957 440 013.60[28](58)	43 397.0(16)	1.5(16)	-0.09(9)	2.501(22)

Table 5.5: Systematic uncertainties that contribute to the total uncertainty of the determined transition frequencies. The laser-/ion beam alignment clearly dominated the total systematic uncertainty.

Uncertainty	Contribution /kHz
Laser-/ion beam alignment $\Delta\nu_{\mathrm{al}}$	500
Uncertainty of the atomic clock $\Delta\nu_{\mathrm{fc}}$	40
Photon recoil $\Delta\nu_{\mathrm{ph}}$	100
Total systematic uncertainty $\Delta\nu_{\mathrm{sys}}$	510

with 820 kHz. The GPS tracking calibrates the atomic clock to the GPS time standard and decreases the uncertainty $\Delta\nu_{\mathrm{fc}}$ from 820 kHz to 40 kHz (reduction to 5%).
In the analysis of the 2008 data [Tie09, Zak10, Noe09] a photon recoil shift could not be excluded. An estimated shift of the transition frequency ν_0 was quadratically added to the total uncertainty. Multiple photon absorption shifts the frequency systematically to higher frequencies and thus contributes to lower frequencies only. As described in Section 5.7.2 the resonance peak position remains unaffected by different laser powers. Nevertheless a conservative upper limit of 100 kHz is included to the total systematic uncertainty. This is a reduction to 10% of the previous value of 1 MHz and 7% in case of ^{10}Be, respectively. All systematic uncertainties are assumed to be uncorrelated and thus the total uncer-

tainty $\Delta\nu_0$ can be calculated as the geometrical average of systematic uncertainties and the statistical uncertainty according to

$$\Delta\nu_0 = \sqrt{(\Delta\nu_{\mathrm{stat}})^2 + (\Delta\nu_{\mathrm{al}})^2 + (\Delta\nu_{\mathrm{fc}})^2 + (\Delta\nu_{\mathrm{ph}})^2} \tag{5.20}$$

The absolute transition frequencies ν_0 were determined with a relative accuracy better than 1 MHz. The accuracy could also be reached in case of $^{12}Be^+$ with its low yield of 10 000 ions/pulse. At this point it should be noted that also the systematic uncertainties of the transition frequencies from 2008 were improved since the assumed photon recoil effect was overestimated with more than 1 MHz.

5.9.2 Isotope Shifts

The isotope shifts $\delta\nu_{IS}^{9,A'}$ are calculated as the difference between the absolute transition frequency $\Delta\nu_0$ of the isotope A' relative to ^{9}Be. The results are listed in Tab. 5.4. Equation 5.20 is not valid to calculate the uncertainty of the isotope shifts $\Delta\delta\nu_{\mathrm{IS}}^{9,A'}$ since some of the uncertainties must be treated differentially, such as the frequency comb- as well as the photon recoil related uncertainties cancel out. Thus, the total uncertainty of the isotope shift $\Delta\delta\nu_{\mathrm{IS}}^{9,A'}$ is calculated by

$$\Delta\delta\nu_{\mathrm{IS}}^{A,A'} = \sqrt{(\Delta\nu_{\mathrm{stat}})^2 + (\Delta\nu_{\mathrm{al}})^2} \tag{5.21}$$

and becomes smaller than the uncertainty of the absolute transition frequencies $\Delta\nu_0$.

5.9.3 Nuclear Charge Radii

The field shift values $\delta\nu_{FS}$ can be extracted as the difference between the determined isotope shifts $\delta\nu_{IS}^{9,A'}$ from Tab. 5.4 and the calculated mass shift data $\delta\nu_{MS}^{9,A'}$ from Tab. 2.2. The change of the root mean square charge radius $\delta\left\langle r^2\right\rangle^{9,A'}$ can then be calculated by

$$\delta\left\langle r^2\right\rangle^{9,A'} = \frac{\delta\nu_{FS}^{9,A'}}{C}, \tag{5.22}$$

where C denotes the field shift constant listed in Tab. 2.2. Finally, the root mean square charge radius R_c is obtained based on the absolute charge radius of ^{9}Be $R_c(^9\mathrm{Be}) = 2.519(12)$ fm [Jan72]

$$R_c = \sqrt{\delta\left\langle r^2\right\rangle^{9,A'} + R_c^2(^9\mathrm{Be})}. \tag{5.23}$$

The absolute charge radii R_c are listed in Tab. 5.4. Due to the absence of nuclear spin, the charge radii of $^{10}Be^+$ and $^{12}Be^+$ are determined from the D1 and D2 transition with similar accuracy and are consistent. The determined charge radii are plotted in Fig. 5.14. The trend of the decreasing nuclear charge radius from ^{7}Be to ^{10}Be and the increase to

^{11}Be from 2008 (blue dots) could be well reproduced in the beamtime 2010 (red dots). It was found that the nuclear charge radius of ^{12}Be is even larger than that of the one-neutron halo nucleus ^{11}Be.
The experimental results benchmark the nuclear charge radius calculations derived from the Fermionic Molecular Dynamics Calculations as included in Fig. 5.14, whereby gray squares depict results of mean field and black squares of multi-configuration calculations [Nef11].

Previous FMD calculations described in [Zak10] reproduced the trend of the charge radii in the beryllium isotopes up to ^{11}Be, but failed to describe the parity inversion of ^{11}Be. The employed effective interaction predict a too large gap between the *p*- and *sd*-shell orbits in this nucleus.
The interaction between the *p*- and *sd*-configurations dominates also the configuration in ^{12}Be. Therefore the effective interaction (based on the Argonne V18 potential [Wir95]) was modified within the unitary correlation operator UCOM method [Nef03] in such a way that a phenomenological parameter η was introduced to influence the strength of the spin-orbit force. This was successfully applied to describe the ^{3}He(α,γ)^{7}Be capture reaction [Nef11]. In case of beryllium this modification increased the binding and thus the relative position of *p*- and *sd*-orbits. The parameter η was modified to fit the experimental separation energies for each isotope.
As discussed in Section 2.3 the intrinsic states of the beryllium isotopes show an α-cluster structure and the distance between the α-clusters changes between isotopes. This clustering effect is reflected in the charge radius decrease from ^{7}Be to ^{10}Be. The sudden change to an increasing charge radius at ^{10}Be is not the result of a shell closure, as it is often observed for heavier nuclei, but related to the motion of the ^{10}Be core of ^{11}Be relative to the center-of-mass of the core and the single halo-neutron in an extended *s*-orbit.
In the FMD calculations of the 0^+ states of ^{12}Be two local minima were found. These correspond to a pure p^2 (as predicted from the nuclear shell model) and a pure $(sd)^2$ intruder configuration. A cut through the intrinsic densities of both configurations is depicted in Fig. 5.15. It was found that for a pure p^2 configuration the charge radius is comparable in size to that of ^{10}Be, whereas the pure $(sd)^2$ configuration shows a significantly larger charge radius. The latter is attributed to an increased distance of the α-clusters as well as to a neutron-correlation which forms an α-^{8}He like structure. Due to the larger neutron separation energy the neutron appearance in the $(sd)^2$ configuration in ^{12}Be completely differs from the *s*-wave halo one in ^{11}Be which is forced by a very small neutron separation energy[8]. Therefore, the $(sd)^2$ matter radius $R_m(^{12}\text{Be}) = 2.58$ fm (in $(sd)^2$ configuration) is significantly smaller than that of the halo nucleus $R_m(^{11}\text{Be}) = 2.80$ fm. At that point it should further be noted that the FMD calculations of the p^2 and $(sd)^2$ configurations are challenging since the amount of mixing is extremely sensitive to the energy difference between the states.
As shown in Tab. 5.6 the adjustment of the spin-orbit force to the separation energies is in good agreement with all known monopole $M(E0)$ and the $B(E2)$ electric quadrupole

[8] In the FMD calculations the $(sd)^2$ configuration is described by a linear combination of *d*- and *s*-orbits and can not easily be decomposed into an *s*- and a *d*-part.

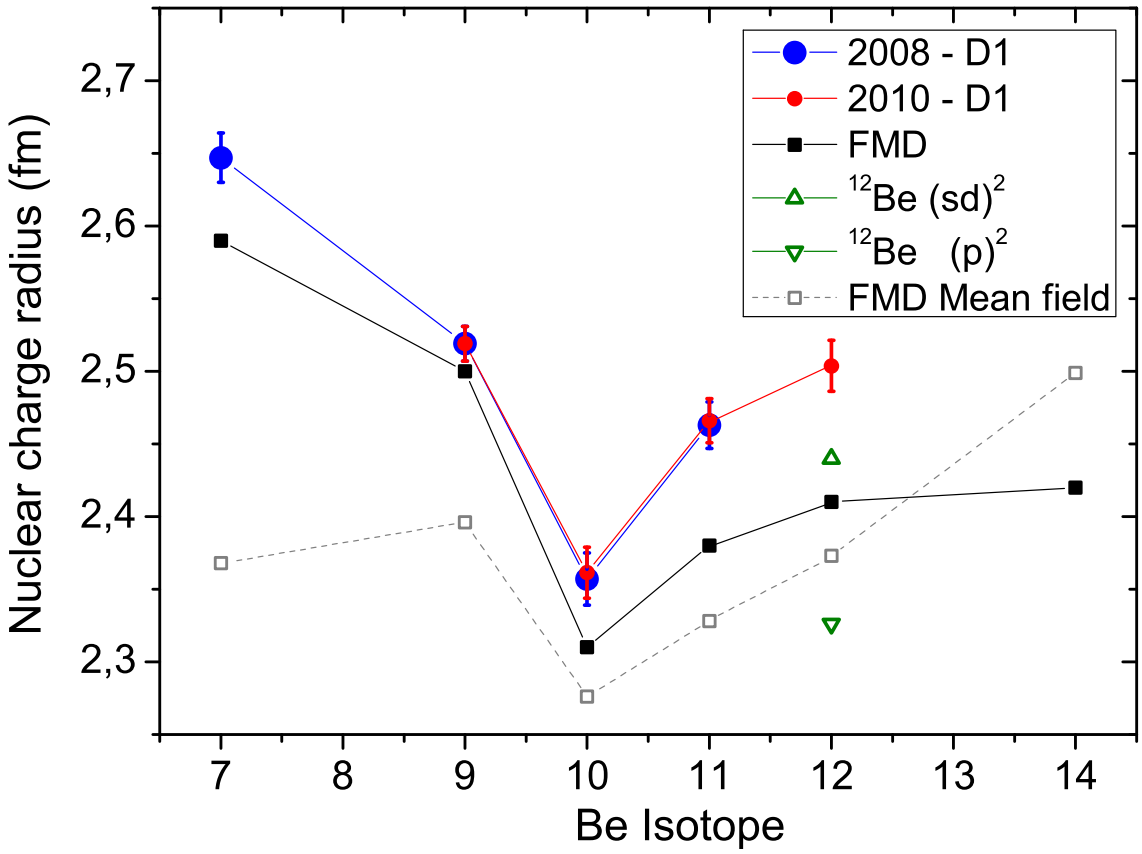

Figure 5.14: Nuclear charge radii of the beryllium isotopic chain. The reference radius of ^{9}Be was determined from electron scattering experiments [Jan72]. The blue bullets (●) depict the results from the first run of the BeTINa experiment [Tie09] from $^{7-11}$Be whereas the 2010 data extended the measurements up to ^{12}Be (this study ●). The gray squares □ represent the Fermionic Molecular Dynamics calculations in the mean field configuration and ■ depict the calculated charge radii in the advanced multi configuration (see text). The charge radii calculated for the pure p^2-configuration (▽) and pure $(sd)^2$ intruder configuration (△) are indicated.

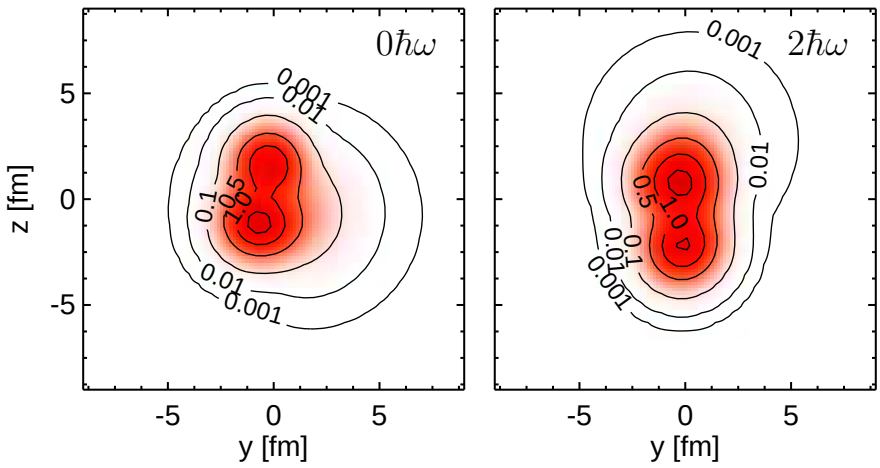

Figure 5.15: The intrinsic densities of the derived ^{12}Be states in the p^2 state ($0\hbar\omega$) and the $(sd)^2$ intruder ($2\hbar\omega$) configuration (right).

transitions. With the optimized values, the $(sd)^2$ configuration contributes about 70% to the ground state. This huge contribution is responsible for the larger charge radius than that calculated for ^{11}Be by about 0.03 fm. With these modifications the trend of the experimentally derived charge radii from ^{9}Be to ^{12}Be can be reproduced, except the fact that they are a little bit smaller, especially the heavier isotopes. If one assumes that the uncertainty of the charge radius of ^{9}Be is 1% only, a possible explanation might be related to deficiencies of the effective interaction which is known to saturate at too high densities for heavier nuclei [Rot10]. This intruder-state mixing was already indicated in scattering experiments [Oza00, Nav00, Iwa00, Iwa02, Aoi02]. The FMD calculations can not separate the contributions of the d^2 and the s^2 configurations. In these experiment a strong influence of the lowering of the $d^2_{5/2}$ orbits was concluded which causes a prolate deformation and thus a strong clustering effect inside this nucleus.
The FMD calculations, in good agreement with the experimental results observed during the framework of this thesis, hence support the breakdown of the magic shell closure at N = 8 in the Be isotope and give evidence to the extended $(sd)^2$ spatial structure of ^{12}Be.

5.9.4 Splitting Isotope Shift Measurements

A valuable test of the theoretical mass shift calculations [Puc10, Dra10] can be provided by comparing the experimental splitting isotope shift $\delta\nu^{A,A'}_{\mathrm{SIS}}$, which is the difference in the isotope shifts between the D1 and D2 transitions with the theoretical predictions. In the SIS all mass-independent terms and the finite size correction cancel. It is caused by the different spin orbit coupling and thus provides a stringent test of the theory. In lithium the SIS amounts only to a few hundred kHz and its determination is difficult due

Table 5.6: Charge and matter radii of different ^{12}Be configurations and the magnetic and electronic transition strengths $M(E0)$ and $B(E2)$ for the mixed eigenstate obtained in the FMD calculation and comparison with the experiment.

		FMD	Exp
^{12}Be - p^2	R_c[fm]	2.33	–
	R_m[fm]	2.41	–
^{12}Be - $(sd)^2$	R_c[fm]	2.44	–
	R_m[fm]	2.58	–
^{12}Be	R_c[fm]	2.41	2.502
	R_m[fm]	2.52	2.59(6)
	$B(E2; 2_1^+ \rightarrow 0_1^+)[e^2$ fm$^4]$	8.75	8.0(3.0) [Shi07]
	$B(E2; 0_2^+ \rightarrow 2_1^+)[e^2$ fm$^4]$	7.45	7.0(6) [Ima09]
	$M(E0; 0_1^+ \rightarrow 0_2^+)[e$ fm$^2]$	0.90	0.87(3) [Ima09]

to unresolved hyperfine structure in the D_2 transition. Figure 5.16 presents the status for the lithium isotopes. It is obvious that experimental data obtained between 1995 and 2007 [San95, Sch96, Wal03, Nob06, Das07] scatter strongly and was not in agreement with theory with one exception [San95], but this result had a rather large uncertainty.

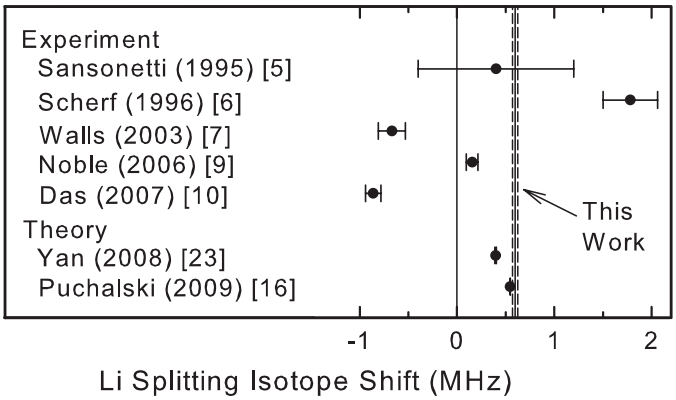

Figure 5.16: Li splitting isotope shift. Taken from [San11].

Recently, the transition have been re-investigated at NIST [San11] and the SIS was obtained with high accuracy and disagreed by 390 kHz (6σ) with the atomic structure calculations by Yan and coworkers [Yan08]. However, reasonable agreement was found with the calculations by Puckalski and Pachucki, who included the effect of hyperfine-induced mixing of the ^{2}P$_{1/2}$ and ^{2}P$_{3/2}$ states.
Compared to lithium the SIS in beryllium is an order of magnitude larger. The ^{2}P$_{3/2}$ hyperfine structure is unresolved as in the case of lithium, but beryllium offers even isotopes that that do not exhibit a hyperfine structure at all. Since the isotope shifts were

Table 5.7: The Be splitting isotope shifts $\delta\nu_{\mathrm{SIS}}^{A,A'}$ relative to $A = {}^{9}$Be and in the last row $\delta\nu_{\mathrm{SIS}}^{12,10}$. If required, the transition frequencies of the D2 line are taken from [Zak10]. The splitting isotope shifts $\delta\nu_{\mathrm{SIS}}^{A,9}$ from [Zak10] are listed in the third column. Two independent theoretical calculations from [Puc10, Dra10] are further listed. All values given in MHz.

SIS (A, A')	$\delta\nu_{\mathrm{SIS,EXP}}^{A,A'}$	$\delta\nu_{\mathrm{SIS,EXP}}^{A,A'}$ [Zak10]	$\delta\nu_{\mathrm{SIS}}^{A,A'}$ [Puc10]	$\delta\nu_{\mathrm{SIS}}^{A,A'}$ [Dra10]
^{7}Be - ^{9}Be	5.2(20)	5.1(22)	6.035(49)	6.049(54)
^{10}Be - ^{9}Be	-2.1(18)	-3.5(24)	-2.094(18)	-2.127(17)
^{11}Be - ^{9}Be	-4.1(20)	-3.6(25)	-3.962(44)	-3.878(34)
^{12}Be - ^{9}Be	-5.5(12)		-5.300(25)	-5.331(55)
^{12}Be - ^{10}Be	-3.4(22)		-3.210(25)	-3.200(55)

determined with an accuracy better than 1 MHz this offers an excellent opportunity to test the atomic structure calculations. The SIS calculated from the experimental data $\delta\nu_{\mathrm{SIS,EXP}}^{A,A'}$ and two independent theoretical results $\delta\nu_{\mathrm{SIS}}^{A,A'}$ [Puc10, Dra10] are compared in Tab. 5.7. The consistency of the splitting isotope shift between experiment and theory is striking. The SIS for the other isotopes are discussed in [Zak10] and are also depicted in Fig. 5.17. Compared to [Zak10], $\delta\nu_{\mathrm{SIS,EXP}}^{10,9}$ (from this work) is about 1 MHz lower and in excellent agreement with the theory. Note, that the upper trace shows the $\delta\nu_{\mathrm{SIS,EXP}}^{12,10}$ ^{12}Be - ^{10}Be.

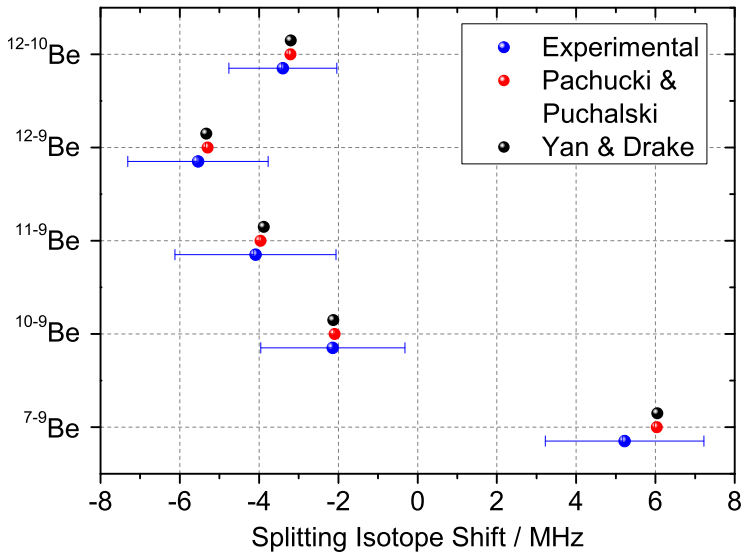

Figure 5.17: The splitting isotope shift of ^{7,10,11,12}Be relative to ^{9}Be. In the very upper row the splitting isotope shift ^{12,10}Be is depicted. Two independent theoretical calculations [Puc10, Yan10] are included.

6 High Voltage Determination in the ppm Regime at ISOLDE

Figure 6.1: The ASTEC power supplies located in the ISOLDE's HV cage.

While the frequency comb based combined collinear and anticollinear technique used for beryllium does not depended on the exact knowledge of the acceleration voltage, it requires a doubling of the laser system and is therefore too complex for less demanding measurements on heavier isotopes. In these cases it is required to know the acceleration voltage typically with an accuracy of at least 10^{-4}. This is the limit for commercial HV dividers.
At the University of Münster, a new high accuracy voltage divider with a reported accuracy of 1 ppm was developed for the KATRIN experiment. In cooperation with the Münster group this divider was transported to CERN, used for a calibration of the HV dividers and the calibration was checked using the frequency comb based spectroscopy on beryllium. These activities were triggered by the observation of a significant change of isotope shifts between two beamtimes where different high voltage dividers at ISOLDE were used. The results are also important for TRIGA-LASER, since a reliable and high accuracy voltage determination has to be installed there as well.

6.1 Calibration of the ISOLDE High Voltage Installations

Voltages of the order of a few volts are precisely measured with a relative accuracy of typically 10^{-12}, taking advantage of the Josephson effect [Jos62]. In contrast, higher voltages above 10 V are out of reach for measurements with such high accuracy. The applied high voltage must be downsized to be applicable for a precise multimeter. Such a high-precision voltage divider was developed for the KATRIN[1] experiment which uses a

[1] KArlsruhe Tritium NeutRINo mass experiment

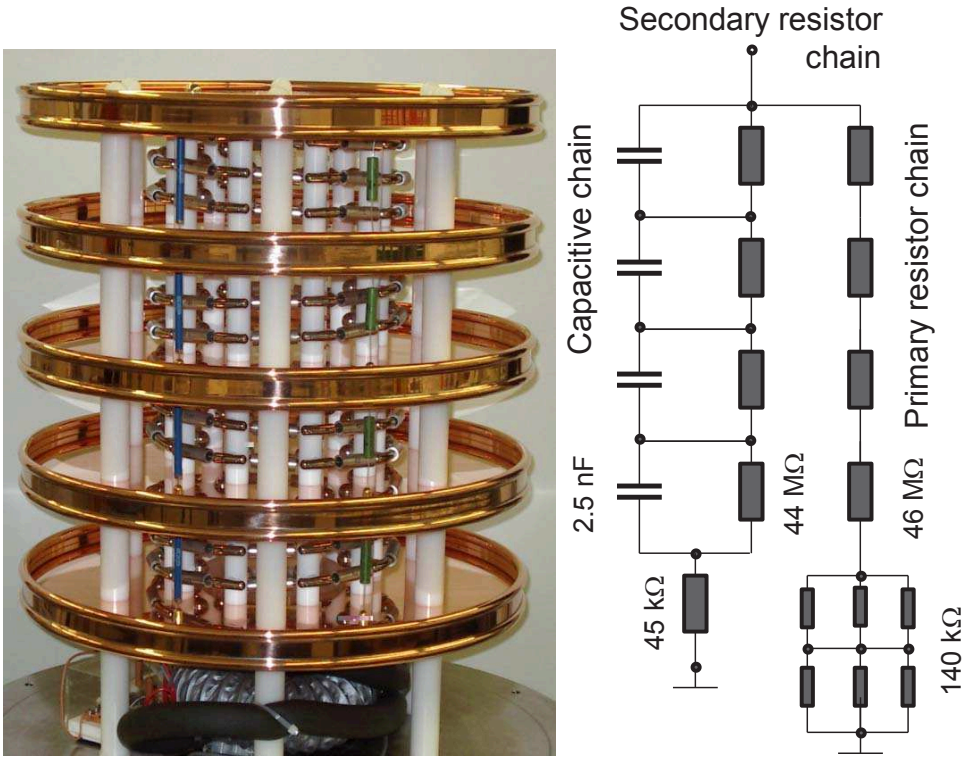

Figure 6.2: The interior of KATRIN's K1 high-voltage divider (left). The primary resistor chain consists of 136 Bulk Metal Foil resistors arranged in a helix structure within five copper ring electrodes. Each high voltage resistor (blue) and capacitor (green) connect a pair of copper electrodes to either form the electrical potential along the primary resistor chain and to protect the primary resistor chain against overloads. The equivalent circuit diagram of the divider is depicted in the right (taken from [Tue09]).

retardation spectrometer to determine the neutrino mass measuring the electron's energy distribution at the end point of the tritium β decay. The electrostatic retarding potential must be measured to the ppm precision to precisely perform the energy measurement. The divider was built by T. Tümmler at the University of Münster [Tue09] to fulfill the following requirements: A voltage of 18.6 kV must be measured for years with a relative accuracy at the ppm level. Therefore, it downsizes the high voltage into a 10 V range which is subsequently measured by a (8.5 digits) digital voltmeter. Since the measurement period is rather long special care has to be taken to avoid any influence due to the temperature, noise and other electronic devices.
This divider (further denoted as K1) allows the determination of voltages up to 35 kV in the sub ppm regime [Tue09] and was used to calibrate the ISOLDE high voltage installation in 2008 [Kri08, Kri11]. Since most of the COLLAPS experiments at CERN are performed at an acceleration voltage U_{ISOLDE} of 50 - 60 kV, a direct calibration at the typical operation voltage was not possible.

However, the K1 divider is mandatory for the success of the KATRIN experiment and therefore the second sub-ppm high precision voltage divider (K2) that was also built for KATRIN in 2009 was upgraded to 65 kV for the purpose of the ISOLDE calibration. It furthermore provides a ripple probe to investigate alternating current (AC) voltages (ripple) on the direct current (DC) high voltage [Ros10]. Both dividers, K1 and K2, are identical in concept and differ only in the amount of resistors. For that reason, the K2 divider is described with the help of an equivalent circuit diagram as depicted in Fig. 6.2 (right). A primary resistor chain consisting of 136 hand-selected Bulk Metal Foil resistors (Vishay VHA 518-11 880 kΩ each) which are arranged in a helix with four turns (thus 34 resistors per turn). The helix is arranged around five copper ring electrodes. A second resistor chain consisting of four Caddock MX360 36 MΩ resistors, where each of them is connected to the corresponding copper ring electrode to ensure a linear potential distribution along the primary resistor chain. A third capacitive chain (four 7.5 nF capacitors - Vishay MKT1816) protects the primary chain against any overloads. The fifth row includes the tapping resistors (140 kΩ) to realize scaling factors of 3636:1, 1818:1 and 100:1. A digital multimeter (FLUKE 8508A) measures the downsized voltage and a calibrated 10 V power supply (Fluke732A) served as a reference which was measured against the K2 divider in advance whenever a voltage was calibrated. Both dividers as well as the Fluke732A reference power supply were specified in advance at the PTB[2] in accuracy as well as in stability to the sub-ppm level [Ros10].
At the ISOLDE facility at CERN two high-voltage power supplies (ASTEC 1 and ASTEC 2) can be connected to the ion source HV platforms. A stabilized high voltage is provided using a servo loop with a ROSS voltage divider 75-10-BDL operated at a scaling ratio of 1000:1. The accuracy of the ASTEC devices as well as the ROSS voltage divider are specified to 10^{-4}. The stability of the dividers are specified to $5 \cdot 10^{-5}$ per year. As depicted in Fig. 6.1 these power supplies (and the dividers) are plunged in an oil bath to temperature stabilize the devices to ±0.1 K. Another ROSS divider is used to downsize the high voltage by a factor of 10 000:1 which is then measured with a digital multimeter (HP 3458A) with an accuracy of 10^{-5}.
Both HV installations with the ASTEC power supplies were calibrated in 2008 up to 35 kV with the K1 divider. In 2009 the ASTEC 1 device was replaced by a state of the art Heinzinger power supply (modified version of the PNChp3p series). It is self-regulated and specified to $1 \cdot 10^{-5}$ stability over 8 hours and to $5 \cdot 10^{-4}$ in case of a load step. Due to the self-regulation the readout is performed with the same ROSS divider (dividing factor of 10000:1) that was previously used with ASTEC 1. Thus, only the ASTEC 2 device could be calibrated under the same conditions as in 2008 during the recent voltage measurements while the new Heinzinger power supply was calibrated using the target readout loop from the former ASTEC 1 device.
The precision voltage divider K2 was implemented at the high-voltage installation at ISOLDE and the calibration performed by comparing the ISOLDE HV readout with the synchronous HV readout from the K2 divider. The HV installation was switched to the new Heinzinger device and the HV was ramped in 5 kV steps from 10 kV up to its limit of

[2] Physikalisch Technische Bundesanstalt

60 kV. After setting a new voltage step, seven minutes waiting time were accommodated to get the system into thermal equilibrium before the measurement was started. Measurement of the downsized voltage was repeated for at least three times in intervals of 30 seconds[3]. From this, the weighted average was taken. After reaching the limit of 60 kV, the HV voltages were measured when a negative stepwise ramp was applied. The calibration curve in Fig. 6.3 (b) displays the discrepancy between the ISOLDE HV readout and the K2 readout. The same procedure was repeated for the ASTEC 2 device and the calibration curve is depicted in Fig. 6.3 (a). The (•) data points represent the calibration obtained in 2008. At that time the data points were fitted with a linear function to extrapolate

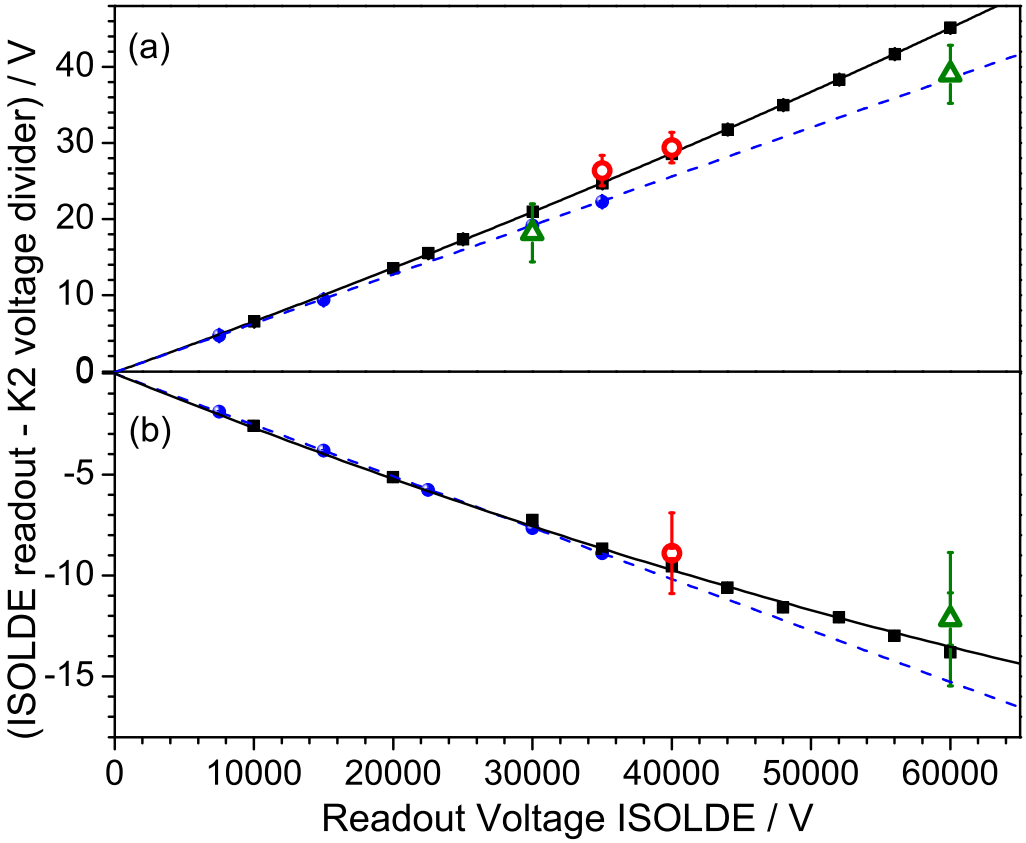

Figure 6.3: Calibration of the ISOLDE HV installations in 2008 (•, linear fit) and 2009 (■), second order polynomial fit). The discrepancy between the ISOLDE HV readout and the high precision voltage divider K2 from the KATRIN experiment is plotted versus the ISOLDE HV readout. The graph (a) shows the calibration curve when the ASTEC 2 power supply was in use whereas in (b) the new Heinzinger device was used. The △ depict the laser spectroscopic results from the first run of the BeTINa experiment whereas ○ show the resultant calibration of the BeTINa beamtime in 2010 [Kri11].

[3]The average of the three results were calculated, weighing the individual values by the standard deviation of the voltage distribution during the 30 s measurement time

calibration factors for voltages higher than 35 kV. For more details see [Kri08, Kri11]. The voltage calibration measurements from 2009 are highlighted as (■). Several fitting functions have been tried, *e.g.* a linear fit with and without fixing the y-axis intersection to zero and second order polynomial functions of the form $y = a_1x + a_2x^2 + b$. A linear function of the form $y = ax$ reproduced the 2008 data (•) well, yielding the calibration function

$$\Delta U = -2.540(24)(40) \cdot 10^{-4} \cdot U, \tag{6.1}$$

where the first uncertainty denotes the statistical and the second one the systematic uncertainty. An extrapolation to 60 kV delivers a deviation of -15.24(15)(24) V. In contrast a parabola fit

$$\Delta U = -2.791(23)(40) \cdot 10^{-4} \cdot U + 8.860(52) \cdot 10^{-10} \cdot U^2. \tag{6.2}$$

reproduces the trend of the 2009 data (■) for the Heinzinger device more precisely and thus reduced the residua of about 1.5 V by about one order of magnitude to 200 mV. At the maximum voltage of 60 kV this yields a deviation of -13.55(16)(24) V. Below 30 kV the 2008 and the 2009 (•) data nearly matches. Therefore the second-order polynomial fit could also be valid for the 2008 data. However, no real conclusion about a drift over the period of 18 month in the region above 30 kV can be drawn.
Due to the fact that the power supply of the HV platform has been changed from the former ASTEC 1 to the Heinzinger device and the calibration curves match, it can be concluded that the internal regulation circuits of both devices are quite accurate and the discrepancy can be attributed to the ROSS voltage divider which was used in both cases for the ISOLDE HV readout. As already mentioned the accuracy of the ROSS divider is specified to 10^{-4} so that this deviation, which is about twice the specified value, can be attributed to aging effects since this device was installed 20 years ago.
The HV platform using the ASTEC 2 power supply was calibrated under the same conditions in 2008 and 2009. Similar to the results in (a) the measurements from 2008 are fitted by the same functions. In this case a linear function with a free offset reproduces the data points best

$$\Delta U = 6.432(26)(40) \cdot 10^{-4} \cdot U - 0.128(68)\ V, \tag{6.3}$$

which yields to a discrepancy of +38.45(22)(24) V at 60 kV. The 2009 data is reproduced by a parabola fitting function

$$\Delta U = +6.51(46)(40) \cdot 10^{-4} \cdot U + 1.721(69) \cdot 10^{-9} \cdot U^2 - 0.118(39)\ V. \tag{6.4}$$

The deviation of +45.13(56)(24) V to the ISOLDE HV readout is not in agreement with the linearly extrapolated value from 2008. Here, the 2008 and 2009 data significantly differ even in the voltage region between 0 and 35 kV. This indicates appreciable instabilities of the ISOLDE HT2 high-voltage divider.
A drift of the ROSS divider was roughly estimated by fitting a second-order polynomial to the 2008 data which obtains a deviation of 6.7 V at 60 kV. In 18 month a change

of $1.2 \cdot 10^{-4}$ was observed. These results show that the extracted calibration factors for this divider are not valid for several month since significant drifts occur and thus further investigations are necessary.
As discussed in Chapter 5 the BeTINa experiment used combined collinear and anti-collinear spectroscopy to perform isotope shift measurements independently of all applied voltages. Therefore, the knowledge of the absolute laser frequencies ν_c and ν_{ac} on a 10^{-9} scale at the same ion velocity is required to fulfill the voltage independent relation $\nu_0^2 = \nu_c \cdot \nu_{ac}$. Vice versa, with the help of the transition rest frame frequency ν_0, the ion's acceleration voltage can be determined with an accuracy better than of 10^{-4}.
The Doppler-shifted frequencies $\nu_{c,ac}$ depend on the transition rest-frame frequency ν_0, the relativistic $\beta-$ and $\gamma-$factor

$$\nu_{c,ac} = \nu_0 \gamma (1 \pm \beta), \tag{6.5}$$

whereby the $\gamma-$factor is a function of $\beta = v/c$

$$\gamma = \frac{1}{\sqrt{1-\beta}}. \tag{6.6}$$

and thus a function of the acceleration voltage U_{acc}. Solving the Eq. 6.5 to the variable β leads to two quadratic equations

$$\beta_{ac} = \frac{\nu_{ac}^2 - \nu_0^2}{\nu_{ac}^2 + \nu_0^2}, \qquad \beta_c = \frac{\nu_0^2 - \nu_c^2}{\nu_c^2 + \nu_0^2}. \tag{6.7}$$

One of these quadratic terms $\beta_{ac,c}$ can be set into Eq. 6.6 to derive the total energy E_{acc}

$$E_{\mathrm{acc}} = mc^2 \cdot \gamma = mc^2 + \underbrace{(\gamma - 1)mc^2}_{E_{\mathrm{kin}} = eU} \tag{6.8}$$

and thus the total acceleration voltage U_{acc} according to

$$U_{\mathrm{acc}} = \frac{mc^2(\gamma - 1)}{e} \tag{6.9}$$

where m denotes the mass of the investigated ion, e the elementary charge and c the speed of light. The results of the high-voltage determination using combined collinear and anti-collinear spectroscopy are indicated in Fig. 6.3. Beforehand it should be noted that these measurements determine the ion velocity by the Doppler shift that is strictly correlated to the starting potential (where the ionization takes place) which can be anywhere inside the heated ionization tube of the ion source. For that reason an offset of about ± 1 - 3 V to the high-voltage divider measurements is expected. In Fig. 6.3 the (△) data point represents the beam energy measurement in 2008 and yield a discrepancy of -12.0(13)(30) V at 60 kV. Within its uncertainty it agrees with both calibration curves. The red circle (○) represents the value for the beam energy measurement in 2010 and is in excellent agreement with the calibration curve of the K2 divider.

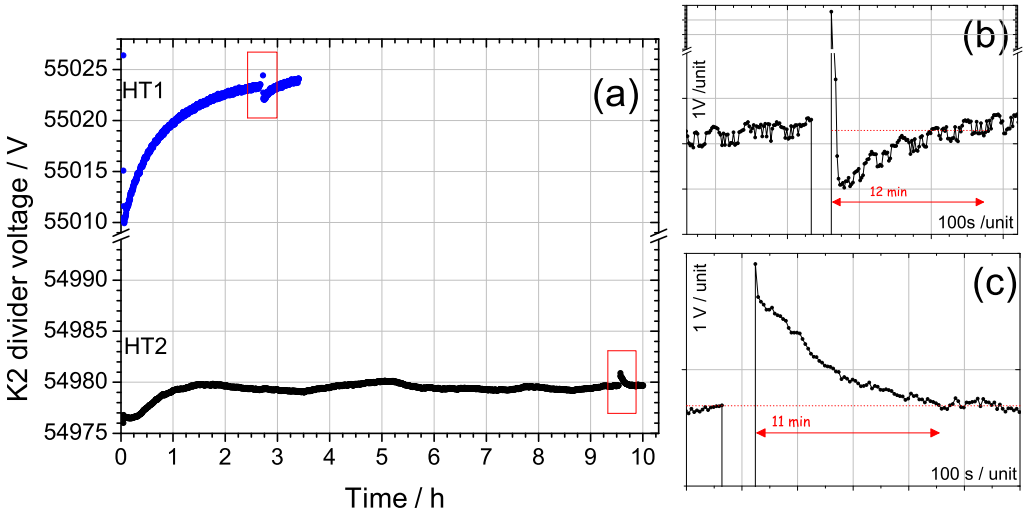

Figure 6.4: Long term measurement of the ISOLDE HV platforms for several hours. Graph (a) shows the stability of the Heinzinger power supply (upper part) and the behavior of the ASTEC 2 power supply (lower part). In the end of both measurements a voltage drop was simulated. An enlarged view of this region is depicted in (b) and (c) respectively.

6.2 Voltage Stability and Transient Behavior

Besides the accurate knowledge of the acceleration voltage applied to the ion beam, its long-term stability during an experiment is of particular importance. Therefore the voltage stability of both power supplies was investigated for several hours. During a collinear experiment a voltage drop might also occur. Such a drop was simulated at the end of the long term measurement switching the power supplies into the stand-by mode for 1 minute and then switched back in one step on again to the nominal voltage. Both power supplies had three hours in advance to reach their thermal equilibrium. The recorded voltage during the long-term measurements are shown in Fig. 6.4. The upper trace in Graph (a) shows the behavior of the Heinzinger power supply. The nominal voltage was set to 55 kV and the K2 divider used to measure the voltage output. During a period of 3 hours the voltage asymptotically drifts from 55010 V to 55023 V. After three hours a voltage drop was simulated and an enlarged view is depicted Graph (b), which shows that the nominal voltage is reached within 12 minutes. It is further observed that the stabilization loop of the Heinzinger device regulates the voltage in small but clearly visible steps of 200 mV. The ASTEC 2 power supply, shown in the lower trace of Fig. 6.4 (a), reached the set voltage within ±3 volts already after less than 1 hour. Then, the voltage only fluctuates around the nominal voltage about ±0.5 V. After 9.5 hours a voltage drop was simulated, which is enlarged in Graph (c) and shows a similar behavior as the Heinzinger device. Eleven minutes after repowering, the nominal voltage is reached again.
From this it can be concluded that the Heinzinger device should not be used for laser spectroscopic measurements, the time to reach to set voltage is too long. Furthermore,

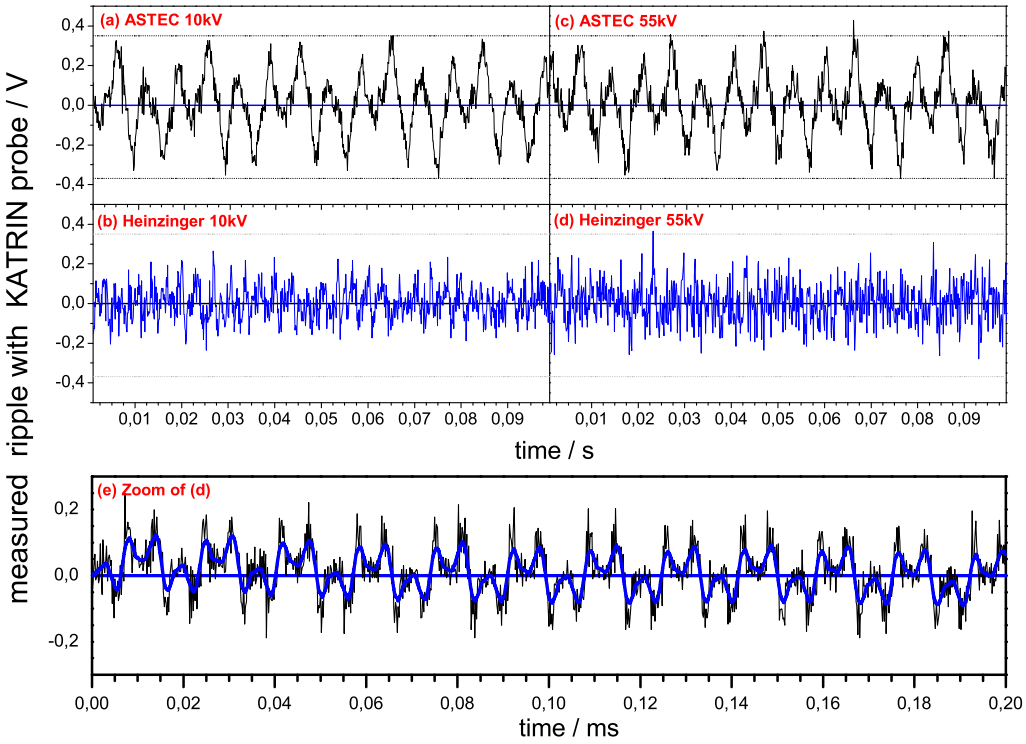

Figure 6.5: Jitter of the ISOLDE HV installation. A ripple probe was used to detect high frequency jitter on the dc voltage output at ISOLDE at 10 kV (a,b) and at 50 kV (c,d). A high resolution scan (e) showed a high frequency ripple on the output of the Heinzinger power supply, whereas the ASTEC device showed low frequency jitter.

after a voltage drop, a new measurement should not be started within the next 15 minutes to avoid any drifts in the acceleration voltage and thus systematic shifts of the resonance. The K2 divider provides a ripple probe to measure fast (ac) fluctuations which are superimposed on the dc component. Such a ripple on the main acceleration voltage can cause additional broadening of the resonance linewidth in collinear laser spectroscopy. Figure 6.5 shows the observed jitter on the high voltage for both power supplies for two cases: Graphs (a) and (b) for a nominal voltage of 10 kV and graph (c) and (d) for 55 kV for the ASTEC and the Heinzinger supply, respectively. For these measurements 10 data points per ms were taken. The observed pattern for the ASTEC power supply is independent of the set voltage and clearly dominated by a regular 50 Hz (and its harmonic of 100 Hz) jitter with a maximum amplitude of ±300 mV. This structure was consistently observed with the ripple probe at the ISOLDE HV installation.
The same measurement has been performed using the Heinzinger power supply. The observed fluctuations exhibit no regular pattern and the maximum amplitude of ±200 mV is a little bit smaller than from the ASTEC device. Therefore it can be concluded that the ripple on the high voltage of both power supplies are rather low and will most probably not influence any laser spectroscopic measurement at COLLAPS.

The lower trace (e) in Fig. 6.5 depicts a high resolution ripple scan recording 5000 data points per ms. This zoom of Graph (d) also shows a regular pattern with a jitter of 125 kHz (as well as its first harmonic) on the dc voltage provided by the Heinzinger power supply. Due to the small peak to peak amplitude of ±200 mV and its high frequency jitter an influence on laser spectroscopic measurements can be excluded. The same pattern was observed at 10 kV set voltage.

6.3 Implications for Laser Spectroscopy Measurements

This section illustrates the implications of a high voltage miss-calibration and of a jitter on the high voltage on laser spectroscopic measurements. Recent isotope shift measurements on short-lived (neutron-deficient) magnesium isotopes clearly demonstrate the utmost importance of the high voltage calibration [Kra10]. During this beamtime the $3s\ ^2S_{1/2} \rightarrow 3p\ ^2P_{1/2,3/2}$ transitions in magnesium ions were investigated. The nuclear charge radii were extracted in terms of the isotope shift according to the stable even isotopes ^{24}Mg and ^{26}Mg which served as a reference. In this case the attention is drawn to the isotope shift between ^{24}Mg and ^{26}Mg. Resonance spectra are depicted in Fig. 6.6. In the

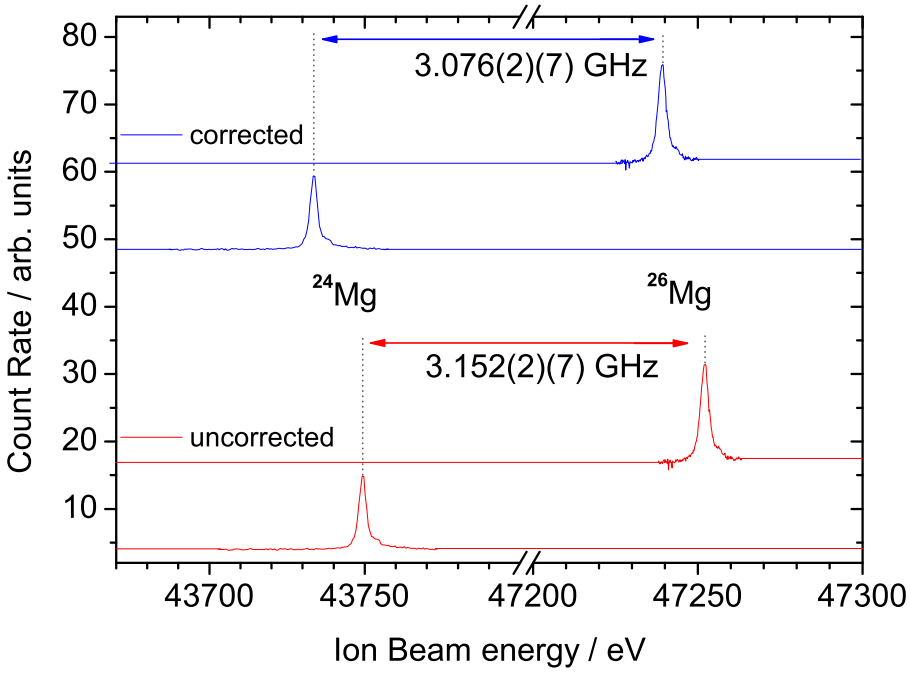

Figure 6.6: Implication of a HV calibration to isotope shift measurements performed at COLLAPS. The lower trace (red) shows the resonance spectra of ^{24}Mg and ^{26}Mg, respectively. Taking the high-voltage calibration into account shifts the resonance spectra relative to their masses to lower beam energies and increases the isotope shift.

lower trace (red) the resonance peaks of ^{24}Mg and ^{26}Mg are plotted and the isotope shift, uncorrected for the observed miss-calibration, is calculated to $\delta\nu_{\mathrm{IS}}^{24,26} = 3.152(2)(7)$ GHz. The uncertainty is reported as the statistical and systematic uncertainty[4]. This isotope shift was accurately determined in an ion trap experiment by Batteiger et al. [Bat09], where $\delta\nu_{\mathrm{IS}}^{24,26} = 3.084\ 905(93)$ GHz was reported. This significantly differs by 68 MHz from the initial COLLAPS value. If the high-voltage calibration is included into the data analysis, both resonance peaks are shifted as shown in the upper trace (blue) and the voltage corrected isotope shift is then $\delta\nu_{\mathrm{IS}}(^{24,26}\mathrm{Mg}) = 3.076(2)(7)$ GHz, which agrees reasonably well with the ion trap measurement. Therefore the precise knowledge of the applied high voltage is of utmost importance. For the very light species it is even more critical so that a relative accuracy of 10^{-5} of the total acceleration voltage is mandatory. The influence of a ripple on the dc voltage was very recently demonstrated at the TRIGA beamline at MAINZ. A power supply (Heinzinger PNChp60-Series) accelerates Pr^+ ions up to 10 kV. This dc HV output was modulated with a saw tooth function applied from a function generator as a simulation of a high frequency jitter. In this configuration the peak structure of the transition in Pr^+ were investigated according to the amplitude of the saw tooth function. The broadening of the resonance curve according to the applied amplitude is depicted in Fig. 6.7. Increasing the amplitude, the peaks become smaller and the linewidth increases. An amplitude of 10 V (= 5 Vpp) nearly doubles the linewidth. But a jitter with an amplitude well below 1 V (as it was observed at CERN) does not influence the linewidth of the peak structure effectively (independently from the frequency). As depicted in Graph (b) a massive broadening of the linewidth was observed if the RF amplitude exceeds 10 V.

6.4 Systematic Uncertainties and Outlook

The last section demonstrated that high-voltage measurements using collinear laser spectroscopy have large potential to offer high accuracy. This concept was already proposed by Poulsen in 1988 [Pou88]. A prototype of such a device was built in Mainz [Goe04] and offered a relative accuracy of about 10^{-4}. This section summarizes the systematic uncertainties that occur in high voltage measurements by collinear laser spectroscopy (CLS) as demonstrated above. First it must be noted that the voltage measured in such a CLS setup is *not* the applied total voltage $U_{\mathrm{tot}} = U_{\mathrm{acc}} + U_{\mathrm{post}}$. The voltage U_{tot} is influenced by several effects to $U = U_{\mathrm{tot}} + \Delta U$ which are discussed in the following.
In [Goe04] a self-made wavemeter, for which a relative accuracy of about 10^{-8} was claimed, was used to determine the absolute frequency of the laser. Nowadays, commercial frequency combs are available which allow absolute frequency measurements better than 10^{-15}. The high voltage measurements during the BeTINa experiment can be regarded as a proof of principle for accurate high-voltage determinations using frequency comb based laser spectroscopy. However, in order to reach accuracies in the sub-ppm regime at high voltages $U > 30$ kV, several contributions, which limit the accuracy in this method must

[4]The systematic uncertainty is usually a relative accuracy of 10^{-4} in the voltage measurement.

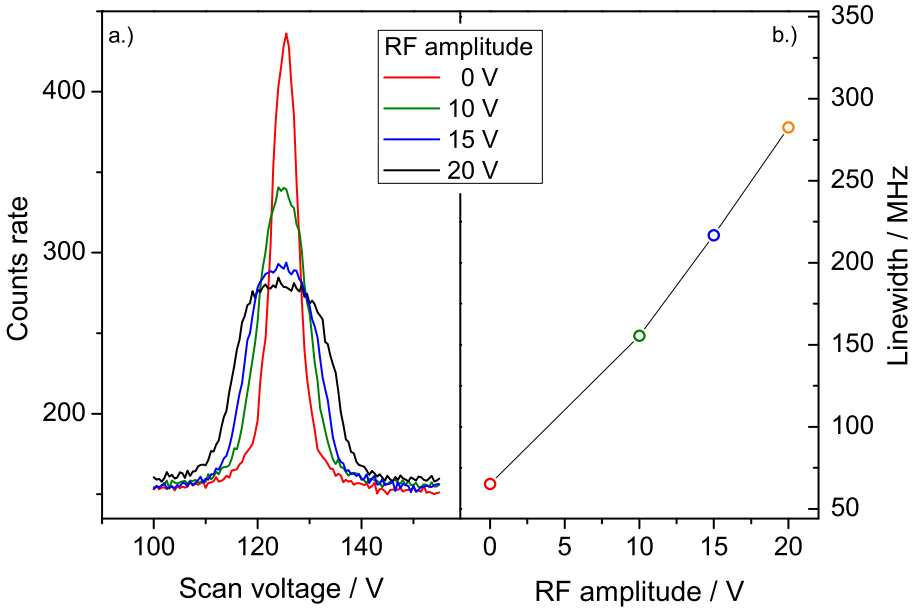

Figure 6.7: Implication of a modulated acceleration voltage on laser spectroscopic measurements. Optical resonances at different modulation amplitudes (left) and the influence of the amplitude on the linewidth (right) are shown.

be eliminated. Based on [Goe04], the main ones are shortly addressed in the following.

- **Uncertainty of the fundamental constants**: The quotient of the ion's mass and the elementary charge (or a multiple of it) are basically determined with a relative uncertainty of 10^{-7}.

- **Laser stabilization**: The laser system which excites the atoms/ions is precisely stabilized in its frequency. A linewidth below 500 kHz and a long-term stability (after 10 hours) of better than 50 kHz was determined with a frequency comb. If a transition is used where a Ti:Sa laser is suitable the linewidth would decrease below 100 kHz, but the long-term stabilization would be comparable in size (approx. some tens of kHz). However, if required a laser can be stabilized much more accurately.

- **Ion source**: A contribution arises due to potential shifts inside the ion source which are unknown. At ISOLDE's hot cavity ion source electrons are emitted and form a plasma at the surface. This and the voltage drop along the tube from direct heating can cause potential shifts of 1 - 3 volts (estimated). A two chamber setup as shown in fig. 6.8 was suggested in [Pou88] and is also described in [Goe04] which is used to suppress any uncertainty caused by the ion source: An acceleration voltage U_{acc} is applied between the ion source and the first optical detection region. The latter is used to measure the ion's velocity v_1. The voltage to be measured is applied between the first and second optical detection chamber which exhibits a potential difference to the ion source of $U_2 = U_{\mathrm{acc}} + U$. The second optical detection chamber

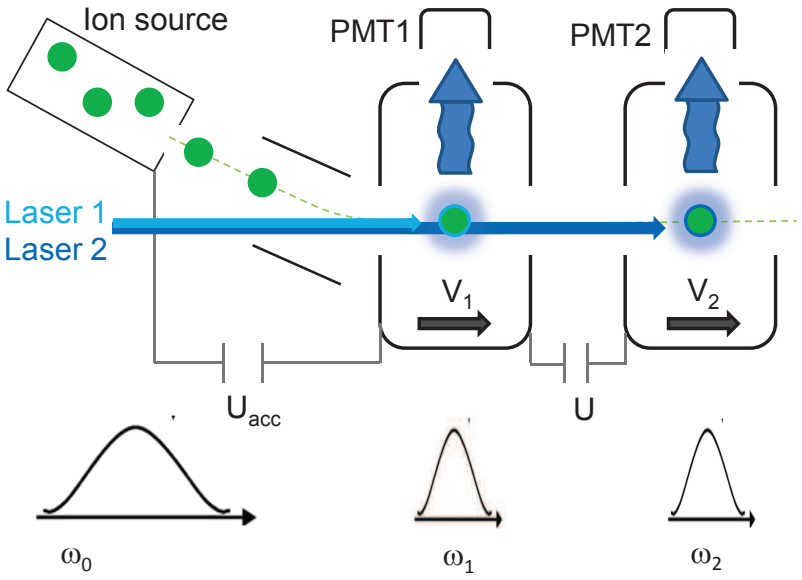

Figure 6.8: Collinear spectroscopy in a two chamber setup for high voltage measurements. The ions are deflected into the experimental apparatus which consists of two detection chambers. In such a setup the ions are preaccelerated with any voltage U_{acc} and ion's velocity v_{acc} is determined in a first optical detection region. The ions then pass a second drift tube and optical detection chamber which exceeds a potential difference U to the first one. In the second detection chamber the velocity v can be determined. Finally, the voltage to be measured is determined by the velocity difference $v - v_{\mathrm{acc}}$ with highest accuracy since the potential shifts caused by the ion source are eliminated.

is used to measure the ion's velocity v_2, whereas the difference in velocity $v_2 - v_1$ determines the voltage $U = U_2 - U_{\mathrm{acc}}$ with highest accuracy. In the framework of this two chamber setup the potential shifts from the ion source are removed which are otherwise the main contribution to the total uncertainty.

- **Ion and laser beam alignment**: As discussed in Section 5.7 parallel and anti-parallel superposition of laser and ion beams is of utmost importance. Usually, the superposition is ensured using two apertures located at both ends of the experimental apparatus. In the BeTINa experiment, this contribution was the dominating effect in the systematic and the total uncertainty. In case of combined collinear and anticollinear spectroscopy, fiber coupling ports could be placed after the viewports. If the laser beams are aligned in such a way that the beam is emitted from one fiber and the coupled into the fiber on the opposite side of the setup, as it has been used *e.g.* in [Nov09], the overlap can be ensured with high precision. However, the superposition with the ion beam still remains to be improved.

- **Lineshape and linewidth** Spectroscopy of ions is favorable since the charge exchange process causes asymmetric lineshapes[5]. Broadening of the linewidth occurs due to the divergence of the ion (laser) beam, the residual ripple of the power supply that provides the acceleration potential $\left(\text{typ. } 10^{-5}\right)$ and the ionization potential of the ion source as mentioned above. Other broadening mechanism *e.g.* saturation broadening and transient time broadening are negligible.

Since the BeTINa experiment demonstrated accurate high voltage determination (10^{-5}) by a frequency comb based laser system, the LUST experiment could be continued in a two chamber setup with a new laser system. Such a setup that directly relates dc voltages to optical frequency measurements offers the potential of high-voltage determination in the ppm regime.

[5]The two chamber setup can only be realized using ions since atoms can not be accelerated after neutralization

7 Summary and Outlook

Within this thesis several frequency-stabilized laser systems for collinear laser spectroscopy were developed and applied for several experiments at TRIGA-SPEC in Mainz and the ISOLDE facility at CERN. This included grating-stabilized diode lasers, a diode-laser based master oscillator power amplifier (MOPA), frequency doubled dye and Ti:Sa lasers and a quadrupled Ti:Sa laser system.
At TRIGA-SPEC in Mainz they were used for a first commissioning of the beamline [Kra10] with Rb atoms, test of a new fluorescence detection chamber [Ham10], an ion-photon coincidence setup [Sie10] and the development of a collinear laser spectroscopy scheme for praseodymium ions which was later used at ISOLDE [Fro13]. With the diode laser based MOPA system and the frequency comb based Ti:Sa laser in combination with second harmonic generation, a laser system has been installed that covers the complete range of elements of interest to be produced for laser spectroscopy at TRIGA-SPEC, which is mainly the region of refractory metals above molybdenum.
The focus of the work at ISOLDE was the isotope shift measurement and the absolute transition frequency determination of ^{12}Be. This is an extension of earlier work in the BeTINa experiment, which determined the isotope shifts and nuclear charge radii from ^{7}Be to ^{11}Be [Tie09, Noe09, Zak10]. In the frame of this thesis, optical isotope shift measurements of the $2s\ ^2\mathrm{S}_{1/2} \rightarrow 2p\ ^2\mathrm{P}_{1/2,3/2}$ transitions in ^{9,10,11,12}Be beryllium ions were performed with a relative accuracy of 10^{-5} by collinear fast beam spectroscopy. The very low production rate of about 8 000 $^{12}\mathrm{Be}^+$/proton pulse required a photon-ion coincidence detection which increased the sensitivity by a factor of 100 compared to the previous experiments. Combining then mass shift calculations [Puc10, Yan10] with the precise optical isotope shift measurements allowed us to extract the change in the rms nuclear charge radius from ^{9}Be to ^{12}Be and therefore the determination of the absolute charge radius of $\mathrm{R}_c\left(^{12}\mathrm{Be}\right) = 2.502(16)$ fm^2. An increase in the nuclear charge radius from the one-neutron halo nucleus ^{11}Be to ^{12}Be of $\delta R^{11,12} = 0.69$ fm was found. The results were compared with the Fermionic Molecular Dynamics Model which reproduces the trend of the experimental results well. From this comparison a large $(sd)^2$-admixture of about 70% to the ground-state wavefunction can be derived. This confirms the observation of a breakdown of the magic shell closure at $N = 8$ in the beryllium chain which was also observerd in other experiments [Oza00, Nav00, Iwa00, Iwa02, Aoi02].
Besides the first determination of the ^{12}Be $2s\ ^2\mathrm{S}_{1/2} \rightarrow 2p\ ^2\mathrm{P}_{1/2,3/2}$ transition frequency, the accuracy of these two transition frequencies for $^{9,10,11}\mathrm{Be}^+$ were considerably improved to a relative accuracy of 10^{-9} due to an enhanced experimental setup *e.g.* the synchronization of the atomic clock to the GPS time standard and an investigation of a photon-ion recoil contribution particularly for the even isotopes.

Since the BeTINa experiment was performed combining collinear and anticollinear laser spectroscopy this method was also used to check the ISOLDE HV installations, which supply the acceleration voltage of usually 30 - 60 kV. Rather large deviations of about 15 and 45 V from the applied 60 kV acceleration voltage were found for the kinetic energy of the ion beam. This triggered a recalibration of the ISOLDE HV-dividers, which was performed using a high precision high-voltage divider from the KATRIN experiment, calibrated to the ppm regime [Tue09]. The importance of this high-voltage calibration was demonstrated for isotope shift measurements of magnesium. The technical design of a high-voltage divider for collinear spectroscopy for COLLAPS and TRIGA-LASER is currently ongoing in Mainz.
The very last isotope of the beryllium chain ^{14}Be is also extremely interesting because it is also known to be a halo nucleus. However, the production rate of $^{14}Be^{+}$ at ISOLDE does not exceed 10 ions/proton pulse and thus the measurement of the optical isotope shift to ^{14}Be is not feasible with the coincidence setup in a reasonable time. The production rate of this isotope is by far not sufficient at ISOL facilities. In contrast to that, in-flight facilities, *e.g.*, FAIR/GSI Darmstadt, FRIB/East Lansing, RIKEN/Japan can reach production rates of several thousand ions per second. But, these highly energetic ions have to be stopped in a gas cell afterwards to achieve a low-energy ion beam with ISOL quality. It is still unsure whether the extraction time can be made sufficiently short for the 4 ms isotope. If so, such a measurement will be a topic for FAIR's low energy beamline experiment LASPEC [Rod10].
An other interesting candidate for optical isotope shift measurements is ^{8}B, a 770 ms isotope that exhibits a proton-halo. Its isotope shift might also be measured using the technique of combined collinear and anticollinear spectroscopy as it was applied in this thesis. Spectroscopy of the light elements will thus be carried into the next isotopic chain. Recently, the nuclear matter radius of ^{8}B was measured in proton elastic scattering experiments in inverse kinematics [Ili11]. The neutron rich boron isotopes ^{17,19}B are also interesting since both are known to be two-neutron halos. However, the mass effect can only be calculated for three-electron systems with sufficient accuracy up to now. Thus helium- or lithium-like boron must be used. An optical transition that is reachable for laser spectroscopy was found from a metastable state $1s\ 2s\ ^3S_1 \rightarrow 1s\ 2p\ ^3P_{2,1,0}$ in helium-like $^{8}B^{3+}$ at a wavelength of 282 nm. Since this is a long lived (100 ms) metastable state it can be excited in a plasma ion source (ECR). Spectroscopy of stable boron based on this transition has already been performed for a test of QED [Din91]. The branching ratio from the excited meta-stable state $1s\ 2p\ ^3P_{2,1,0}$ is 12:1 that the system de-excites into the lower meta-stable state $1s\ 2s\ ^3S_1$ instead to the $1s^2\ ^1S_0$ ground state [Din91]. This might change by the influence of hyperfine induced mixing and must be calculated in advance. Since boron isotopes hardly emerge from ISOL sources, in-flight facilities are in need. In order to achieve spectroscopic resolution, the energy distribution must be decreased to a few eV (ISOL quality) using, *e.g.*, a gas-catcher technique. Such an experiment is proposed at ATLAS to investigate the optimum beam energy and ^{8}B extraction. If the production rate exceeds more than 10^3 atoms/s the beam can be transfered into an ECR ion source where the helium-like charge state will be breeded and the meta-stable state be populated.
A possible proton-halo structure in ^{8}B might affect the cross section of the low-energy

astrophysical reaction $^{7}\mathrm{Be}(p,\gamma)^{8}\mathrm{B}$, which describes the solar neutrino flux initiating from ^{8}B [Cso00, Sch06]. Moreover, the transition in the stable isotope was measured in [Din91] with limited resolution and an improvement will also be of value for a better QED test on this system [Dra12].
At TRIGA-SPEC, up to now only a surface ion source is available which delivers mostly alkali and earth alkali isotopes, which are of less interest for laser spectroscopy since most of them are already investigated. In contrast, neutron rich refractory elements which are not feasible at ISOL facilities can be produced by a plasma ion source that is currently under development. Since there are no chemical limitation in the whole production process the limit concerning half-life is the transport time through the gas jet which is about 400 ms [Eib10]. Compared to the production mechanism applied at the IGISOL[1] facility at Jyväskylä, that is also chemically non-selective, a much higher yield for neutron-rich nuclei from the neutron induced fission is expected at TRIGA-SPEC. Thus, even neutron rich refractory isotopes close to the neutron drip line could be investigated. In this region, the isotopic chains above molybdenum (Z = 42) are of importance.
In the far future, this setup will be transfered to FAIR in Darmstadt where many isotopes will be available that cannot be produced anywhere else [Rod10] and will be exploited by the LASPEC collaboration.

[1] Ion Guide Isotope Separator On-Line

Bibliography

[Aey01] J. Äystö *et al.*: *Development and applications of the IGISOL technique*, Nuclear Physics A, **693**, 477, (2001).

[Alk96] J. S. Al-Khalili *et al.*: *Matter Radii of Light Halo Nuclei*, Physical Review Letters, **76**, 3903-3906, (1996).

[Alk06] G. D. Alkhazov *et al.*: *Experimental studies of the nuclear spatial structure of neutron-rich He and Li isotopes*, Physics of Atomic Nuclei, **69**, 1124-1131, (2006).

[Alk11] G. D. Alkhazov *et al.*: *Nuclear radii of unstable nuclei*, International Journal of Modern Physics E, **20**, 583-627, (2011).

[And69] T. Andersen *et al.*: *Mean-Life Measurements of Excited Electronic States in Neutral and Ionic Species of Beryllium and Boron*, Physical Review, **188**, 1, (1969).

[Ant78] K. R. Anton *et al.*: *Collinear Laser Spectroscopy on Fast Atomic Beams*, Physical Review Letters, **40**, 10, (1978).

[Aoi02] N. Aoi *et al.*: *Anomaly of $N = 8$ shell closure in neutron-rich Be and B isotopes studied via delayed neutron emitting ^{11}Be β decay*, Physical Review C, **66**, 014301, (2002).

[Ara01] K. Arai *et al.*: *Microscopic Multicluster Description of Light Exotic Nuclei with Stochastic Variational Method on Correlated Gaussians*, Progress of Theoretical Physics Supplement, **142**, 97-156, (2001).

[Arn87] E. Arnold *et al.*: *Nuclear Spin and Magnetic Moment of ^{11}Li*, Physics Letters B, **197**, 311-314, (1987).

[Arn92] E. Arnold *et al.*: *Quadrupole moment of ^{11}Li*, Physics Letters B, **281**, 16-19, (1992).

[Aud97] G. Audi *et al.*: *The NUBASE evaluation of nuclear and decay properties*, Nuclear Physics A, **624**, 1-124, (1997).

[Bar91] G. P. Barwood *et al.*: *Frequency Measurements on Optically Narrowed Rb-Stabilised Laser Diodes at 780 nm and 795 nm*, Applied Physics B, **53**, 142-147 (1991).

[Bat09] V. Batteiger *et al.*: *Precision spectroscopy of the 3s-3p fine-structure doublet in* Mg^+, Physical Review A, **80**, 022503, (2009).

[Ber10] J. C. Bernauer *et al.*: *High-Precision Determination of the Electric and Magnetic Form Factors of the Proton*, Physical Review Letters, **105**, 242001 (2010).

[Bla92] B. Blank *et al.*: *Charge-changing cross sections of the neutron-rich isotopes* $^{8,9,11}Li$, Z. Physic A, **343**, 375-379, (1992).

[Bro02] B. A. Brown *et al.*: *The Nuclear Shell Model Towards the Drip Lines*, Progress in Particle and Nuclear Physics, **47**, 517, (2001).

[Bru85] M. Brügger *et al.*: *Operation of a high temperature ion source at the helium-jet on-line isotope separator facility HELIOS*, Nuclear Instruments and Methods in Physics Research A, **234**, 218-223, (1985).

[But84] S. Buttengenbach: *Magnetic Hyperfine Anomalies*, Hyperfine Interaction, **20**, 1-64 , (1984).

[Cam02] P. Campbell *et al.*: *Laser Spectroscopy of Cooled Zirconium Fission Fragments*, Physical Review Letters, **89**, 082501, (2002).

[Cha09] F. C. Charlwood *et al.*: *Nuclear charge radii of molybdenum fission fragments*, Physics Letters B, **674**, 23-27, (2009).

[Che07] B. Cheal *et al.*: *The shape transition in the neutron-rich yttrium isotopes and isomers*, Physics Letters B, **645**, 133-137, (2007).

[Che10] B. Cheal *et al.*: *Progress in laser spectroscopy at radioactive ion beam facilities*, Journal of Physics G: Nucl. Part. Physics, **37**, (2010).

[Cso00] A. Csótó *et al.*: *Study of the* $^3He(^4\mathrm{He},\gamma)^7Be$ *and* $^3H(^4\mathrm{He},\gamma)^7Li$ *Reactions in an Extended Two-Cluster Model*, Few Body Systems (Springer Verlag), **29**, 121-130, (2000).

[Das07] D. Das *et al.*: *Absolute frequency measurement of the lithium D lines: Precise determination of isotope shifts and fine-structure intervals*, Physical Review A **75**, 052508, (2007).

[Del00] A. Delfino *et al.*, *Virtual states of light non-Borromean halo nuclei*, Physical Review C **61**, 051301(R), (2000).

[Din91] T. P. Dinneen *et al. Precision measurements of relativistic and QED effects in heliumlike boron*, Physical Review Letters, **66**, 22 (1991).

[Dob06] A. V. Dobrovolsky *et al.*: *Study of the nuclear matter distribution in neutron-rich Li isotopes*, Nuclear Physics A, **766**, 1-24, (2006).

[Dra99] G. W. F. Drake *et al.*: *Asymptotic expansion method for the evaluation of correlated three-electron integrals*, Canadian Journal of Physics, **83**, 311-325, (2005).

[Dra02] G. W. F. Drake *et al.*: *Progress in helium fine-structure calculations and the fine-structure constant*, Physical Review A, **52**, 3681, (1995).

[Dra05] G. W. F. Drake *et al.*: *Isotope shifts and nuclear radius measurements for helium and lithium*, Canadian Journal of Physics, **83**, 311-325, (2005).

[Dra06] G. W. F. Drake *et al.*: *Studies of light halo nuclei by the isotope shift method*, Hyperfine Interactions, **172**, 141-147, (2006).

[Dra06b] G. W. F. Drake *et al.*: *Atomic, Molecular, and Optical Physics*, 2nd Edition Springer-Verlag ISBN-13:978-0-387-20802-2, (2006).

[Dra10] G. W. F. Drake: *private communication*, (2010).

[Dra12] G. W. F. Drake: *private communication*, (2012).

[Eas86] D. A. Eastham *et al.*: *Coincidence laser spectroscopy - a new ultrasensitive technique for fast ionic or atomic-beams*, Optics Communications, **60**, 293-295, (1986).

[Eas91] D. A. Eastham *et al.*: *Position sensitive detection of photons in ultrasensitive fluorescent spectroscopy*, Optics Communications, **82**, 1-2, (1991).

[Ein05] A. Einstein: *Über die von der molekularkinetischen Theorie der Wärme geforderten Bewegung von in ruhenden Flüssigkeiten suspendierten Teilchen*, Annalen der Physik, Volume **322**, Issue 8, 549-560, (1905).

[Ege02] P. Egelhof *et al.*: *Nuclear-matter distributions of halo nuclei from elastic proton scattering in inverse kinematics*, European Physical Journal A, **15**, 27-33, (2002).

[Eib10] M. Eibach *et al.*: *Transport of fission products with a helium gas-jet at TRIGA-SPEC*, Nuclear Instruments & Methods A, **613**, 226-231, (2010).

[Ett10] S. Ettenauer *et al.*: *Precision ground state mass of* ^{12}Be *and an isobaric multiplet mass equation (IMME) extrapolation for* 2^+ *and* 0_2 *states in the* $T = 2, A = 12$ *multiplet*, Physical Review C, **81**, 024314, (2010).

[Ewa04] G. Ewald *et al.*: *Nuclear Charge Radii of* $^{8,9}Li$ *Determined by Laser Spectroscopy*, Physical Review Letters, **93**, 113002, (2004).

[Fed08] V. N. Fedosseev, *et al.*: *ISOLDE RILIS: New beams, new facilities*, Nuclear Instruments & Methods in Physics Research Section B-Beam Interactions with Materials and Atoms, **266**, 4378-4382, (2008).

[Fel97] H. Feldmeier *et al.*: *Fermionic Molecular Dynamics*, European Physical Journal A, **15**, 27-33, (2002).

[Fir96] R. B. Firestone: *Table of isotopes*, Wiley-Interscience, 8th ed., (1996).

[Fir10] LBL fission homepage. http://ie.lbl.gov/fission/249cft.txt, (2010).

[Fla11] K. Flanagan *et al.*: *Magnetic and quadupole moments of neutron deficient $^{58-62}$Cu isotopes*, Physical Letters B, **703**, 34-39, (2011).

[For11] H. T. Fortune and R. Sherr: *Structure of 2^+, T = 2 states in A = 12 nuclei*, Physical Review C, **83**, 044313, (2011).

[Fre07] M. Freer: *The clustered nucleus-cluster structures in stable and unstable nuclei*, Reports on Progress in Physics, **70**, 2149-2210, (2007).

[Fro13] N. Frömmgen, Dissertation, Universität Mainz, (2013).

[Gei99] W. Geithner *et al.*: *Measurement of the Magnetic Moment of the One-Neutron Halo Nucleus ^{11}Be*, Physical Review Letters, **83**, 3792, (1999).

[Gei00] W. Geithner *et al.*: *Accurate isotope shift measurements on short-lived neon isotopes*, Hyperfine Interactions, **127**, 117-120, (2000).

[Gei02] W. Geithner: *Nuclear Moments and Differences in Mean Square Charge Radii of Short-Lived Neon Isotopes by Collinear Laser Spectroscopy*, Dissertation, Universität Mainz, (2002).

[Gei08] W. Geithner *et al.*: *Mass and charge radii of $^{17-22}$Ne and the two-proton-halo candidate ^{17}Ne*, Physical Review Letters, **101**, 252502, (2008).

[Gil07] M. Gilowski *et al.*: *Narrow bandwidth interference filter-stabilized diode laser systems for the manipulation of neutral atoms*, Optics Communications, **280**, 443-447 (2007).

[Goe55] M. Goeppert-Mayer and J. H. D. Jansen *et al.*: *Elementary theory of the nuclear shell structure*, New York: John Wiley and Sons (1955).

[Goe04] S. Goette *et al.*: *Test of collinear spectroscopy for precise high-voltage determination*, Review of Scientific Instruments, **75**, 4, (2004).

[Hei74] K. Heilig *et al.*: *Changes in mean-square nuclear charge radii from optical isotope shifts*, Atomic Data and Nuclear Data Tables, **14**, 613-638, (1974).

[Ham10] M. Hammen: *Development, Construction and Test of an Effcient Fluorescence Detection Region for Collinear Laser Spectroscopy at TRIGA-Mainz*, Diplomarbeit, Universität Mainz (2010).

[Han87] P. G. Hansen *et al.*: *The Neutron Halo of Extremely Neutron-Rich Nuclei*, Europhysics Letters, **4**, 409-414, (1987).

[Her03] F. Herfurth *et al.*:*Segmented linear RFQ traps for nuclear physics*, Nuclear Instruments & Methods, **204**, 587, (2003).

[Her08] I. Hertel and C. Schulz:*Atome, Moleküle und optische Physik 1*, Springer-Lehrbuch, DOI 10.1007/978-3-540-30617-7, (2008).

[Hey87] K. Heyde *et al.*: *A shell-model description of 0^+ intruder states in even-even nuclei*, Nuclear Physics A, **466**, 189-226 (1987).

[Hof56] R. Hofstadter: *Electron scattering and nuclear structure*, Reviews of Modern Physics, **28**, 3 (1956).

[Hub98] A. Huber *et al.*: *Hydrogen-Deuterium 1S-2S Isotope Shift and the Structure of the Deuteron*, Physical Review Letters, **80**, 468-471, (1998).

[Ili08] S. Ilieva: *Investigation of the nuclear matter density distributions of the exotic ^{12}Be, ^{14}Be and ^{8}B nuclei by elastic proton scattering in inverse kinematics*, Dissertation, Universität Mainz, (2008).

[Ili11] S. Ilieva *et al.*: *Nuclear-matter density distribution in the neutron-rich nuclei $^{12,14}Be$ from proton elastic scattering in inverse kinematics*, Nuclear Physics A, **875**, 8 (2011).

[Ima09] N. Imai *et al.*: *First lifetime measurement of 2_1^+ state in ^{12}Be*, Physical Letters B **673**, 179-182, (2009).

[Iwa00] H. Iwasaki *et al.*: *Quadrupole deformation of ^{12}Be studied by proton inelastic scattering* Physical Letters B **481(1)**, 7-13, (2000).

[Iwa02] H. Iwasaki *et al.*: *Inelastic scattering on ^{12}Be and disappearance of the $N = 8$ magic number*, The European Physical Journal A - Hadrons and Nuclei, **13(1)**, 55-58, (2002).

[Jag74] C. W. de Jager *et al.*: *Nuclear Charge- and Magnetization-Density Distribution Parameters from Elastic Electron Scattering*, Atomic Data and Nuclear Data Tables, **14**, 479-508, (1974).

[Jan72] J. A. Jansen *et al.*: *Nuclear charge radii of ^{12}C and ^{9}Be*, Nuclear Physics A, **188**, 337-352, (1972).

[Jen11] U. D. Jentschura *et al.*: *Hydrogen-deuterium isotope shift: From the 1S-2S-transition frequency to the proton-deuteron charge-radius difference*, Physical Review A, **83**, 042505, (2011).

[Jos62] B. D. Josephson: *Possible new effects in superconductive tunnelling*, Physics Letters, **1**, 7, (1962).

[Kar82] T. Karlewski: *Optimierung einer Plasmaionenquelle für die On-Line Massentrennung von leichten Spaltproduktion mit dem HELIOS-System*, Diplomarbeit, Universität Mainz, (1982).

[Kau76] S. L. Kaufman: *High-resolution laser spectroscopy in fast beams*, Optics Communications, **17**, 3, (1976).

[Ket08] J. Ketelaer *et al.*: *TRIGA-SPEC: A setup for mass spectrometry and laser spectroscopy at the research reactor TRIGA Mainz*, Nuclear Instruments and Methods in Physics Research A, **594**, 162-177, (2008).

[Ket10] J. Ketelaer *The construction of TRIGA-TRAP and direct high-precision Penning trap mass measurements on rare-earth elements and americium*, Dissertation, Universität Mainz, (2010).

[Kna00] K. M. Knaak: *Konzeption und Aufbau eines Experiments zur Spectroskopischen Messung von Hochspannung* , Ruprecht Karls Universität, Heidelberg, (2000).

[Kno04] H. Knöckel *et al.*: *Iodine Spectrum Calculating Software Iodine Spec 4*, Toptica Photonics, (2004).

[Koe98] U. Koester *et al.*: *On-line separation of short-lived beryllium isotopes*, ENAM98 AIP Conference Proceeding **455**, 989, (1998).

[Kop95] S. Kopecky *et al.*: *New Measurement of the Charge Radius of the Neutron*, Physical Review Letters, **74**, 2427-2430, (1995).

[Kra10] J. Krämer: *Construction and Commissioning of a Collinear Laser Spectroscopy Setup at TRIGA Mainz and Laser Spectroscopy of Magnesium Isotopes at ISOLDE (CERN)*, Dissertation, Universität Mainz (2010).

[Kre04] M. Kretzschmar: *Influence of the thermal motion on the line shape and position of resonances in collinear fast beam laser spectroscopy*, Applied Physics B, **79**, 623-627, (2004).

[Kri08] A. Krieger: *Aufbau eines jodstabilisierten Farbstofflasers zur kollinearen Spektroskopie und sein Einsatz zur Hochspannungsmessung an ISOLDE*, Diplomarbeit, Universität Mainz, (2008).

[Kri11] A. Krieger *et al.*: *Calibration of the ISOLDE acceleration voltage using a high-precision voltage divider and applying collinear fast beam laser spectroscopy*, Nuclear Instruments and Methods in Physics Research A, **632**, 23-31, (2011).

[Kug00] E. Kugler: *The ISOLDE facility*, Hyperfine Interactions, **129**, 1-4, (2000).

[Lev10] C. D. P.Levy *et al.*: *Development of the collinear laser beam line at TRIUMF* , Hyperfine Interactions **196**, 287-294, (2010).

[Lit08] Y. Litvinov *et al.*: *Observation of Non-Exponential Orbital Electron Capture Decays of Hydrogen-Like* ^{140}Pr *and* ^{142}Pm *Ions*, Physical Letter B, **664**, 162, (2008).

[Lun09] M. D. Lunney *et al.*: *Cooling of mass-separated beams using a radiofrequency quadrupole ion guide*, International Journal of Mass Spectrometry, **190**, 153-160, (1999).

[Mac69] R. D. Macfarlane *et al.*: *The helium-jet recoil transport method*, Nuclear Instruments and Methods, **73**, 285-291, (1961).

[Man09] E. Mané *et al.*: *An ion cooler-buncher for high-sensitivity collinear laser spectroscopy at ISOLDE*, The European Physical Journal A - Hadrons and Nuclei, **42**, 503-507, (2009).

[Man11] E. Mané *et al.*: *Collinear laser spectroscopy with reverse-extracted bunched beams at TRIUMF*, Hyperfine Interact **199**, 357-363, (2011).

[Man11b] E. Mané *et al.*: *Ground-state spins and moments of* $^{72,74,76,78}Ga$ *nuclei*, Physical Review C, **84**, 024303, (2011).

[May02] T. Meyer Kuckuk: *Kernphysik: Eine Einführung*, ISBM 3-519-13223-0, B. G. Teubner Verlag, (2002).

[Maz76] A. K. Mazumdar *et al.*: *Connection experiments with a hollow cathode ion source and a helium gas jet system for on-line isotope separation*, Nuclear Instruments and Methods, **139**, 319-323, (1976).

[Moo02] R. Moore *et al.*: *Character of an* 8^- *isomer of* ^{130}Ba, Physical Letters B, **547**, 200-204, (2002).

[Moo08] I. Moore *et al.*: *New concepts for the ion guide technique*, Nuclear Instruments and Methods B, **266**, 19-20, (2008).

[Mos73] P. A. Moskowitz *et al.*: *Distribution of nuclear magnetization in mercury isotopes*, Physical Letters B, **46**, 334, (1973).

[Mue07] P. Müller *et al.*: *Nuclear Charge Radius of* ^8He, Physical Review Letters, **99**, 252501-4, (2007).

[Nak06] T. Nakamura *et al.*: *Laser spectroscopy of* $^{7,10}Be^+$ *in an on-line ion trap*, Physical Review A, **74**, 052503-5, (2006).

[Nav00] A. Navin *et al.*: *Direct Evidence for the Breakdown of the* $N = 8$ *Shell Closure in* ^{12}Be, Physical Review Letters **85**, 266-269, (2000).

[Nav09] P. Navrátil, *et al.*: *Recent developments in no-core shell-model calculations*, Journal of Physics G, **36**, 083101, (2009).

[Nef03] T. Neff *et al.*: *Tensor correlations in the unitary correlation operator method*, Nuclear Physics A, **713**, 311-371, (2003).

[Nef05] T. Neff *et al.*: *Structure of light nuclei in Fermionic Molecular Dynamics*, Nuclear Physics A, **752**, 321-324 (2005).

[Nef08] T. Neff *et al.*: *Clustering and other exotic phenomena in nuclei*, European Physical Journal Special Topics, **156**, 69-92, (2008).

[Nef08b] T. Neff *et al.*: *Nuclear structure and reactions in the Fermionic Molecular Dynamics approach*, Journal of Physics: Conference Series, **111**, 012007, (2008).

[Nef11] T. Neff *private communication*, (2011).

[Neu81] R. Neugart: *Laser spectroscopy on mass-separated radioactive beams*, Nuclear Instruments and Methods, **186**, 165-175, (1981).

[Neu85] R. Neugart: *Collinear Laser Spectroscopy on Unstable Isotopes - A Tool of Nuclear Physics*, Hyperfine Interactions, **24**, 159-180, (1985).

[Neu08] R. Nilsson *et al.*: *Precision Measurement of ^{11}Li Moments: Influence of Halo Neutrons on the ^{9}Li Core*, Physical Review Letters, **101**, 132502, (2008).

[Nie00] A. Nieminen *et al.*: *Beam cooler for low-energy radioactive ions*, Nuclear Instruments and Methods in Physics Research A, **469**, 244-253, (2000).

[Nie12] B. Nießen, Diploma thesis, University of Mainz (2012).

[Nil55] S. G. Nilsson: *Relativistic, QED, and finite nuclear mass corrections for low-lying states of Li and Be^{+}*, Physical Review A, **78**, 052511, (2008).

[Nob06] G. A. Noble *et al.*: *Isotope shifts and fine structures of $^{6,7}Li$ D lines and determination of the relative nuclear charge radius*, Physical Review A, **74**, 012502, (2006).

[Noe09] W. Nörtershäuser *et al.*: *Nuclear Charge Radii of Be-7,Be-9,Be-10 and the One-Neutron Halo Nucleus Be-11*, Physical Review Letters, **102**, 062503, (2009).

[Noe11] W. Nörtershäuser *et al.*: *Isotope-shift measurements of stable and short-lived lithium isotopes for nuclear-charge-radii determination*, Physical Review A, **83**, 012516, (2011).

[Nov09] C. Novotny *et al.*: *Sub-Doppler laser spectroscopy on relativistic beams and tests of Lorentz invariance*, Physical Review A, **80**, 022107, (2009).

[Oka08] K. Okada *et al.*: *Precision Measurement of the Hyperfine Structure of Laser-Cooled Radioactive $^{7}Be^{+}$ Ions Produced by Projectile Fragmentation*, Physical Review Letters, **101**, 212502, (2008).

[Ott89] E. W. Otten: *Treatise on heavy-ion science*, Vol. **8**, Plenum Publishing Corporation, (1989).

[Oza00] A. Ozawa *et al.*: *New Magic Number, N = 16, Near the Neutron Drip Line*, Physical Review Letters, **84(24)**, 5493 (2000).

[Pac04] K. Pachucki *et al.*: *Relativistic and QED Corrections for the Beryllium Atom*, Physical Review Letters, **21**, 92, (2004).

[Pac12] K. Pachucki, Talk presented at 501. WE-Heraeus-Seminar, (2012).

[Pen62] S. Penselin *et al.*: *Hyperfine Structure of the Electronic Ground States of ^{85}Rb and ^{87}Rb*, Physical Review, **127**, 2, (1962).

[Pie01] S. C. Pieper *et al.*: *Quantum Monte Carlo Calculations of Light Nuclei*, Annual Review of Nuclear and Particle Science, **51**, 53-90, (2001).

[Pod04] I. Podadera *et al.*: *Design of a second generation RFQ Ion Cooler and Buncher (RFQCB) for ISOLDE*, Nuclear Physics A, **764**, 647c-650c, (2004).

[Poh10] R. Pohl *et al.*: *The Size of the Proton*, Nature **466**, 213-216, (2010).

[Pou82] O. Poulsen: *Velocity and high-voltage measurements using resonant collinear, fast-beam/laser interactions*, Nuclear Instruments and Methods, **202**, 503-509, (1982).

[Pou88] O. Poulsen and E. Riis: *Absolute determination of high voltages using fast-beam laser velocimetry*, Metrologia Springer-Verlag, **25**, 147-153, (1988).

[Pov06] B. Povh: *Teilchen und Kerne*, 7th Edition, Springer Verlag, ISBN-10 3-540-36685-7, (2006).

[Puc06] M. Puchalski *et al.*: *Ground-state wave function and energy of the lithium atom*, Physical Review A, **73**, 022503, (2006).

[Puc08] M. Puchalski *et al.*: *Relativistic, QED, and finite nuclear mass corrections for low-lying states of Li and* Be^+, Physical Review A, **78**, 052511, (2008).

[Puc09] M. Puchalski *et al.*: *Fine and hyperfine splitting of the 2P state in Li and* Be^+, Physical Review A, **79**, 032510, (2009).

[Puc10] M. Puchalski *et al.*: *Nuclear structure effects in the isotope shift with halo nuclei*, Hyperfine Interact, **196**, 35-42, (2010).

[Rae11] S. Raeder: *Spurenanalyse von Aktiniden in der Umwelt mittels Resonanzionisations-Massenspektrometrie*, Dissertation, Universität Mainz, (2011).

[Ren12] D. Renisch, priv. communications, (2012).

[Ric95] L. Ricci *et al.*: *A compact grating-stabilized diode laser system for atomic physics*, Optics Communication **117**, 541-549, (1995).

[Rii94] E. Riis *et al.*: *Lamb shifts and hyperfine structure in* $^6Li^+$ *and* $^7Li^+$*: Theory and experiment*, Physical review A, **49**, 1, (1994).

[Rin09] R. Ringle *et al.*: *High-precision Penning trap mass measurements of* $^{9,10}Be$ *and the one-neutron halo nuclide* ^{11}Be, Physics Letters B, **675**, 170-174, (2009).

[Rod10] D. Rodriguez *et al.*: *MATS and LaSpec: High-precision experiments using ion traps and lasers at FAIR*, European Physical Journal Special Topics, **183**, 1-123, (2010).

[Ros10] S. Rosendahl *et al.*: *Präzisionshochspannung für das KATRIN-Experiment*, Diplomarbeit, Universität Münster, (2010).

[Rot10] R. Roth *et al.*: *Nuclear Structure in the Framework of the Unitary Correlation Operator Method*, Prog. Part. Nuclear Physics **65**, 50 (2010).

[San95] C. J. Sansonetti *et al.*: *Measurements of the resonance lines of* ^6Li *and* ^7Li *by Doppler-free frequency-modulation spectroscopy*, Physical Review A, **52**, 2682-2688, (1995).

[San06] R. Sánchez *et al.*: *Nuclear Charge Radius of ^{11}Li: the Influence of Halo Neutrons*, Physical Review Letters, **96**, 033002, (2006).

[San11] C. J. Sansonetti *et al.*: *Absolute Transition Frequencies and Quantum Interference in a Frequency Comb Based Measurement of the $^{6,7}Li$ D Lines*, Physical Review Letters, **107**, 023001, (2011).

[Sch06] F. Schümann *et al.*: *Coulomb Dissociation of ^{8}B and the Low-Energy Cross Section of the $^{7}Be(p,\gamma)^{8}B$ Solar Fusion Reaction*, Physical Review C, **73**, 015806 , (2006).

[Sch93] T. J. Scholl *et al.*: *Precision measurement of relativistic and QED effects in heliumlike beryllium*, Physical Review Letters, **71**, 14 , (1993).

[Sch96] W. Scherf *et al.*: *Re-measurement of the transition frequencies, fine structure splitting and isotope shift of the resonance lines of lithium, sodium and potassium*, Zeitschrift für Physik D, **36**, 31-33 , (1996).

[Shi95] D. Shiner *et al.*: *Three-Nucleon Charge Radius: A Precise Laser Determination Using ^{3}He*, Physical Review Letters, **74**, 18, (1995).

[Shi07] S. Shimoura *et al.*: *Lifetime of the isomeric 0_2^+ state in ^{12}Be*, Physical Letters B **654**, 87 (2007)

[Sic03] I. Sick: *On the rms-radius of the proton*, Physical Letters B **576**, 62-67 (2003)

[Smi07] M. Smith *et al.*: *First tests of the TITAN digital RFQ beam cooler and buncher*, Hyperfine Interact, **173**, 171-180, (2006).

[Smi08] M. Smith *et al.*: *First Penning-Trap Mass Measurement of the Exotic Halo Nucleus ^{11}Li*, Physical Review Letters, **101**, 202501, (2006).

[Smo11] C. Smorra, *private communication*, (2011).

[Smo12] C. Smorra, Dissertation, Universität Mainz (2012).

[Sie10] B. Sieber: *Aufbau und Test eines Detektorsystems zum Koinzidenznachweis von Ionen und Photonen für die kollineare Laserspektroskopie am TRIGA-Forschungsreaktor*, Diplomarbeit, Universität Mainz, (2010).

[Sun91] D. Sundholm and J. Olsen: *Large MCHF calculations on the hyperfine structure of $Be(^3P_O)$: the nuclear quadrupole moment of ^{9}Be*, Chemical Physics Letters, **177**, 1, 91-97, (1991).

[Sor08] O. Sorlin *et al.*: *Nuclear magic numbers: New features far from stability*, Progress in Particle and Nuclear Physics **61**, 1, 602-673, (2008).

[Ste08a] D. A. Steck: *Rubidium 85 d line data*, available online at available online at http://steck.us/alkalidata (revision 0.1.1, (2008)

[Ste08b] D. A. Steck: *Rubidium 87 d line data*, available online at available online at http://steck.us/alkalidata (revision 2.0.1, (2008)

[Tak09] A. Takamine *et al.*: *Isotope shift measurements of* $^{11,9,7}Be^{+}$, The European Physical Journal A, **5**, 10883, (2009).

[Tal60] I. Talmi *et al.*: *Order of Levels in the Shell Model and Spin of* ^{11}Be, Physical Review Letters, **11**, 103007, (2009).

[Tal87] W. L. Talbert *et al.*: *Optimization of a He-jet activity transport system to use at lampf*, Nuclear instruments and methods B, **26**, 345-350, (1987).

[Tan85] I. Tanihata *et al.*: *Measurements of interaction cross sections and nuclear radii in the light p-shell region*, Physical Review Letters, **55**, 2676-2679, (1985).

[Tan88] I. Tanihata *et al.*: *Measurement of Interaction Cross-Sections Using Isotope Beams of Beryllium and B and Isospin Dependence of the Nuclear Radii*, Physics Letters B, **206**, 592-596, (1988).

[Tan96] I. Tanihata *et al.*: *Neutron halo nuclei*, Journal of Physics G, **22**, 157-198, (1996).

[Tan03] I. Tanihata *et al.*: *Halo and skin nuclei*, Comptes Rendus Physique, **4**, 437-449, (2003).

[Tan12] I. Tanihata, Results presented at the 501. Heraeus Seminar,(2012).

[Thi75] C. Thibaulti *et al.*: *Direct measurement of the masses of* ^{11}Li *and* $^{26-32}Na$ *with an on-line mass spectrometer.*, Physical Review C, **12**, 644-657 (1975).

[Tie09] D. Tiedemann: *Nuclear charge radius determination of* $^{7,10}Be$ *and the one-neutron halo nucleus* ^{11}Be, Dissertation, Universität Mainz, (2009).

[Til04] D. R. Tilley *et al.*: *Energy levels of light nuclei A = 8,9,10* , Nuclear Physics **A**, 745, 155-362, (2004).

[Tor10] B. R. Torabi: *Structure of Beryllium Isotopes in Fermionic Molecular Dynamics*, Dissertation, GSI Darmstadt, (2010).

[Tue09] T. Tümmler *et al.*: *Precision high voltage divider for the KATRIN experiment*, New Journal of Physics **4**, 469 (2009).

[Ude97] T. Udem *et al.*: *Phase-Coherent Measurement of the Hydrogen* $1S-2S$ *Transition Frequency with an Optical Frequency Interval Divider Chain*, Physical Review Letters, **79**, 2646-2649, (1997).

[Ude02] T. Udem, *"Uhrenvergleich auf der Femtosekundenskale"*, Physik Journal **2** 39 (2002).

[Wad06] M. Wada *et al.*: *Laser Spectroscopic Determination of the* ^{06}He *Nuclear Charge Radius*, Physical Review Letters, **93**, 142501, (2004).

[Wal03] J. Walls *et al.*: *Measurement of isotope shifts, fine and hyperfine structure splittings of the lithium D lines*, European Physical Journal D, **22**, 159-162, (2003).

[Wan04] L. B. Wang *et al.*: *Laser spectroscopy of trapped ^{7}Be and ^{10}Be at a prototype slow RI-beam facility of RIKEN*, Hyperfine Interactions, **137**, 153-163, (2006).

[Wen99] K. Wendt *et al.*: *Recent developments in and applications of resonance ionization mass spectrometry*, Fresenius' Journal of Analytical Chemistry, **364**, 471-477, (1999).

[Win76] W. H. Wing *et al.*: *Observation of the infrared spectrum of the hydrogen molecular ion HD^{+}*, Physical Review Letters, **36**, 25, (1976).

[Win83] D. J. Wineland *et al.*: *Laser-Fluorescence Mass Spectroscopy*, Physical Review Letters, **50**, 628-631, (1983).

[Wir95] R. B. Wiringa *et al.*: *Accurate nucleon-nucleon potential with charge-independence breaking*, Physical Review C, **51**, 38-51, (1995).

[Wol76] H. Wollnik: *Principles behind a he-jet system and its application for isotope separation*, Nuclear instruments and methods, **139**, 311-318, (1976).

[Yan00] Z. C. Yan *et al.*: *Lithium isotope shifts as a measure of nuclear size*, Physical Review A, **61**, 022504, (2000).

[Yan02] Z. C. Yan *et al.*: *Lithium transition energies and isotope shifts: QED recoil corrections*, Physical Review A, **66**, 042504, 1-8, (2002).

[Yan03] Z. C. Yan *et al.*: *Bethe Logarithm and QED Shift for Lithium*, Physical Review Letters, **91**, 113004, (2003).

[Yan08] Z. C. Yan *et al.*: *High precision atomic theory for Li and Be^{+}: QED shifts and isotope shifts*, Physical Review Letters, **100**, 243002, (2008).

[Yan08b] Z. C. Yan *et al.*: *Erratum: High Precision Atomic Theory for Li and Be^{+}: QED Shifts and Isotope Shifts*, Physical Review Letters, **102**, 249903(E), (2009).

[Yan10] Z. C. Yan, *private communication*, (2010).

[Yor11] D. T. Yordanov *et al.*: *Nuclear Charge Radii of $^{21-32}Mg$*, Physical Review Letters, **108**, 042504, (2012).

[Zah93] M. Zah *et al.*: *Momentum distributions for $^{12,14}Be$ fragmentation*, Physical Review C, **48**, 4, (1993).

[Zak10] M. Žáková *et al.*: *Isotope shift measurements in the $2s_{1/2} - 2p_{3/2}$ transition of Be^{+} and extraction of the nuclear charge radii for $^{7,10,11}Be$*, Journal of Physics G: Nuclear and Particle Physics, **37**, 055107, (2010).

[Zim94] K. Zimmer *et al.*: *Determination of ^{90}Sr in environmental samples with resonance ionization spectroscopy in collinear geometry*, Applied Physics B, **59**, 117-121, (1994).